

IMPACT OF ATMOSPHERIC AND OCEANIC
FEEDBACKS ON THE STABILITY OF THE
MERIDIONAL OVERTURNING CIRCULATION

Andrea Cimadoribus

Andrea Cimatoribus

Royal Netherlands Meteorological Institute
Global Climate Division

Present address:

Royal Netherlands Institute for Sea Research
Physical Oceanography department
PO box 59, 1790AB Den Burg, Netherlands
Andrea.Cimatoribus@nioz.nl

ISBN: 978-90-393-5953-2

Printing: Ridderprint BV

IMPACT OF ATMOSPHERIC AND OCEANIC
FEEDBACKS ON THE STABILITY OF THE
MERIDIONAL OVERTURNING CIRCULATION

De invloed van atmosferische en oceanografische
terugkoppelingen op de stabiliteit van de thermohaliene
circulatie

(met een samenvatting in het Nederlands)

Proefschrift

ter verkrijging van de graad van doctor aan de Universiteit
Utrecht op gezag van de rector magnificus, prof.dr. G.J. van der
Zwaan, ingevolge het besluit van het college voor promoties in
het openbaar te verdedigen op vrijdag 5 juli 2013 des middags te
12.45 uur

door

ANDREA CIMATORIBUS

geboren op 5 februari 1982
te Maniago, Italië

PROMOTOREN: Prof.dr. H.A. Dijkstra
Prof.dr. S. Drijfhout

This thesis was accomplished with financial support from NWO in the ALW program.

CONTENTS

SUMMARY	xii
SAMENVATTING	xiii
1 INTRODUCTION	1
1.1 The meridional overturning circulation in the Ocean	1
1.1.1 The Meridional Overturning Circulation in the Atlantic Ocean	2
1.2 Stability, freshwater transport and salt-advection feedback . . .	5
1.2.1 Bistability in a box model	5
1.2.2 Bistability in numerical models	9
1.2.3 Salt-advection feedback and freshwater transport	9
1.3 The topics of this study	10
1.3.1 Atmospheric feedbacks in an efficient climate model . .	12
1.3.2 Sensitivity to the different components of freshwater transport	13
1.3.3 Stability and feedbacks of the AMOC in a box model . .	13
2 A GLOBAL HCM BASED ON ATMOSPHERE–SST FEEDBACKS	15
2.1 Introduction	16
2.2 The EMIC SPEEDO	18
2.3 Linear regressions	21
2.4 Results	24
2.4.1 Local regressions	24
2.4.2 Large-scale regressions	29
2.5 HCM test	35
2.6 Summary and Conclusions	39
3 SENSITIVITY OF THE AMOC TO FRESHWATER ANOMALIES	43
3.1 Introduction	44
3.2 Model experiments: methods	46
3.2.1 SPEEDO	47
3.2.2 THCM	51
3.3 Model experiments: results	52
3.3.1 SPEEDO HCM	52
3.3.2 THCM	61
3.4 Discussion and conclusions	64

4	STABILITY AND FEEDBACKS IN A BOX MODEL	69
4.1	Introduction	70
4.2	Methods	73
4.2.1	Model definition	73
4.2.2	Solution method	82
4.3	Results	83
4.3.1	Model sensitivity	84
4.3.2	Stability to freshwater perturbations	87
4.3.3	The role of M_{ov}	93
4.4	Summary and conclusions	99
5	RECONCILING THE NORTH–SOUTH DENSITY DIFFERENCE SCALING WITH GEOSTROPHY	103
5.1	Introduction	104
5.2	Scaling of the AMOC with north–south density difference	106
5.3	Methods	109
5.4	Results	111
5.5	Conclusions	116
6	CONCLUSIONS	119
6.1	Atmospheric feedbacks	119
6.2	Salt-advection feedback in the ocean	121
6.3	Towards an understanding of the three dimensional, turbulent AMOC	121
A	EQUIVALENT FRESHWATER BUDGET IN THE ATLANTIC OCEAN	125
A.1	Equivalent freshwater budget	125
A.1.1	Virtual freshwater transport at $30^\circ S$	126
A.2	Freshwater budget in CLIO	127
B	DERIVATION OF $E_a _{M_{ov}}^0$ AND Δ_E	129
	BIBLIOGRAPHY	133
	LIST OF PUBLICATIONS	145

LIST OF FIGURES

Figure 1.1	A sketch of the MOC (plane view)	2
Figure 1.2	A sketch of the MOC on the meridional plane	3
Figure 1.3	Bistability in Stommel's model	8
Figure 1.4	Salt advection feedback	11
Figure 2.1	Maximum AMOC	22
Figure 2.2	Climatological surface fluxes in SPEEDO	25
Figure 2.3	Local regression parameter	27
Figure 2.4	Large-scale regression parameter	31
Figure 2.5	Effective feedbacks	32
Figure 2.6	Drift in SST between SPEEDO and HCM	34
Figure 2.7	Model drift	35
Figure 2.8	Surface density flux	36
Figure 2.9	Model variability	38
Figure 2.10	Collapse of AMOC	39
Figure 2.11	Overturning streamfunction	40
Figure 3.1	Areas used for freshwater anomalies	47
Figure 3.2	AMOC and freshwater budget, exps. A, B, C, Crev	53
Figure 3.3	Zonal salinity at 30°S	55
Figure 3.4	AMOC and freshwater budget at 30°N, exps. A, B, C and Crev	56
Figure 3.5	AMOC and freshwater budget, exps. D, Drev, HCMc and GCMc	59
Figure 3.6	AMOC and freshwater budget at 30°N, exps. D, Drev, HCMc and GCMc	60
Figure 3.7	Regime diagram of the AMOC	63
Figure 3.8	Effect of dipole anomaly	66
Figure 4.1	Sketch of a bifurcation diagram for the AMOC	71
Figure 4.2	Structure of the box model	74
Figure 4.3	Sensitivity to wind stress	85
Figure 4.4	Sensitivity to gyre exchange in the south	86
Figure 4.5	Sensitivity to symmetric freshwater flux	87
Figure 4.6	Sensitivity to asymmetric freshwater flux	89
Figure 4.7	Continuation of limit point with r_S	91
Figure 4.8	Changes in the bifurcation diagram due to gyres	92
Figure 4.9	Continuation of limit point with r_N	93
Figure 4.10	Skill of M_{ov} as ME indicator	97

Figure 5.1	Density classes involved in the scaling	107
Figure 5.2	Density section in the South Atlantic and Southern Ocean	108
Figure 5.3	Forcing profiles	112
Figure 5.4	Zonal average temperature and MOC in run A	113
Figure 5.5	Scaling of the MOC	115
Figure 6.1	Effect of atmospheric feedbacks on the bifurcation diagram of the AMOC	120

LIST OF TABLES

Table 2.1	Model runs	26
Table 3.1	List of simulations	50
Table 3.2	Freshwater budget	50
Table 4.1	Reference parameters of the box model	80
Table 4.2	Reference solution of the box model	80
Table 5.1	Numerical experiments summary	110

FREQUENTLY USED ACRONYMS

ACC	Antarctic Circumpolar Current
AMOC	Atlantic Meridional Overturning Circulation
EMIC	Earth Model of Intermediate Complexity
GCM	General Circulation Model
GIN	Greenland–Iceland–Norway Sea
HCM	Hybrid Coupled Model
ME	Multiple Equilibria
MOC	Meridional Overturning Circulation
NH	Northern Hemisphere

SH	Southern Hemisphere
SST	Sea Surface Temperature

SUMMARY

The Atlantic Meridional Overturning Circulation (AMOC) is that component of the global ocean circulation which takes place, on average, on the meridional plane. Warm, saline water flows northward in the upper Atlantic Ocean, loses heat to the atmosphere in the mid- and high-latitudes sinking at intermediate depth, then flowing southward. Upwelling takes place at low latitudes due to mixing, and in the Southern Ocean due to wind forcing. The fundamental climatic importance of the AMOC lies in the northward heat transport in the Atlantic Ocean associated with this component of the circulation.

Despite its importance, the understanding of the AMOC dynamics, and in particular of its stability properties, is fragmentary at best. Paleoclimatic data and numerical models (mostly ocean-only models) suggest that the AMOC may undergo abrupt, irreversible collapses if appropriately perturbed, in particular by freshwater anomalies in the northern North Atlantic. However, it is unclear whether such an abrupt transition is possible in the real ocean, in the present-day climate or under global warming. Some state of the art coupled climate models show in fact no such collapse. This different behaviour has generally been attributed to deficiencies of simpler numerical models; in more realistic models, ocean–atmosphere feedbacks would prevent any irreversible collapse of the AMOC. On the other hand, it has also been suggested that biases of freshwater transport in coupled climate models may prevent any irreversible collapse of the AMOC therein.

Here, a simple representation of ocean–atmosphere interaction is presented, using linear regressions to describe the changes of the boundary conditions at the ocean surface as a function of the ocean state, measured by Sea Surface Temperature (SST). This minimal atmospheric model is derived from a coarse resolution numerical model, but the technique can be applied to different models as well as to observations, and it also provides a way to analyse the ocean–atmosphere feedbacks active in a system. Combining an ocean General Circulation Model (GCM) and this minimal atmospheric model, an Hybrid Coupled Model (HCM) was implemented and tested.

The HCM was then used for studying the sensitivity of the AMOC stability to changes in the freshwater budget of the Atlantic Ocean. The numerical simulations performed indicate that the zonal salinity gradient at the southern end of the Atlantic Ocean plays a key role in controlling the sensitivity of the AMOC to freshwater perturbations. These results show that the AMOC response to external perturbations is strongly affected by the freshwater budget of the

Atlantic Ocean, and by the biases that affect its representation in climate models. These results also stress the importance of the freshwater transport by the overturning circulation for the stability of the overturning circulation itself.

These findings were confirmed and extended in a different numerical model, and further studied in the highly idealised framework of a box model. This simple model includes a basic representation of the Atlantic basin with a periodic channel at its southern end. Attempting to reproduce the results from the numerical models, the key processes determining the AMOC stability in the model are identified. In particular, it is suggested that an overturning rate scaling with the meridional density gradient is an essential element. Furthermore, it is shown under which conditions the freshwater transport by the overturning circulation can measure the AMOC stability in the model.

The relationship between the meridional density gradient and the overturning circulation rate is further studied in an idealised numerical model which includes a basin spanning two hemispheres and a periodic channel at its southern end. It is shown that, even if the AMOC is in geostrophic balance, the meridional density gradient is highly correlated with the overturning rate. This is connected to the stratification induced by the presence of a periodic channel in the south. The water upwelling at the northern end of the periodic channel is the one found approximately at the bottom of the pycnocline within the basin. The water at the base of the pycnocline is in turn the one which, in the northern hemisphere, is in geostrophic balance with the maximum meridional overturning rate. The AMOC strength is thus determined not only by the dense water formation in the north, but also by the water properties at the southern end of the Atlantic Ocean.

SAMENVATTING

Gemiddeld genomen stroomt er in het bovenste gedeelte van de Atlantische Oceaan water met een hoge temperatuur en saliniteit naar het noorden. Het koelt onderweg af, zinkt daardoor op hoge breedtegraden naar diepere lagen en stroomt dan weer zuidwaarts. De circulatie wordt gesloten door een omhooggaande beweging, die zowel plaatsvindt rond de evenaar ten gevolge van menging, als in de Zuidelijke Oceaan, waar ze toe te schrijven is aan krachten uitgeoefend door de wind. Deze component van de wereldwijde oceaan-circulatie wordt aangeduid als de Atlantische Meridionale “Overturning” Circulatie (AMOC). De AMOC is van groot belang voor het klimaatsysteem, omdat ze een substantiële hoeveelheid warmte naar het noorden transporteert.

Hoewel van groot belang, is het begrip van de dynamica van de AMOC en in het bijzonder van haar stabiliteit, op zijn best fragmentarisch. Paleoklimatologische gegevens en numerieke modellen (vooral modellen die tot de oceaan beperkt zijn) suggereren dat de intensiteit van de AMOC abrupt en onomkeerbaar kan afnemen als gevolg van bepaalde verstoringen. De AMOC lijkt in het bijzonder gevoelig voor veranderingen in de uitwisseling van zoetwater met de atmosfeer in het noordelijke deel van de Noord Atlantische Oceaan. Het is echter niet duidelijk of een dergelijke abrupte verandering ook kan plaatsvinden in de echte oceaan, hetzij in het huidige klimaat, ofwel als gevolg van de globale opwarming van de aarde. De meest geavanceerde gekoppelde klimaatmodellen laten inderdaad geen sterke afzwakking van de AMOC zien. Er wordt dan ook algemeen van uitgegaan dat dergelijk gedrag in eenvoudiger modellen berust op onvolkomenheden van die modellen: in meer realistische modellen zou de wisselwerking tussen oceaan en atmosfeer ervoor zorgen dat een onomkeerbare afzwakking van de AMOC niet mogelijk is. Daar staat de suggestie tegenover dat gekoppelde klimaatmodellen geen onomkeerbare afname van de AMOC toelaten als gevolg van een systematische fout in het zoetwatertransport in die modellen.

In dit proefschrift wordt een eenvoudige weergave van de interactie tussen oceaan en atmosfeer gepresenteerd. Hierbij wordt gebruik gemaakt van lineaire regressies om de veranderingen in de randcondities aan het oceaanoppervlak te beschrijven als functie van de temperatuur van het water aan het oppervlak. Dit minimale model van de atmosfeer is afgeleid van een numeriek model met een grof rooster, maar bij de hier beschreven methode kan even goed gebruik gemaakt worden van de uitkomsten van andere typen modellen of van observaties. De methodiek voorziet bovendien in een manier om de wisselwer-

king tussen oceaan en atmosfeer te analyseren. Het minimale atmosfeermodel is met een stromingsmodel van de oceaan gecombineerd tot een zogenaamd Hybride Gekoppeld Model (HGM) en dit is vervolgens getest.

Het HGM is daarna ingezet om de gevoeligheid van de stabiliteit van de AMOC voor veranderingen in de zoetwaterhuishouding van de Atlantische Oceaan te bestuderen. De uitgevoerde numerieke simulaties maken duidelijk dat de zonale saliniteitsgradiënt aan de zuidrand van de Atlantische Oceaan een cruciale rol speelt bij het bepalen van de gevoeligheid van de AMOC voor verstoringen van de zoetwaterflux. Deze resultaten tonen aan dat de respons van de AMOC op externe verstoringen sterk wordt bepaald door het zoetwaterbudget van de Atlantische Oceaan. Klimaatmodellen waarin de representatie van het zoetwaterbudget systematisch afwijkt van de werkelijkheid geven dan ook een verkeerd beeld van deze respons. De resultaten ondersteunen bovendien het idee dat de component van het zoetwatertransport die toe te schrijven is aan de AMOC zelf, van belang is voor de stabiliteit van de grootschalige circulatie.

Bovenstaande bevindingen zijn bevestigd en verder uitgebreid in een ander numeriek model en vervolgens bestudeerd in de sterk geïdealiseerde context van een “box” model. Dit eenvoudige model bestaat uit een elementaire weergave van het Atlantisch bekken, met aan de zuidkant een gedeelte met periodieke randvoorwaarden als representatie van de Zuidelijke Oceaan. Door te proberen de numerieke modelresultaten zo goed mogelijk te benaderen, zijn met dit model de processen geïdentificeerd die voor de stabiliteit van de AMOC essentieel zijn. Een van de essentiële elementen lijkt het feit dat de sterkte van de AMOC evenredig is met de meridionale dichtheidsgradiënt. Bovendien wordt beschreven onder welke omstandigheden het zoetwatertransport ten gevolge van de AMOC zelf een maat kan zijn voor de stabiliteit van de AMOC in het model.

Ten slotte is de relatie tussen meridionale dichtheidsgradiënt en de sterkte van de AMOC bestudeerd in een geïdealiseerd numeriek model. Dit model bestaat uit een bekken dat zich over beide halfronden uitstrekt, en een kanaal met periodieke randvoorwaarden aan de zuidkant. Er wordt aangetoond dat de meridionale dichtheidsgradiënt sterk gecorreleerd is met de intensiteit van de AMOC, ook als de AMOC voldoet aan het geostrofisch evenwicht. Dit heeft te maken met de stratificatie die wordt opgelegd door de aanwezigheid van het periodieke kanaal in het zuiden. Het water dat aan de noordkant van het kanaal zijn weg naar boven vindt, is hetzelfde als dat wat zich in het bekken ruwweg aan de onderkant van de pycnocline bevindt. Het water aan de onderkant van de pycnocline is dan weer hetzelfde als het water dat op het noordelijk halfrond in geostrofisch evenwicht is met de AMOC intensiteit. De sterkte van de AMOC wordt dus niet alleen bepaald door de vorming van water met een hoge dichtheid in het noorden, maar ook door de eigenschappen van het water aan de zuidrand van de Atlantische Oceaan.

A Maurilio

*“All saints revile her, and all sober men
Ruled by the God Apollo’s golden mean –
In scorn of which we sailed to find her
In distant regions likeliest to hold her
Whom we desired above all things to know,
Sister of the mirage and echo.”*

“I am not only convinced that what I say is false, but also that what one might say against it is false. Despite this, one must begin to talk about it. In such a case the truth lies not in the middle, but rather all around, like a sack, which, with each new opinion one stuffs into it, changes its form, and becomes more and more firm.”

“What is truth?”

 INTRODUCTION

1.1 THE MERIDIONAL OVERTURNING CIRCULATION IN THE OCEAN

The Meridional Overturning Circulation (MOC) is defined as the zonally averaged flow in the ocean, projected on the plane defined by latitude and depth, i. e. the meridional plane. Its most common measure is given by the overturning streamfunction, Ψ , defined as:

$$\Psi = - \int_{-H}^z \int_{x_W}^{x_E} v \, dx \, dz',$$

where the inner (definite) integral of the meridional velocity v is performed along lines of constant latitude, between the western (x_W) and eastern (x_E) boundaries of the basin under investigation. The outer (indefinite) integral is performed from the bottom H up to the depth level z .

A famous schematic representation of the MOC structure is shown in Fig. 1.1. In the Atlantic, warm and saline waters flow northward at intermediate depth, from the Southern Ocean to the Nordic Seas. Dense water formation in the high latitudes of the Atlantic Ocean provides a source for North Atlantic Deep Water, which then spreads southward, below the pycnocline, as a deep western boundary current as well as in the interior [6, 36, 113]. On the other hand, no deep water is formed in the North Pacific. A second region where deep water forms is the Southern Ocean, around Antarctica. The deep waters formed in the Southern Ocean are denser than deep water of Atlantic origin, and thus spread to deeper levels, down to the ocean bottom. Upwelling takes place over larger areas, in the tropical world Ocean due to mixing and in the Antarctic Circumpolar Current (ACC) due to wind-driven upwelling [62].

When considering the globally averaged circulation on the meridional plane (sketched in Fig. 1.2), the MOC is split in two branches that occupy different depths. The dense water formed around Antarctica fills the deepest Ocean flowing from the south to the north, and its formation rate has to be compensated by mixing induced upwelling to intermediate depths. After gaining buoyancy,

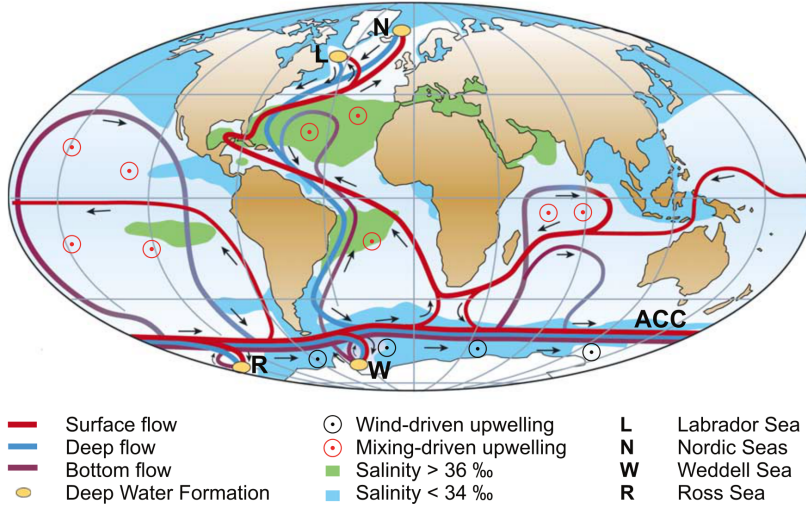


Figure 1.1: Strongly simplified sketch of the global overturning circulation system. From Kuhlbrodt et al. [62].

deep water of Antarctic origin returns to the south and upwells to the surface mixed layer due to Ekman pumping in the ACC. The dense water formed in the northernmost latitudes of the Atlantic Ocean spreads southward above the abyssal overturning cell. The circulation is closed by upwelling in tropical Oceans and in the ACC, and by the northward flow above the pycnocline.

1.1.1 The Meridional Overturning Circulation in the Atlantic Ocean

The focus of this work is on the upper branch of the Meridional Overturning Circulation, usually referred to as “intermediate depth” overturning circulation or Atlantic Meridional Overturning Circulation (AMOC). Fig. 1.1 hints at the reason why the upper branch is referred to as the *Atlantic* MOC. No deep water is formed in the Pacific Ocean, and the upper overturning branch seen in Fig. 1.2 is determined for the largest part by the circulation within the Atlantic basin. The interest in the upper branch of the AMOC mainly stems from its climatic importance. Despite the difficulties associated with estimating the heat transport of the AMOC, it is believed that a northward heat transport of the order of 1 PW is associated with the intermediate MOC branch in the Atlantic Ocean [36]. The most recent estimate of the volume transport in the upper branch of the AMOC is 18.5 Sv, based on RAPID array measurements [55]. Measurements show large variability associated with both the volume and the heat

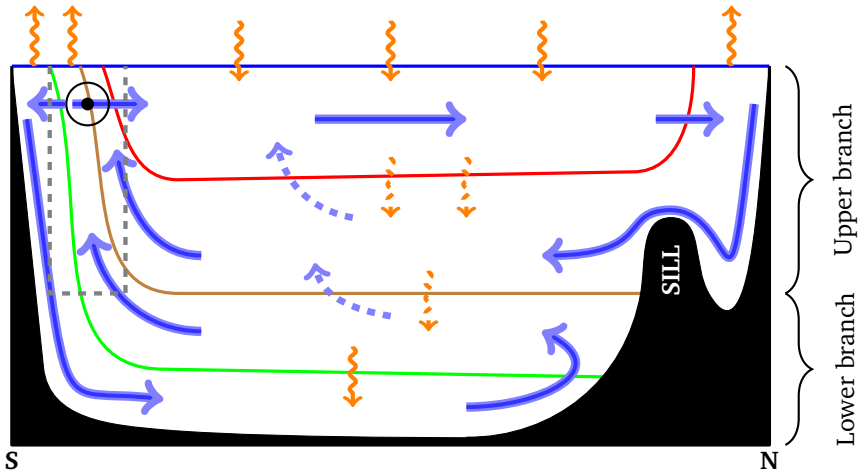


Figure 1.2: An idealised diagram of the two branches of the global MOC as viewed on the meridional plane. Deep water formation takes place at high latitudes, and the present day circulation is represented by the blue arrows. Dashed arrows represent mixing-driven diapycnal fluxes whose importance is subject to debate. Curly orange arrows represent buoyancy fluxes due to surface fluxes (at the top) or due to mixing (in the interior); also in this case, they are dashed if their importance is uncertain. In the south, the Ekman pumping in the ACC region (marked by the grey dashed line) induces upwelling of deep waters. Three isopycnals are drawn, from top to bottom these are: (i) the isopycnal at which the MOC streamfunction attains its maximum (red); on average, at this level, no meridional motion takes place. (ii) The isopycnal where the streamfunction crosses zero (brown), the level where the southward velocity is maximum and the southward transport in the lower branch of the MOC compensates the northward transport in the upper ocean. (iii) The isopycnal where the streamfunction attains its minimum (negative, green in the figure), separating southward flowing waters above from northward flowing waters of Antarctic origin below.

transports at all time scales accessible with present day observation systems (from 10 days to months) [55]. The heat transport connected with the AMOC is thought to be of fundamental importance in mitigating Western European climate. Changes in this part of the ocean circulation may, as a consequence, have a strong impact on the climate of the North Atlantic regions. In particular, numerical results suggest that a collapse of the AMOC may lead to a decrease of the Northern Hemisphere (NH) average atmospheric temperature of the order of $1 - 2^{\circ}\text{C}$ [e.g. 114]. Changes in the AMOC rate are believed to be a key element explaining the strong and abrupt variability of the paleoclimatic records of the last glacial age as well [see e.g. 17, 37].

Despite the importance attributed to the AMOC in controlling the climate system, our understanding of this component of the ocean circulation is still fragmentary at best. Historically, the corner stone of MOC theory has been the abyssal circulation theory of Stommel and Arons [100]. This theory describes the circulation of the deep overturning branch in a bounded domain, given a source of deep water at high latitudes and a diffusive upwelling distributed over the whole basin. Despite its merits, this theory is severely limited by the fact that it assumes that the nature of the downwelling and of the upwelling are known. A different approach was followed in Callies and Marotzke [11] and Marotzke [71], where a model for both branches of the MOC, northward in the upper ocean and southward at intermediate depth, was developed in terms of boundary mixing and planetary geostrophy. This model, though, assumes a priori a density structure in the ocean, and neglects the effect of the winds, but is consistent with findings from idealised numerical experiments [72]. A similar approach was followed by Cessi and Fantini [13].

Further insight in the downwelling process at the northern high latitudes is provided by a series of numerical and analytical studies focusing on the downwelling dynamics in marginal seas [97, 98, 102]. These works discuss the processes controlling downwelling in marginal seas where strong, buoyant boundary currents develop around a dense interior. These studies, originally developed with the Labrador Sea in mind, may be relevant also for the other main downwelling region, namely the Greenland–Iceland–Norway Sea (GIN), where most of the dense water formation takes place [see e.g. 25]. The connection between the downwelling at the northern boundary of the Atlantic Ocean and the planetary scale MOC is still unclear at the moment. Water downwelling at the northern boundary of the Atlantic Ocean may not necessarily enter the deep branch of the AMOC, it may recirculate in the subpolar gyre [96] or may be strongly modified while flowing out of the sills that separate the downwelling regions from the rest of the Atlantic Ocean [25].

Another point of fundamental importance for understanding the dynamics of the AMOC, still subject of debate, concerns the upwelling mechanism of the waters that downwell in the northern North Atlantic. While the traditional view is

that of a mixing driven upwelling, in particular close to the western boundary [see e.g. 71], a more recent hypothesis postulates a quasi-adiabatic ocean interior with wind-driven upwelling concentrated in the Southern Ocean, within the ACC [90, 121]. Given the highly localised nature of the processes responsible for diapycnal mixing, and our limited knowledge of their geographical distribution, it is difficult to assess the relative importance of these two upwelling mechanisms in the real ocean.

1.2 STABILITY, FRESHWATER TRANSPORT AND SALT-ADVECTION FEEDBACK

None of the theories briefly discussed in the previous section focuses on the stability properties of the AMOC. On the other hand, the results obtained from numerical models consistently show that the AMOC can be permanently collapsed if appropriately perturbed, either directly by a freshwater anomaly or possibly in connection with global warming [21, 50, 73, 88, 114].

Paleoclimatic data, showing strong climate variability in the NH during the last glacial cycle, has been connected to AMOC variability too. In particular, it has been suggested that large and abrupt shifts in temperature may be caused by shifts between different regimes of the AMOC, an “ON” state similar to the present day one, and an “OFF” state with little or no overturning circulation in the Atlantic ocean, or even with a reversed circulation [see e.g. 37, 107]. These transitions between states with a strong and a weak or reversed overturning rate would have a strong impact on NH temperatures, due to the associated changes in the meridional heat transport.

1.2.1 *Bistability in a box model*

The model of Stommel [99] is the simplest model of the AMOC that predicts two alternative steady states for the overturning circulation. The model was in fact proposed by Stommel discussing the exchange between evaporative semienclosed basins and the Ocean (e. g. exchange between Mediterranean and Atlantic), but it has become the paradigm of the AMOC bistability. In this view, the AMOC is seen as a two-dimensional circulation between a tropical and a polar box, driven by density differences between the two boxes. In this simple view, multiple equilibria under the same boundary conditions can exist: an ON AMOC, dominated by the dense water formation in the northern box (due to the strong heat flux) and a reverse OFF circulation with downwelling in the tropical box (due to the strong evaporation). The Stommel model captures the central non-linearity involved: the present-day ON state of the AMOC is maintained by a positive “salt-advection feedback” between the northward transport

by the AMOC of high salinity waters in the upper ocean and the salinity (and, as a consequence, density) of northern North Atlantic waters.

Despite its simplicity, it is interesting to briefly discuss the theory of Stommel [99], as it emphasises some of the key elements involved in this study [for a recent overview of the subject, see Chap. 16 of 27]. Stommel considered two boxes of equal size, stirred by mechanical devices, in connection with each other through an overflow at the top, and a capillary at the bottom. One of the boxes can be regarded as the “tropical” box, and is thus warm and saline. The other box can be regarded as the “polar” box, and is thus cold and fresh. Temperature and salinity are controlled by restoring them to some constant value; higher temperature and salinity in the tropical box, lower ones in the polar box. We refer to these values, towards which the boxes are restored, as the “bath” temperature and the “bath” salinity, because they represent the properties of the baths into which the two boxes of the model are immersed, setting the boxes’ properties on sufficiently long time scales. The temperature and salinity differences between the tropical and polar baths are set to $\Delta T^{(b)}$ and $\Delta S^{(b)}$ respectively, where the superscript (b) reminds that the quantities refer to the bath properties.¹ A linear equation of state is used, and the density (ρ) is thus given by $\rho = \rho_0(1 - \alpha(T - T_0) + \beta(S - S_0))$, with ρ_0 , T_0 and S_0 a reference density, temperature and salinity respectively. T and S are a generic temperature and salinity respectively. The constant thermal expansion and haline contraction coefficients are written as α and β respectively. The flow rate through the capillary, Ψ , can be written as $\Psi = -k\Delta\rho/\rho_0$, with $\Delta\rho$ the density difference between the tropical and polar boxes; it is positive when the flow at the surface goes from the tropical to the polar box. The rate of change of temperature difference and of salinity difference between tropical and polar boxes (ΔT and ΔS respectively) can be written as:

$$\begin{aligned} \frac{d}{dt}\Delta T &= c_T(\Delta T^{(b)} - \Delta T) - |2\Psi|\Delta T \\ \frac{d}{dt}\Delta S &= c_S(\Delta S^{(b)} - \Delta S) - |2\Psi|\Delta S, \end{aligned} \tag{1.1}$$

where t is time, while c_T and c_S are two relaxation constants, determining respectively the strength of the relaxation of temperature and salinity to the properties of the baths. The two boxes have unit volume, and the connections between the two have negligible volume. Equations can be cast in a non-dimensional form by defining the following non-dimensional variables (marked by a hat): $\hat{t} = c_t t$, $\Delta\hat{T} = c_T/(2k\alpha)\Delta T$, $\Delta\hat{S} = c_T/(2k\beta)\Delta S$, $\hat{\Psi} =$

¹ Only temperature and salinity differences are relevant, since a linear equation of state is used.

$(c_T/2)\Psi$. Hence, the system of equations 1.1 can be written in non-dimensional form as:

$$\begin{aligned}\frac{d}{d\hat{t}}\Delta\hat{T} &= \eta_1 - \Delta\hat{T} \left(1 + |\Delta\hat{T} - \Delta\hat{S}|\right) \\ \frac{d}{d\hat{t}}\Delta\hat{S} &= \eta_2 - \Delta\hat{S} \left(\eta_3 + |\Delta\hat{T} - \Delta\hat{S}|\right),\end{aligned}\tag{1.2}$$

where the non-dimensional flow rate takes the simple form $\Psi = \Delta\hat{T} - \Delta\hat{S}$. The three non-dimensional parameters are:

$$\begin{aligned}\eta_1 &= \frac{2k}{c_T}\Delta T^{(b)}\alpha, \\ \eta_2 &= \frac{2k}{c_T}\Delta S^{(b)}\beta\frac{c_S}{c_T}, \\ \eta_3 &= \frac{c_S}{c_T}.\end{aligned}\tag{1.3}$$

The first two non-dimensional parameters represent the strength of the heat and salinity forcing respectively (in a more realistic model, freshwater forcing would be used instead of salinity forcing). The third parameter measures the relative strength of salinity restoring and temperature restoring. It is thus a measure of the relative decay time of temperature and salinity anomalies in the ocean. The third parameter is smaller than one, since temperature anomalies can be damped faster by interaction with the atmosphere than salinity anomalies². It is interesting to study the behaviour of the system 1.2 at the steady state. The steady state solution, as measured by the non-dimensional overturning rate Ψ , is plotted in Fig. 1.3 as a function of freshwater forcing, parameter η_2 . For no freshwater forcing, $\eta_2 = 0$, the solution is completely determined by the temperature difference between the two boxes. Cold water sinks in the polar box, and is upwelled by mixing in the tropical box. Increasing the freshwater forcing reduces salinity in the polar box while increasing it in the tropical box. The strength of the overturning decreases as the density difference between the polar and tropical boxes decreases. This solution, which can be shown to be stable, is representative of the present day AMOC (it is the ON state); it is dominated by heat forcing. If the freshwater forcing is increased beyond a critical point, which in this simple model takes the form of a saddle-node bifurcation (marked by L_1 in Fig. 1.3), the solution becomes unstable (dashed line in the figure). If the freshwater forcing is increased more, the system jumps to a

² While a warm patch in the ocean tends to lose more heat to the atmosphere, a salty patch does not influence the freshwater exchange with the atmosphere in any direct way. For this reason, a flux boundary condition for salinity (freshwater) is more realistic. A salinity restoring is only acceptable in a highly idealised context.

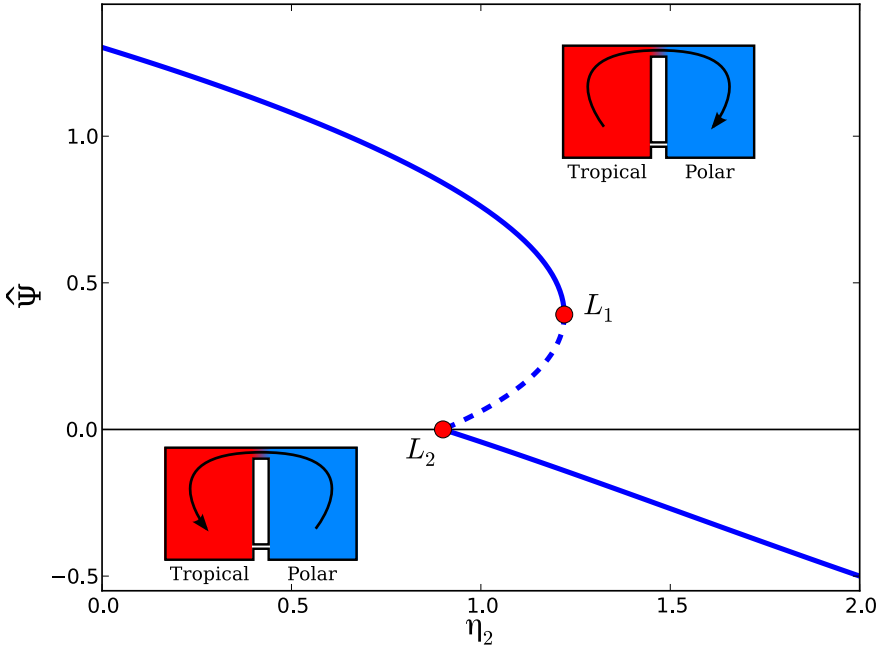


Figure 1.3: The non-dimensional overturning rate $\hat{\Psi}$ of Stommel's box model is plotted as a function of the freshwater forcing, parameter η_2 . The stable solution is plotted as a continuous line, while the unstable solution is plotted as a dashed line. The red dots labelled L_1 and L_2 mark the positions of the two saddle-node bifurcations where the stability of the solution changes. Two sketches show the two boxes forming the model, with the circulation patterns of the ON (top) or OFF (bottom) states superimposed.

different steady state characterised by a reversed flow, since no steady solution with positive Ψ exists to the right of L_1 . This second solution is the OFF state, and is dominated by the effect of freshwater forcing. If the freshwater forcing is reduced again, the ON solution is not recovered at the same value of freshwater forcing that determined the reversal of the circulation. The freshwater forcing has to be reduced further, down to a second saddle-node bifurcation, marked by L_2 in the figure. There is a region where three different steady state solutions are available, among which two are stable and one is not, and the system shows a hysteresis behaviour. In this region, transitions between the two stable states are possible if a sufficiently large perturbation is applied. In particular, transitions between stable states are possible if a perturbation in overturning strength is applied, strong enough to cross the unstable solution. This region is usually referred to as the *multiple equilibria regime*. Physically, the hysteresis is caused by a feedback between advection and density. A positive overturning

transports salt and heat to the polar box. An increased salinity in the polar box increases the density therein, and thus the overturning rate; a positive feedback is active between advection and salinity. The opposite holds for the heat content in the polar box (salt-advection feedback). A negative feedback is instead active between advection and heat content, and the balance between the two opposing feedbacks will eventually determine the appearance of a steady state. Given the different relaxation times of temperature and salinity, temperature is virtually set by the bath temperature (perturbations are damped quickly), while salinity is more influenced by the direction and rate of the flow (salinity perturbations are damped more slowly). The two opposing feedbacks, due to heat and salinity, thus have different strength and the salt-advection feedback can destabilise the flow within a range of values of the freshwater forcing (the multiple equilibria regime).

1.2.2 *Bistability in numerical models*

Although an oversimplification of the real system, Stommel's results have provided, in the lack of more physically grounded models, a minimal explanation for the hysteresis behaviour of the AMOC in several other models of higher complexity. An abrupt collapse of the AMOC in response to a quasi-equilibrium increase of the freshwater forcing in the North Atlantic, not followed by any spontaneous recovery, has been reported in various ocean and climate models of different complexity [see among others 21, 50, 73, 88, 114]. Despite these results, a shared view on the stability of the AMOC has not emerged yet. Schmitner et al. [91], for instance, discuss the lack of any abrupt collapse of the AMOC in response to increasing CO₂ concentrations. This work is in fact not directly comparable with those from models using a direct (and stronger) freshwater forcing in the North Atlantic, but still raises questions on the importance of bistability and salt-advection feedback in state-of-the-art climate models. Also Latif et al. [64] and Yin et al. [124] suggested that air-sea interaction may provide a stabilising mechanism for the AMOC, making a permanent collapse of the AMOC impossible.

1.2.3 *Salt-advection feedback and freshwater transport*

Further insight in this issue is given in Huisman et al. [54], using an ocean-only model, and Drijfhout et al. [30], analysing the coupled climate models of the CMIP3 archive. In both works, the existence of a permanent shut-down state of the AMOC is connected with the salt and freshwater budget of the Atlantic Ocean. In particular, Drijfhout et al. [30] suggest that the lack of a collapsed state in IPCC-class climate models may be attributed to a bias in the salt trans-

port by the AMOC, in connection with the salt-advection feedback at the Atlantic basin scale.

Stommel's box model is often interpreted as representing the overturning circulation between the tropical and subpolar North Atlantic, but a box model can be developed aiming at a basic representation of the interhemispheric AMOC, closely following the ideas of Stommel [99]. The salt-advection feedback operates in this case between the North Atlantic Ocean and the Southern Ocean [86, 89, 92]. With this interpretation in mind, it is not possible to decide a priori the sign of the salinity difference between the two boxes of the Stommel's box model. The properties of the water masses that the two boxes are meant to represent can not be distinguished as easily as in the case of tropical and subpolar Atlantic Ocean.

This subtle difference seems to play a fundamental role in the interpretation of the results from numerical models. The value of the net equivalent freshwater import, or scaled salt export, by the overturning circulation at the southern border of the Atlantic Ocean is the key quantity that signals the coexistence of two stable equilibria of the AMOC. The value of this freshwater transport is written conventionally either as M_{ov} or as F_{ov} ; the first notation is used in this work. Its formal definition is given in the following chapters, but its meaning is introduced here. M_{ov} represents the net amount of freshwater imported in the Atlantic basin by the meridionally overturning component of the ocean circulation alone; it must be in balance with the freshwater transport by the atmosphere as well as by other components of the ocean circulation (see Fig. 1.4). This quantity is computed at the southern end of the Atlantic Basin, usually taken to be the latitude of the southern tip of the African continent. If M_{ov} is positive, the overturning circulation is exporting salt out of the Atlantic basin. A negative perturbation in the AMOC rate would lead to a positive density anomaly within the Atlantic basin that, once advected or diffused to the downwelling regions of the North Atlantic, would tend to damp the initial AMOC perturbation (i. e. increase overturning rate again). In this case, only the present day ON state of the AMOC is stable. In other terms, a *positive* M_{ov} corresponds to a *negative* salt-advection feedback at the basin scale, i.e. more salt is accumulated in the Atlantic Ocean if the AMOC transport decreases. If M_{ov} is negative, on the other hand, salt is imported into the basin by the overturning, and a second stable state of the AMOC exists; salt-advection feedback makes the AMOC sensitive to finite amplitude perturbations (see Fig. 1.4).

1.3 THE TOPICS OF THIS STUDY

While the role played by M_{ov} in determining the existence of the multiple equilibria of the overturning circulation has already been studied in detail [21,

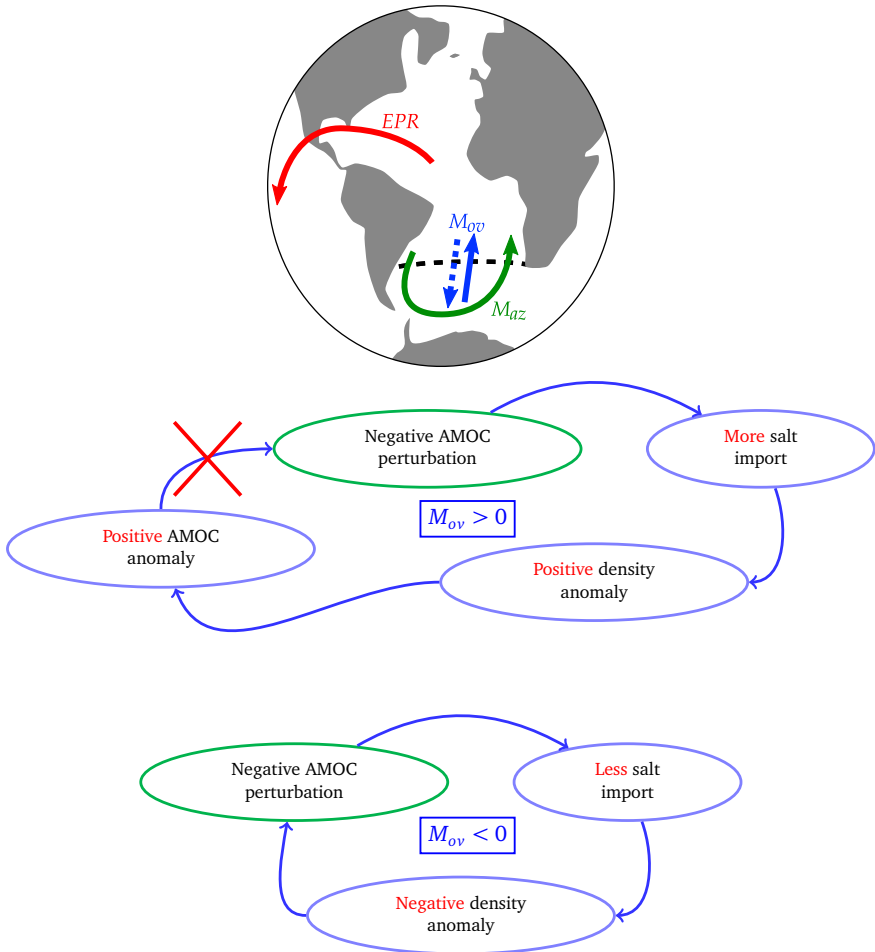


Figure 1.4: Top: the balance between net evaporation out of the Atlantic Ocean (EPR) and freshwater import by the ocean circulation through the southern end of the Atlantic Ocean. The freshwater import by the ocean circulation is in turn split in two parts: the transport by the overturning circulation (M_{ov}) and the transport by the gyre circulation (M_{az}). Centre and bottom: diagrams of the salt-advection feedback mechanism, for M_{ov} of different sign. For positive M_{ov} (centre) salt-advection feedback is negative, i. e. is not active. For negative M_{ov} (bottom) salt-advection feedback is positive, and the AMOC can collapse due to finite amplitude perturbations.

54], the importance of other feedbacks has received less attention. In particular, the importance of ocean–atmosphere interaction is still subject of debate [see e.g. 101]. The role of other components of the freshwater transport in the ocean, first of all the transport by the wind-driven gyres, is still unclear too. The importance of the freshwater transport by the wind-driven gyre was in fact already noted at least by de Vries and Weber [21]. They exploited the freshwater transport by the wind-driven gyre to control the sign of M_{ov} and, as a consequence, the stability of the AMOC. However, the mechanism underlying the interaction between the different components of the freshwater transport and the AMOC stability were not investigated in detail.

1.3.1 *Atmospheric feedbacks in an efficient climate model*

As already mentioned, a collapse of the AMOC is thought to have a strong climatic impact. The abrupt cooling of the NH, determined by the reduction of the northward heat transport carried by the AMOC, would change the zonally averaged surface temperature profile. This would in turn modify the wind as well as the net evaporation at the surface. In the real climate system, these changes in the atmosphere, caused by a collapse of the AMOC, would feed back into the ocean, possibly determining substantial differences in the response of the coupled system, compared to the ocean alone. As an example, a freshwater perturbation in the northern North Atlantic may reduce the overturning rate and the northward heat transport. The cooling of the atmosphere in the NH induced by this perturbation would in turn cause a cooling, and thus densification, of water in the NH Ocean. This may determine a partial or complete recovery of the AMOC by enabling more dense water formation.

In order to investigate the importance of atmospheric feedbacks for the AMOC stability, ocean–atmosphere interaction during a collapse of the AMOC has been analysed in a coupled General Circulation Model (GCM). The coupled GCM has been used as a basis for providing state-dependent boundary conditions to an ocean model, thus obtaining a minimal representation of ocean–atmosphere interaction valid for long time scales. These boundary conditions have been tested by forcing the ocean component of the GCM, enabling time integration on time scales of tens of thousand years. Despite the efficiency, these boundary conditions allow for a minimal representation of atmospheric feedbacks that would otherwise be lost in an ocean-only model. This work is described in Chap. 2. The same boundary conditions including atmospheric feedbacks have also been used in a study by den Toom et al. [23]. In this latter study, the effect of atmospheric feedbacks on the shape of the bifurcation diagram of the AMOC is studied in detail in an idealised ocean GCM. These results are briefly discussed in the last chapter.

1.3.2 *Sensitivity to the different components of freshwater transport*

As mentioned above, a second important point of discussion regarding the stability of the AMOC in numerical models concerns the influence of the wind-driven gyres and, more in general, of the horizontal circulation. It has been shown that M_{ov} , the freshwater transport by the overturning circulation, has a fundamental importance for determining the stability of the AMOC, but what sets the value of M_{ov} ? The freshwater transport by the overturning circulation has to balance, on average, the freshwater transport by the horizontal circulation in the ocean as well as the atmospheric freshwater transport, i. e. net evaporation at the surface. Under fixed boundary conditions at the surface, the freshwater transport in the ocean can still be distributed differently between its different components; with what impact on AMOC stability? These problems have been studied analysing the sensitivity of the AMOC to different freshwater anomalies applied at the surface, that determine different distributions of freshwater transport between the overturning and horizontal components of the circulation.

The ocean GCM coupled to the simplified atmosphere described in Chap. 2 has been used to investigate the effect of anomalies in different components of the freshwater transport. Besides this, a second, more idealised, ocean-only model has been used, enabling a more systematic exploration of the phase space. In Chap. 3 the importance of the freshwater transport by the wind-driven gyres is discussed, with a focus on the role of the southern subtropical gyre. This study is particularly relevant for climate models, which consistently show biases in the salinity fields and, as a consequence, in the different components of the freshwater transport between the Atlantic and the other ocean basins [30]. It is shown here that the freshwater transport by the southern subtropical gyre of the Atlantic Ocean can strongly affect the response of the AMOC to freshwater perturbations. It is also shown that freshwater anomalies in the southern hemisphere can be sufficient for inducing a complete collapse of the AMOC.

1.3.3 *Stability and feedbacks of the AMOC in a box model*

The results of Chap. 3 are revisited in Chap. 4, in the framework of a simple semi-analytical model. A simple model has the advantage of providing complete control over the parameters used. It also helps clarifying the assumptions that are involved in most numerical studies on the AMOC, and enables to discuss the essential elements determining the stability properties of the AMOC. In this much simpler framework, compared to a GCM, it is shown again that the freshwater transport by the southern subtropical gyre is an effective source of

perturbations for the AMOC. It is also shown that the dependence of the AMOC strength on the north–south density difference is essential for reproducing the sensitivity of the AMOC observed in more complex GCMs.

Furthermore, the validity of M_{ov} as a stability indicator of the AMOC can be discussed in analytical terms in the box model. It is shown that M_{ov} is a perfect indicator if feedbacks other than the salt-advection one are negligible. The skill of M_{ov} in identifying the Multiple Equilibria (ME) regime is also assessed when other feedbacks are included, in particular when vertical diffusion and wind-driven gyres are present.

Further discussion of the scaling used for the AMOC strength is given in Chap. 5. In particular, the use of a scaling depending on the north–south density difference is motivated by reviewing the present knowledge on the dynamics of the pycnocline and by considering a set of idealised numerical simulations. The importance of geostrophy in setting the AMOC strength is also discussed.

A summary and a discussion of the results of the entire work is done in Chap. 6.

2

A GLOBAL HYBRID COUPLED MODEL BASED ON ATMOSPHERE–SST FEEDBACKS.

A global hybrid coupled model is developed, with the aim of studying the effects of ocean–atmosphere feedbacks on the stability of the Atlantic meridional overturning circulation. The model includes a global ocean general circulation model and a statistical atmosphere model. The statistical atmosphere model is based on linear regressions of data from a fully coupled climate model on sea surface temperature both locally and hemispherically averaged, being the footprint of Atlantic meridional overturning variability. It provides dynamic boundary conditions to the ocean model for heat, freshwater and wind-stress. A basic but consistent representation of ocean–atmosphere feedbacks is captured in the hybrid coupled model and it is more than 10 times faster than the fully coupled climate model. The hybrid coupled model reaches a steady state with a climate close to the one of the fully coupled climate model, and the two models also have a similar response (collapse) of the Atlantic meridional overturning circulation to a freshwater hosing applied in the northern North Atlantic.

This chapter has been published as:

A. A. Cimadoribus, S. S. Drijfhout and H. A. Dijkstra. A global hybrid coupled model based on atmosphere–SST feedbacks. *Clim. Dyn.*, 38:745–760, 2012.

2.1 INTRODUCTION

Since the pioneering work by [99] on a conceptual model of the thermohaline circulation, the problem of the stability of the Atlantic Meridional Overturning Circulation (AMOC) has become one of the main issues in climate research. A collapse of the AMOC is often used to explain abrupt changes in past climate records. In recent years, a possible AMOC collapse in response to increased freshwater forcing in the northern North Atlantic, expected as a consequence of global warming, has been identified as a low probability but high risk future climate event [1, 9, 17].

An abrupt collapse of the AMOC, in response to a quasi-equilibrium increase in freshwater forcing in the North Atlantic, has been reported in different ocean and Earth Model of Intermediate Complexitys (EMICs) [88]. This implies a non-linear response of the ocean to the freshwater forcing, with a sudden collapse of the overturning above a threshold value of the freshwater forcing. The EMIC results are challenged by the model experiments of [124] and by IPCC-AR4 General Circulation Model (GCM) results, as analysed in [91]. In the latter, it is found that the AMOC strength decreases approximately linearly in response to a CO₂ increase according to the SRES-A1B scenario and there is no collapse. It must be noted that the simulations to detect possible multiple equilibria regimes of the AMOC in these GCMs have not been done. The near-linear response to the gradual freshwater flux perturbation as found in [91] does not rule out the possibility of a sudden collapse with a stronger freshwater flux.

However, from the GCM results it has been suggested that the existence of a multiple equilibria regime is an artefact of ocean-only models, and in particular of poor (or absent) representation of ocean–atmosphere interactions. In an ocean-only model, the salt advection feedback is the central feedback affecting the stability of the AMOC. When an atmosphere is coupled to the ocean model, other feedbacks, due to the ocean–atmosphere interaction, become relevant. The effect of these feedbacks may eventually overcome the effect of the salt-advection feedback, and remove the multiple equilibria found in ocean-only models and EMICs.

In some models, the response of the atmosphere to AMOC changes may indeed act to stabilise the present day AMOC [101, 115]. In particular, the southward shift of the intertropical convergence zone would enhance the surface salinity of the Atlantic north of the equator, increasing the northward salinity transport by the northern hemispheric gyres [59, 115]. The decrease in the atmospheric temperature of the Northern Hemisphere (NH), as a consequence of the AMOC collapse, may also play a role [101]. Lower atmospheric temperatures would determine stronger heat extraction from the ocean and, consequently, higher densities of surface waters. This effect may be more than compensated by the insulating effect of a NH ice cover extending more to the

south [115]. The potential impact of changes in the wind-stress, in particular zonal wind-stress, has recently been investigated in [3], but the magnitude of the changes induced by the wind-stress feedback remains unclear.

The question that must be answered is: “Do the atmospheric feedbacks remove the multiple equilibria regime of AMOC, as found in ocean-only models and EMICs?” The first step to try to answer this question is, in our view, to find a simple, but quantitative, description of these atmospheric feedbacks, extending that of box-model representations [79]. Only when a quantitative description of the feedbacks is available, it is possible to assess the impact of the ocean–atmosphere interaction on the stability properties of the AMOC. Studies to isolate the effect of the different feedbacks using a GCM are computationally expansive. Furthermore, the complexity of a full GCM can hinder the understanding of the relevant processes in the system. For these reasons, simpler atmospheric models are needed to provide dynamic boundary conditions to full ocean GCMs. Their design can benefit from the fact that the atmosphere, on the ocean time scales, can effectively be treated as a “fast” component that adjusts to the ocean anomalies. These coupled models are often referred to as Hybrid Coupled Models (HCMs).

Since the main known atmosphere–ocean coupled mode of variability is the El Niño Southern Oscillation (ENSO), HCMs have been developed mainly to study this phenomenon, focusing on the interaction between wind and Sea Surface Temperature (SST) in the tropical oceans. In this framework, the main atmosphere–ocean interaction to include in the model is the change in the zonal winds over the equatorial Pacific in response to SST anomalies [12]. [4] used a statistical model of the wind-stress based on an empirical orthogonal function decomposition of real data, coupled to a regional GCM of the equatorial Pacific. They found good forecasting skill for ENSO variability prediction, and HCMs have been extensively used for ENSO forecasting since then [63]. Singular value decomposition of observational data has been used in [103], to implement an anomaly model of wind-stress for the equatorial Pacific. The HCM including this model has been used to investigate the role of ENSO-like feedbacks in seasonal variability. In [10], linear regressions on Niño-3 and Niño-4 indexes are used in combination with a red noise term to study the importance of local wind feedbacks in the Tropical Pacific. Singular value decomposition in combination with a stochastic term has been used also in [116]. In these studies, the wind-stress–SST interaction is generally the main point of interest, but other feedbacks are active as well in the ocean–atmosphere system. Changes in wind speed affect evaporation and, as a consequence, surface temperature [80]. Also the freshwater flux is correlated to SST, through the triggering of convective events in the atmosphere [45, 125].

Our aim here is to develop a global HCM that includes all the main atmosphere–ocean feedbacks relevant for the stability of the AMOC, in an approach

that focuses on the quasi-steady state behaviour rather than on variability. As we want to follow an approach as general as possible, we regress all the surface fluxes pointwise on SST. Since the SST variability has a typical extent ranging from regional to basin scale, the atmosphere–ocean interaction is roughly captured by this local approach. In the HCM, two linear perturbation terms dependent on SST are added to the climatology of the forcing fields of the ocean model. A term depending on the local SST anomaly represents the atmosphere–ocean feedbacks that are acting in a statistical steady state. The large-scale changes in the surface fluxes due to the collapse of the AMOC can not be described by these local regressions alone, but are included through a second linear term that depends on the anomalous strength of the overturning circulation itself, measured through the NH annual average SST anomaly. Taken together, the local- and large-scale terms give a simple representation of the atmospheric feedbacks which play a role in the stability of the AMOC.

As a demonstration of concept, our regressions are based on the output of an EMIC (described in section 2.2). The linear atmospheric feedback representations are presented in section 2.3 with results in section 2.4. The performance of the HCM is compared to the one of the original EMIC in section 2.5. With both local and large-scale regression terms, the HCM captures the changes in atmospheric fluxes in response to AMOC changes. The advantages of the HCM over the EMIC are that (i) a more than ten fold decrease in computation time is achieved and (ii) it gives the possibility to selectively investigate the effect of different physical processes on the stability of the AMOC separately.

2.2 THE EMIC SPEEDO

The HCM is constructed from data of the EMIC SPEEDO [93], an intermediate complexity coupled atmosphere, land, ocean, sea-ice general circulation model. The choice for an EMIC is motivated by the fact that multi-thousand year runs are needed to construct the HCM, which is at the moment not feasible with a GCM.

The atmospheric component of SPEEDO is a modified version of Speedy [7, 8, 52, 60, 78], an atmospheric GCM, having a horizontal spectral resolution of T30 with a horizontal Gaussian latitude–longitude grid (approximately 3° resolution) and 8 vertical density levels. Simple parametrization are included for large-scale condensation, convection, radiation, clouds and vertical diffusion. A simple land model is included, with three soil layers and up to two snow layers. The hydrological cycle is represented with the collection of precipitation in the main river basins and outflow in the ocean at specific positions. Freezing and melting of soil moisture is included.

The ocean model component of SPEEDO is the CLIO model [43]. It has approximately a $3^\circ \times 3^\circ$ resolution in the horizontal, with 20 vertical layers ranging in resolution from 10 m to 750 m from the surface to the bottom. The horizontal grid of the ocean model is curvilinear, and deviates from a latitude–longitude one in the north Atlantic and Arctic basins to avoid the singularity of the north pole. A convective adjustment scheme, increasing vertical diffusivity when the water column is unstably stratified, is used in the model. LIM sea-ice model is included in CLIO [45]. A coupler provides the boundary conditions to the components, and performs the interpolations between the different ocean and atmosphere model grids in a conservative way.

Studies conducted both with an EMIC [21, 21] and with a fully implicit ocean model [54] showed the fundamental role of the salinity budget at the southern boundary of the Atlantic ocean in determining the response of the AMOC to freshwater anomalies [86]. The value of the net freshwater transport by the overturning circulation at 35°S , shorthanded M_{ov} , is likely a control parameter that signals the coexistence of two stable equilibria of the AMOC. If M_{ov} is positive, the AMOC is importing freshwater into the Atlantic basin and only the present-day “ON” state of the overturning is stable. If M_{ov} is negative, freshwater is exported out of the basin by the AMOC, and a second stable “OFF” state of the AMOC exists, with reversed or no overturning in the Atlantic ocean.

In the equilibrium solution of SPEEDO, the Atlantic basin integrated net evaporation is overestimated both with respect to most other models and to the few available observations [86]. Furthermore, the zonal gradient of salinity in the south Atlantic is reversed too, with a maximum on the eastern side. The high evaporation over the basin, combined with the low freshwater import by the gyre due to the reversed zonal salinity profile, force the overturning circulation to import freshwater ($M_{ov} = 0.29\text{ Sv}$) in order to close the budget. For these reasons, a small freshwater flux correction is needed in the model for the purpose of our study, since we are interested in the feedbacks connected with a permanent collapse of the AMOC. Following the example of [21], a freshwater increase is applied over the eastern Atlantic, from the southern boundary to the latitude of the Gibraltar strait, summing up to 0.2 Sv . A dipole correction is applied over the southern gyre to reverse the zonal salinity profile, with a rate of 0.25 Sv^1 . All the corrections are performed as a virtual salt flux, keeping the global budget closed with an increased evaporation in the tropical Pacific and Indian oceans. As a consequence of these corrections, the net freshwater transport of the AMOC at the southern boundary of the Atlantic basin becomes negative ($M_{ov} = -0.069\text{ Sv}$). As proposed in [21] and [54], this situation may

¹ The model used in [21] shares the same ocean model component as SPEEDO, but uses ECBilt as the atmospheric model instead of Speedy. In their setup, the basin integrated net evaporation of the Atlantic ocean is underestimated, while the zonal salinity contrast in the southern Atlantic is overestimated. Therefore, their correction has a sign opposite to that here.

allow the coexistence of multiple equilibria of AMOC under the same boundary conditions. Even if the data necessary for the definition of the HCM comes from 300 years of simulations alone, in the testing phase of different freshwater corrections applied to reach the regime where the AMOC can permanently collapse, several tens of thousand years of integrations have been simulated by the EMIC (i.e., changing fresh-water correction and going to equilibrium, testing flux diagnostics, testing whether the collapse of the AMOC is permanent), motivating the use of a fast EMIC.

The surface boundary conditions for the ocean are computed from the atmospheric model as follows. Since the atmospheric boundary layer is represented by only one model layer, near surface values of temperature (T_{sa}), wind (\vec{U}_{sa} , the bold font indicating a vector quantity) and specific humidity (Q_{sa}) are extrapolated from the values of the model lowest full layers. Furthermore, an effective wind velocity is defined to include the effect of unresolved wind variability as $|V_0| = \sqrt{\vec{U}_{sa} \cdot \vec{U}_{sa} + V_{gust}^2}$, where V_{gust} is a model parameter. The ocean model provides through the coupler the values of SST, from which also the saturation specific humidity at the surface (Q_{sa}^{sat}) is computed through the Clausius-Clapeyron equation. With these quantities, the surface boundary conditions for the ocean are computed. The sensible (Φ_{SQ}) and latent heat (Φ_{LQ}) fluxes into the ocean are obtained from the bulk formulas:

$$\begin{aligned}\Phi_{SQ} &= \rho_{sa} c_p C_H |V_0| (T_{sa} - SST), \\ \Phi_{LQ} &= \rho_{sa} L_H C_H |V_0| \min \left[(Q_{sa} - Q_{sa}^{sat}), 0 \right],\end{aligned}\tag{2.1}$$

where ρ_{sa} is the surface air density, c_p and L_H are the specific heat of air and the latent heat of evaporation, respectively, and C_H is a heat exchange coefficient, a model parameter depending on the stability properties of the boundary layer. The parametrization of the radiative fluxes are more complex. For the short-wave (Φ_{SW}) and long-wave components (Φ_{LW}), two and four frequency bands are used, respectively. Transmittance is computed for each band separately, taking into account air density, water content and cloud cover. The total non-solar heat flux (Φ_Q) is just the sum of the different components:

$$\Phi_Q = \Phi_{SQ} + \Phi_{LQ} + \Phi_{LW}.\tag{2.2}$$

Separate parametrization are used for precipitation due to convection (Φ_{Pcv}) and to large-scale condensation (Φ_{Pls}). River runoff (Φ_R) is provided by the land model. The net evaporation (Φ_E) can then be computed as:

$$\Phi_E = \Phi_{LQ}/L_H - \Phi_{Pls} - \Phi_{Pcv} - \Phi_R.\tag{2.3}$$

The wind-stress vector is computed as:

$$\vec{\Phi}_U = \rho_{sa} C_D |V_0| \vec{U}_{sa},\tag{2.4}$$

where C_D is a drag coefficient.

2.3 LINEAR REGRESSIONS

Our aim is to capture the changes in the atmospheric forcing connected with the changes in the ocean state, that is the atmospheric response to a collapse of the AMOC. As motivated in the introduction, we assume that these atmospheric feedbacks can be expressed as functions of SST alone. First, the feedbacks that keep the system in a statistical equilibrium state are always present, and are expressed in our case as a function of local SST. They are extracted from a 200 years long statistical steady state run (CLIM) of SPEEDO. The departure from the steady state arises during an externally forced AMOC collapse, in association with the large-scale SST footprint of a AMOC decline. The feedbacks involved in the collapse are different from the ones acting at the steady state. To study the large-scale feedbacks, a 4000 year experiment was performed, starting from CLIM, with an additional 0.4 Sv freshwater flux centred around southern Greenland during the first 1000 years; this run is referred to as PULSE. In the first hundred years of the experiment, the AMOC collapses and a shallow reverse overturning cell is established in the Atlantic basin. Since in this paper the focus is only on the impact of a complete and steady collapse of the AMOC, we only show the results using the large freshwater anomaly mentioned, that guarantees that the AMOC is brought to a steady reversed state.

The maximum of the meridional overturning streamfunction during the first two hundred years of both PULSE and CLIM runs are shown in figure 2.1 (bottom panel). After the first 1000 years of the experiment, the additional freshwater pulse is released and the model tends to an equilibrium state with no sign of recovery of deep water formation in the northern north Atlantic after 3000 years (top panel of figure 2.1). Taken together, the feedbacks extracted from CLIM and PULSE runs provide the representation of the changes of the atmospheric fluxes during a collapse of the AMOC.

To provide the simplest description of the changes taking place at the ocean-atmosphere interface, the first order approximation is the addition of a linear perturbation term to the climatology of surface atmosphere-ocean fluxes. In particular, we consider a linear regression on SST. This approach is clearly limited, but it is an approximation that gives a consistent representation of the large-scale feedbacks. The results can be successfully used as boundary conditions for the ocean-only model, as will be shown below.

To force the ocean model, we need five surface fluxes: non-solar heat flux (that includes long-wave radiation, latent and sensible heat fluxes), short-wave radiative heating, net evaporation, zonal and meridional wind-stresses. The incoming short-wave radiation is not regressed, and only its average seasonal

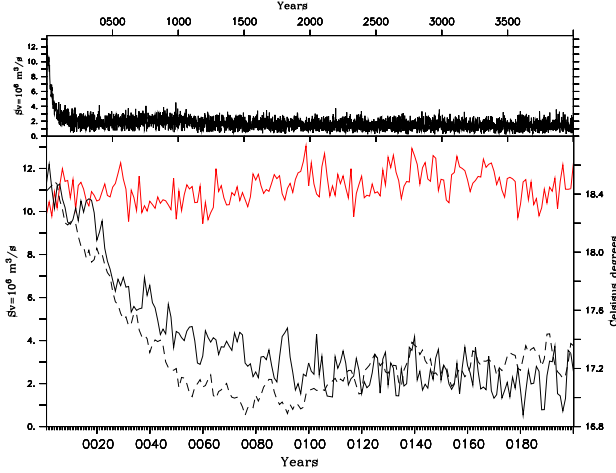


Figure 2.1: Top panel: Maximum AMOC for the entire PULSE experiment, in Sv. Bottom panel: Maximum AMOC for CLIM (red full line) and first 200 years of PULSE (black full line) in Sv (left y-axis). NH average SST in $^{\circ}\text{C}$ (right y-axis) for PULSE (dashed black line).

cycle is retained, since its response to SST is totally mediated through a cloud cover response that is not well represented in the Speedy model [93].

Two linear models are used for regressing data from CLIM and PULSE. The CLIM data is fitted with:

$$\phi(i, j) - \overline{\phi(i, j)} = p_1(i, j) \cdot \left(\text{SST}(i, j) - \overline{\text{SST}(i, j)} \right), \quad (2.5)$$

where $\phi \in \{\Phi_Q, \Phi_E, \Phi_U\}$ is a particular surface flux field to be regressed, p_1 is the model parameter field to be fitted, i (j) is the grid index in the east–west (north–south) direction and the overbar indicates a time average. Monthly data is used in the fit of CLIM data to represent the seasonal cycle. Note that this formulation is a *local* regression, by which we mean a regression between quantities that belong to the same grid cell of the model.

The natural variability signal caught by regressions from equation (2.5) is removed from PULSE data. Only the first 100 years of PULSE are used, since we are interested in the response that can approximately be considered linear. The residual signal $\phi_r(i, j)$ can then be regressed with a second linear model:

$$\phi_r(i, j) = p_2(i, j) \cdot \left(\langle \text{SST} \rangle_{\text{NH}} - \overline{\langle \text{SST} \rangle_{\text{NH}}} \right), \quad (2.6)$$

where the symbol $\langle \rangle_{\text{NH}}$ denotes the average over the NH. In this case the regressor is, for all grid cells, the yearly average SST in the NH, a good indicator

of the state of the AMOC [101], as figure 2.1 suggests (bottom panel, dashed line). Yearly mean data is used for the fit of PULSE. It must be stressed that the last term of equation (2.6) is the average NH SST for the CLIM run, since we are interested in the deviation from the equilibrium state. Consequently, the intercept is set to zero, since the terms involving p_2 need not to have an effect when the climate is in a neighbourhood of CLIM.

All the regressions are computed with the *lm* (linear model) function provided in the R statistical software, version 2.8.0 [106]. The regressions are computed through a least square technique, and we require a statistical significance higher than the 95 percentile, discarding all the fits with a *p-value* (provided by *lm* itself) higher than 0.05. This equals to discarding a fit if the probability of having the same result using random data is higher than 5%. When this occurs the fit is considered unsuccessful, and only the climatological value of CLIM ($\overline{\phi(i, j)}$ in equation (2.5)) is kept and both $p_1(i, j)$ and $p_2(i, j)$ are set to zero. The output of the fitting procedure shows very weak sensitivity to the chosen significance level.

The same regression procedure was applied also to the output of the uncorrected original SPEEDO model. The results obtained from the two models, with or without freshwater flux corrections, are consistent on both qualitative and quantitative grounds. A partial exception is the southern ocean and the Labrador sea, where the strength of the feedbacks is different. An analysis of these differences is beyond the scope of the present study, but may be associated with changes in sea-ice cover in the two models.

We now give the formulation of the boundary conditions for the ocean-only model to be forced by our “climatology with feedbacks”. The surface heat flux into the ocean is computed as a combination of the regressions and a restoring term to the climatology:

$$\begin{aligned}
 \Phi_Q(i, j) = & \overline{\Phi_Q(i, j)} + p_1^{\Phi_Q}(i, j) \cdot (SST(i, j) - \overline{SST(i, j)}) \\
 & + p_2^{\Phi_Q}(i, j) \cdot (\langle SST \rangle_{NH} - \overline{\langle SST \rangle_{NH}}) \\
 & + \overline{\Phi_{SW}(i, j)} \\
 & + \frac{\rho_{sa} c_p \overline{V_0(i, j)}}{\tau} \cdot (\overline{SST(i, j)} - SST(i, j)),
 \end{aligned} \tag{2.7}$$

where $p_1^{\Phi_Q}$ and $p_2^{\Phi_Q}$ are the local and large-scale regression parameters for the heat flux, ρ_{sa} and $\overline{V_0(i, j)}$ are fixed climatological values and the relaxation time τ is chosen to be 55 days for the ocean, consistently with the bulk formula of the coupled model of equation (2.1).

The net evaporation flux is computed in three steps. First, the deviations from the climatological values, $\delta\Phi_E$, are computed at each grid cell:

$$\begin{aligned}\delta\Phi_E(i, j) = & p_1^{\Phi_E}(i, j) \cdot \left(SST(i, j) - \overline{SST(i, j)} \right) \\ & + p_2^{\Phi_E}(i, j) \cdot \left(\langle SST \rangle_{NH} - \overline{\langle SST \rangle_{NH}} \right),\end{aligned}\quad (2.8)$$

where $p_1^{\Phi_E}$ and $p_2^{\Phi_E}$ are the regression parameters for the net evaporation flux. Then, the global integral of the deviations, $\Delta\Phi_E$, is computed on the model grid and the budget imbalance is set to zero. The total freshwater flux reads then:

$$\Phi_E(i, j) = \overline{\Phi_E(i, j)} + \delta\Phi_E(i, j) - \Delta\Phi_E/\Sigma, \quad (2.9)$$

where Σ is the ocean surface area.

For the wind-stress vector, only the output of the regressions is used:

$$\begin{aligned}\vec{\Phi}_U(i, j) = & \overline{\vec{\Phi}_U(i, j)} + \vec{p}_1^{\vec{\Phi}_U}(i, j) \cdot \left(SST(i, j) - \overline{SST(i, j)} \right) \\ & + \vec{p}_2^{\vec{\Phi}_U}(i, j) \cdot \left(\langle SST \rangle_{NH} - \overline{\langle SST \rangle_{NH}} \right),\end{aligned}\quad (2.10)$$

where $\vec{p}_1^{\vec{\Phi}_U}(i, j)$ and $\vec{p}_2^{\vec{\Phi}_U}(i, j)$ are the vectors of the regression parameters for local and large-scale regressions respectively, for the two components of the wind-stress. Over sea-ice, a fixed climatology of air-ice fluxes is used. When sea-ice is present, weighting is applied by the model to the surface fluxes multiplying by the fractional ocean area ($1 - \varepsilon(i, j)$), where $\varepsilon(i, j)$ is the fractional sea-ice cover of the cell.

The technique described returns the rate of change of the field with SST or $\langle SST \rangle_{NH}$ only in those areas where a linear regression is statistically significant. Furthermore, setting the regression parameters to zero still leaves a constant climatology that can be used as boundary condition for the ocean model. We thus have the complete control over which feedbacks are acting at the ocean-atmosphere interface, and we can selectively investigate their individual or collective effect.

2.4 RESULTS

2.4.1 Local regressions

The fitting procedure for CLIM data is generally successful and the results of the regressions on CLIM data are reported in figures 2.2 and 2.3.

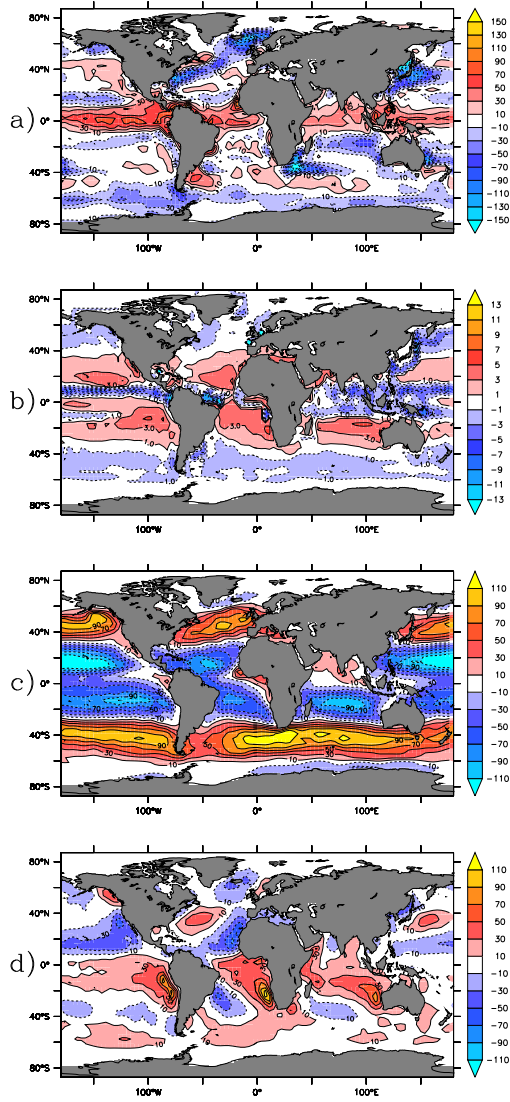


Figure 2.2: Average value of the regressed fields from CLIM data ($\overline{\phi(i, j)}$ in equation (2.5)), weighted by the fractional ocean area ($1 - \varepsilon(i, j)$). a) Total heat flux in W m^{-2} , positive downwards. b) Net evaporation in mm/day . c) and d) are the zonal and meridional components of wind-stress respectively, in 10^{-3} Pa .

Name	Model	Freshwater anomaly	Total length (years)
CLIM	EMIC	None	200
PULSE	EMIC	0.4 Sv	4000
regCLIM	HCM	None	5000
regPULSE	HCM	0.6 Sv	5000

Table 2.1: List of the model runs described in the text.

In figure 2.2, the average value of the regressed fields is reported ($\overline{\phi(i, j)}$ in equation (2.5)). The total heat flux (including short-wave radiation) is shown in figure 2.2. The net evaporation includes the river runoff. The values of the regression parameter p_1 are shown in figure 2.3 for all the regressed fields. In both figures 2.2 and 2.3 the values are weighted by the fractional free ocean surface of the cell to compensate for the effects of average sea-ice cover. The effect of changes in sea-ice cover are not included into the regressions, as the effect of sea-ice is taken into account by CLIO model. As discussed below, the changes in sea-ice can strongly modify the feedbacks (compare figures 2.3 and 2.5).

For all the regressed fields, the contribution to the fluxes of the local regression terms can be important compared to the average value, in particular at the western boundaries and outside the equatorial and polar regions. This is clear when we consider the SST variability on a daily basis; the root of the variance is well above 1°C everywhere in the subtropical and subpolar ocean, with peak values of about 7°C close to the NH western boundaries (not shown).

The linear regressions only capture part of the natural variability of CLIM fluxes, but the error is generally lower than 10% of the original field over a major part of the ocean (not shown).

Apart from the standard damping on SST that also operates in ocean-only models driven by a prescribed atmosphere, the atmospheric control over the atmosphere–ocean heat flux counteracts this damping in many regions, in particular in the tropics and at high latitudes (positive values in figure 2.3 a). This means that the linear feedback for the heat flux is not damping the SST anomalies. Relevant exceptions are the equatorial ocean, the central north Atlantic, the northern portion of the Southern Ocean and other smaller areas. It should be noted that in the polar areas, the sea-ice cover determines the effective feedback in the heat flux, and often changes the sign of the feedback. The exact mechanism of this feedback is discussed in more detail in section 2.4.2.

To investigate the origin of the pattern of the local heat feedback outside the polar regions, the same regression procedure was applied to each compo-

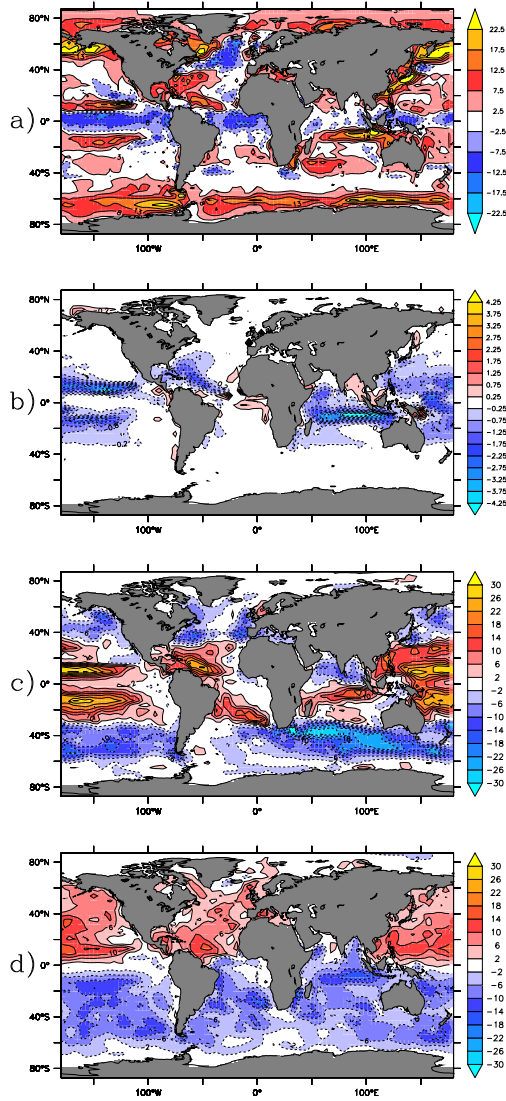


Figure 2.3: As in figure 2.2, but for the local regression parameter p_1 . The units are the same of figure 2.2, divided by $^{\circ}\text{C}$. In panel a, only the non-solar heat flux is considered.

ment of the heat flux separately, namely sensible and latent heat fluxes and long-wave radiation (not shown). The change in the latent heat release is the most important component of the heat flux change. The feedback of sensible heat flux is slightly weaker in magnitude, and is positive with the only relevant exceptions of the North Atlantic and the equatorial ocean. The long-wave radiation feedback follows the same pattern, and is the weakest term. As first noted in [34], the sign of the heat flux feedback from equation (2.1) depends to first order only on the relative change of T_{sa} and SST, if the wind is assumed constant. A positive feedback is possible only if the change in T_{sa} is larger than the one in SST. This is almost always true in our model in the areas where the heat feedback is positive, as we find when T_{sa} is regressed on SST (not shown).

A plausible explanation of this positive heat feedback, at least at low and mid latitudes, is given by the convection–evaporation feedback mechanism as proposed by [125]. There is a strong resemblance between the patterns of increased convective precipitation and those of weaker latent heat loss at higher SST. This suggests that, in the tropical and subtropical areas where a positive heat flux feedback is observed, a positive SST anomaly is associated with anomalous convergence of wet air that both contributes to the reduction of evaporation² and enhances precipitation if convection is triggered. Regression of surface pressure on SST also supports this hypothesis, since higher SSTs correlate with lower surface pressure in the tropical and subtropical areas. Regarding net evaporation (figure 2.3 b), a weak increase is observed at higher SST over most of the ocean. On the contrary, in most of the tropical areas the increase in convective events leading to increased precipitation dominates the freshwater feedback (basically, the blue areas of figure 2.3 b), as discussed above.

In the case of wind-stress, a decreased magnitude is observed in connection with higher SST (compare figure 2.3 c and d with the mean fields of figure 2.2). The term $|V_0|$ of equation (2.1) is regressed on the local SST, confirming that over most of the ocean at low and mid latitudes lower than average winds are observed in association with higher than average SSTs (not shown), implying lower heat transfer through the interface. The correlation decreases moving poleward and the mechanism involved is basically the wind–evaporation feedback [80], that connects higher evaporation (lower SST) with stronger winds. The fact that we do not observe stronger winds where an increase of convective precipitation is found is not surprising, since the parametrization of convection does not affect the horizontal wind field [78]. A positive correlation between wind speed and SST is observed only in the western part of the subtropical gyre of the Southern Hemisphere (SH) of the Atlantic ocean, south of Greenland and in the Labrador sea, in the northeastern part of the subpolar gyre of Pacific ocean, and in some other smaller regions. Even though the negative wind feed-

² The reduction of evaporation is mainly due to weaker winds.

back is thought to be dominant, some evidence for a positive feedback has been found for the Kuroshio extension area, in the northeastern Pacific [82, 117]. The best known wind–SST feedback mechanism where the wind response to SST anomalies is central is the Bjerknes’ feedback in the equatorial Pacific areas, in connection with the ENSO [12]. The fundamental coupled variability of the equatorial ocean–atmosphere system is that of a decrease of the western Pacific trade winds in response to a positive anomaly of SST in the eastern equatorial Pacific. Even though the model has too low resolution to exhibit a realistic ENSO [93], a weakening of the trade winds in the western and central equatorial ocean is captured by the linear regressions (figure 2.3 c) and is consistent with the anomaly patterns connected with ENSO [24]. The stronger convective precipitation detected in the western Pacific at higher SSTs may be a sign of anomalous convergence of the low level atmospheric circulation, again in agreement with what shown by [24]. The origin of the dipole structure of the meridional wind feedback between NH and SH (figure 2.3 d) is basically a reflection of the weaker dominant winds at higher SST.

2.4.2 Large-scale regressions

Moving to the results of *large-scale* regressions, it must be kept in mind in the interpretation of the results that the fit is performed only on the residuals of *local* regressions, not on the full data of PULSE and that the fit is performed on a decreasing quantity, the NH average SST.

The collapse of the AMOC causes a decrease in the NH average SST of about 1.2°C . A weaker change of opposite sign is observed over the Southern Ocean (approximately 0.4°C). This NH–SH temperature dipole is a robust feature of different models, and is connected with lower northward heat transport in the Atlantic ocean, as already found in [101]. The changes in the heat flux are mainly captured by the large-scale regression parameter alone. This can be evinced comparing the large-scale heat flux parameter and the diagnosed changes in the flux from the coupled model, and is connected with the larger magnitude of the large-scale parameter. The main response of the heat flux after the overturning collapse, not considering changes in the sea-ice cover (figure 2.4 a), would be that of an increased heat extraction from the ocean in the NH ($9.9\text{ W m}^{-2}\text{ }^{\circ}\text{C}^{-1}$ on average). When the effect of a changing sea-ice cover is included in the computation of the heat feedback (figure 2.5 b), its sign changes in the high latitudes of the NH ($-9.6\text{ W m}^{-2}\text{ }^{\circ}\text{C}^{-1}$ on average in the NH), which means that heat released to the atmosphere decreases. This result is in contrast with what the regression parameter p_2 suggests, but consistent with the sign of the effective regression parameter. The difference is explained

below. The net heat flux, weighted by the ice-free area $(1 - \varepsilon)$, can be written as:

$$\phi_Q = (1 - \varepsilon)(\overline{\phi_Q} + \partial \phi_Q / \partial SST + \partial \phi_Q / \partial \langle SST \rangle_{NH}). \quad (2.11)$$

$p_2^{\phi_Q}$ is simply $\partial \phi_Q / \partial \langle SST \rangle_{NH}$ while the effective parameter is:

$$\begin{aligned} p_{2,eff}^{\phi_Q} &= \partial(\phi_Q \cdot (1 - \varepsilon)) / \partial \langle SST \rangle_{NH} \\ &= (1 - \varepsilon) \partial \phi_Q / \partial \langle SST \rangle_{NH} - \phi_Q \partial \varepsilon / \partial \langle SST \rangle_{NH} \\ &= (1 - \varepsilon) p_2^{\phi_Q} - \phi_Q \partial \varepsilon / \partial \langle SST \rangle_{NH}. \end{aligned} \quad (2.12)$$

The second term on the right hand side of equation 2.12 describes the changes in sea-ice cover in response to SST changes. This term is larger than the first term over most of the Northern North Atlantic. Sea-ice cover changes determine the sign change in the large-scale heat feedback term. A similar reasoning holds for the local feedback. In general, the NH-NH heat flux dipole seen in figure 2.4 a is driven by the decrease of NH near-surface temperature, that follows a pattern similar to that of SST (figure 2.6), but with stronger sensitivity to AMOC changes everywhere except for the southern mid latitudes. This amplification of the SST signal, in particular in the atmosphere of the high latitudes of NH, is a consequence of the appearance of sea-ice during winter. Without sea-ice changes, these differential variations in SST and atmospheric temperature would tend to produce an increased upward heat flux in the NH (figure 2.4 a). This increased heat loss is more than counteracted by the decrease in open ocean area; the increased ice cover effectively drives the cooling of atmospheric temperatures above the North Atlantic. This can be seen from the changes in the heat flux diagnosed from the coupled model including the insulating effect of sea-ice (figure 2.5 c) and this is confirmed by the *large-scale* regression parameter computed including the effect of sea-ice (figure 2.5 b). This “effective” regression parameter is the result of the same fitting procedure, applied in this case to the surface heat flux weighted by the actual sea-ice cover and not to the complete heat flux. The results for the local (large-scale) regression are those shown in figure 2.5 a (b). As a consequence, this regression parameter gives a better representation of the feedbacks that the ocean effectively senses (including the effect of sea-ice). Note that the HCM only uses p_1 and p_2 , and not the effective response coefficients. The changes in sea-ice cover result from explicitly resolved ice dynamics and thermodynamics.

At low and mid latitudes in the NH the changes are due to reduced evaporation in response to lower SST and, at low latitudes, to lower wind speed. The changes in the surface long-wave radiation budget are smaller in magnitude,

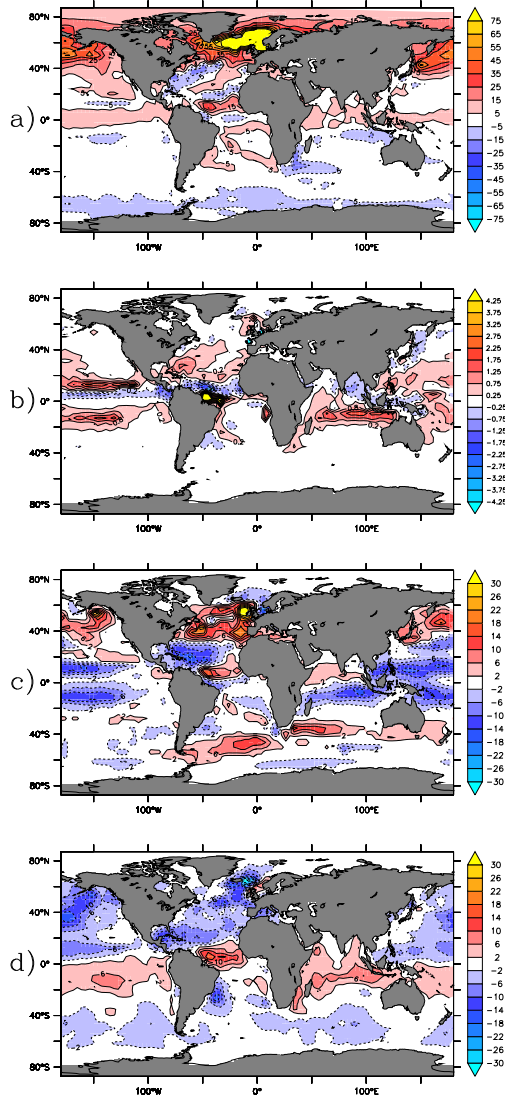


Figure 2.4: As in figure 2.2, but for the large-scale regression parameter p_2 . The units are the same of figure 2.2, divided by $^{\circ}\text{C}$ In panel a, only the non-solar heat flux is considered. In panel b, the signal of the freshwater pulse has been removed from the source data.

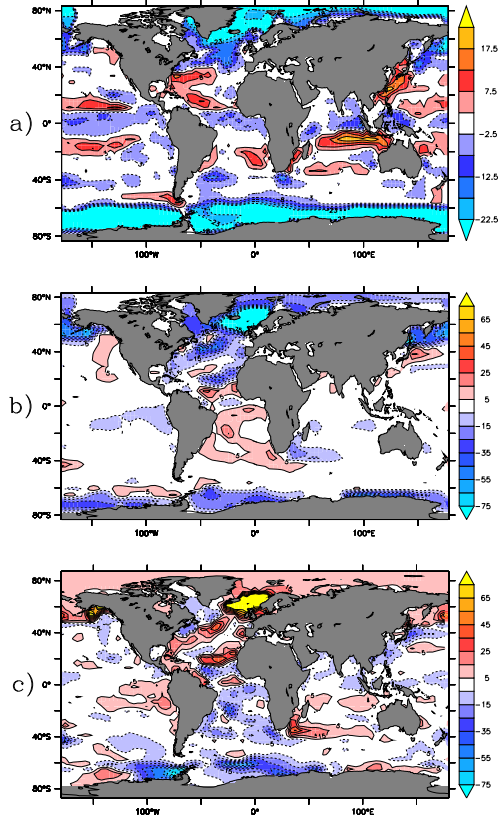


Figure 2.5: Effective feedbacks for heat flux (short wave radiation excluded), when changes in sea-ice are considered (see text). Effective regression parameters for the heat flux, computed including the effect of changes in sea-ice (p_1 in panel a and p_2 in panel b). Also the change in the heat flux, as directly diagnosed from the coupled model, is shown in panel c, computed as the difference in ice-weighted heat flux from years 91-100 and 1-10 of PULSE. Note that a different colour scale is used in the top panel.

and amount to an increased net emission of long-wave radiation almost everywhere in the NH except from the GIN seas. This effect has been observed in other model experiments and is connected with the reduced downward long-wave radiation flux over compensating the decreased black body emission at lower SSTs [65]. The decrease in the downward long-wave flux is an effect of a drier atmosphere, and partly balances the reduced latent heat flux. These changes in heat flux amount to a positive feedback on an AMOC anomaly when the effect of sea-ice is included, favouring a decrease of the surface density in the deep water formation areas of the North Atlantic in connection with weaker overturning circulation.

The patterns of the net evaporation change (figure 2.4 b) are consistent with the findings of [101] (their figure 9 e, with opposite sign). The AMOC collapse causes a reduction of net evaporation over the tropical and subtropical NH and over the tropical SH, due to lower SSTs (figure 2.6). In the few areas where an increase in evaporation is observed (basically the north equatorial oceans), this is due to stronger winds. At low latitudes, a significant change of the precipitation patterns also plays a role, with a dipole pattern centred around the equator, and positive to the south. This southward shift of the intertropical convergence zone (ITCZ) produces the strongest precipitation increase over the Amazon river basin. This response of the Hadley cell is connected with the southward shift of the latitude of maximum heating, and has been observed consistently in different climate models [59, 65, 101] and in an idealised framework too [31]. A similar, though weaker, pattern of precipitation change is observed in the Pacific and Indian oceans. The increased precipitation over the entire southern Atlantic more than compensates for the increased evaporation due to higher SST in this part of the basin. A slow down of the hydrological cycle over Europe is detected as two negative peaks off the coast of France and in the North sea. On a global scale, the regressions of PULSE residuals determine an evaporation increase of $0.13 \text{ mm day}^{-1} \text{ }^{\circ}\text{C}^{-1}$. Therefore, our linear approach is not conserving the ocean water mass and needs a budget closure correction when used as boundary condition for the ocean, as implemented in equation (2.9).

In the case of wind-stress, the response of the atmosphere is somewhat less straightforward to understand, and it deserves a longer discussion. For what concerns the meridional wind-stress, the changes in the low and mid latitudes are driven by the response of the zonally averaged temperature profile to the AMOC collapse. The equator to pole temperature difference increases by approximately 4°C in the NH. In the SH, the opposite is true, with a smaller change. These changes are clearly mirrored in the zonally averaged wind-stress. Stronger southward wind blows on the ocean with a collapsed AMOC in the NH up to 50°N . The situation is similar in the SH, but with a weaker circulation down to 40°S , following the opposite change in the zonally averaged temper-

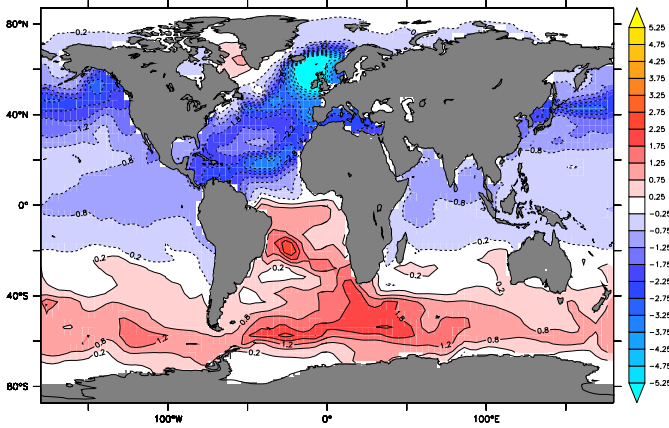


Figure 2.6: Difference in SST ($^{\circ}\text{C}$) between the years 91–100 of PULSE experiment and the mean state of CLIM.

ature. The zonal winds over the Southern Ocean are also reduced. A more peculiar feature is observed in the north Atlantic. A pressure anomaly dipole between Greenland and northeastern Atlantic develops, with positive sign to the east, in connection with the differential cooling between these two regions (stronger cooling over eastern Atlantic). This in turn determines an anomalous anticyclonic circulation centred north of Scotland, with impacts on both the meridional and zonal wind-stress. Referring to our regressions, the changes due to the AMOC collapse in the tropical regions are already caught by the local regression parameter (p_1 , figure 2.3 c and d). This can be understood considering that the change in SST due to the AMOC collapse (figure 2.6) is a dipole centred at the latitude of the southern tropic (at the equator in the Atlantic ocean) and positive to the south of it, with an amplitude of a few degrees. In fact, the changes due to the overturning collapse are overestimated by the local regressions, and p_2 (figure 2.4 c and d) amounts to a correction opposite to p_1 . The positive values of p_2 for meridional wind-stress in the intertropical regions (figure 2.4 d) signal the southward shift of the ITCZ, that is an anomalous southward wind with decreasing NH average SST, not represented by the local regressions. Also the anomalous anticyclonic circulation is reproduced in the large-scale regressions by the dipoles over northeastern Atlantic (positive to the south and to the east). The impact on AMOC stability of wind-stress feedbacks has been investigated in the recent paper by [3], where a simple zonally averaged atmospheric model was used. Even though it is quite difficult to compare their results with the results from a GCM like SPEEDO, the general picture

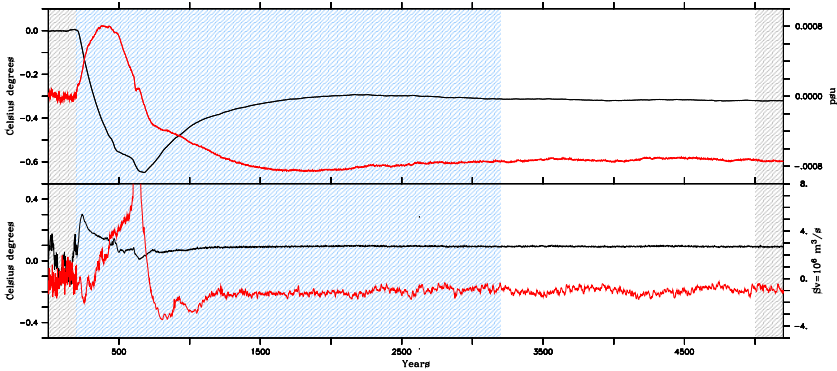


Figure 2.7: Deviation from CLIM average in regCLIM of four quantities: global average sea temperature (top panel, black, left y-axis), global average salinity (top panel, red, right y-axis), global average SST (bottom panel, black, left y-axis) and maximum AMOC (lower panel, red, right y-axis).

is similar. The atmospheric circulation in the NH is strengthened, while the opposite is true for the SH. The magnitude of the changes in SPEEDO is close to their lowest estimates.

2.5 HCM TEST

The HCM consists of the ocean component of SPEEDO (i.e., CLIO) and the dynamic boundary conditions described in the previous section. It was tested by comparing its results with the original SPEEDO model. The first experiment (regCLIM) starts from the end state of the ocean of the CLIM run. The model is forced only by the local regressions (values of p_2 set to zero) for 3000 years. Next, all the large-scale regressions are also switched on, and the model runs for 2000 years more.

Results of the regCLIM run are shown in figure 2.7. On the top panel, the deviation from CLIM mean value of the global average sea temperature (salinity) is reported in black (red). The area shaded in grey on the left margin of figure 2.7 marks the (200 years) data of the CLIM run. The light blue area marks the first 3000 years of the regCLIM of the ocean-only model, with only local regressions active. To estimate the theoretical equilibrium state of the model, we fit the global average sea temperature and salinity from years 1201-5200 of regCLIM with the function:

$$f(t) = a_1 \sin\left(\frac{t + a_2}{a_3}\right) \exp\left[-\frac{t + a_2}{a_4}\right] + B, \quad (2.13)$$

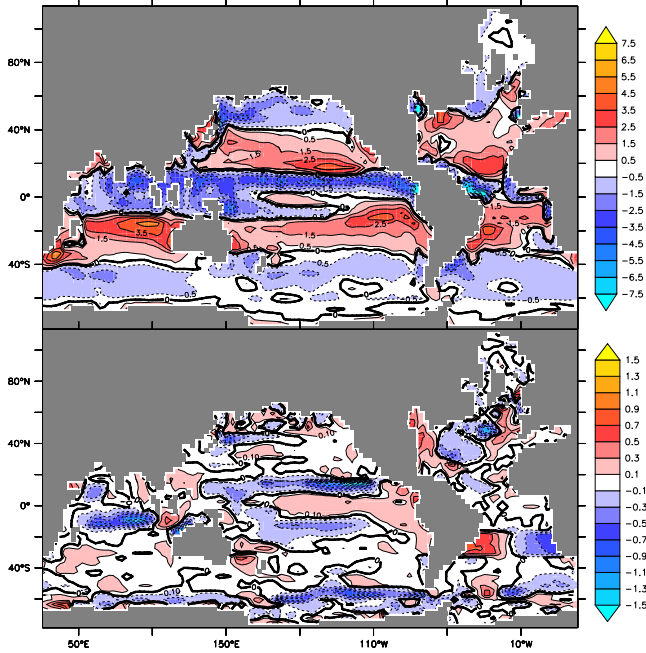


Figure 2.8: In the top panel, the surface density flux for CLIM is shown in $10^{-6} \text{ kg m}^{-2} \text{ s}^{-1}$. In the bottom panel, the difference of the same quantity between the last 200 years of regCLIM and CLIM. Different colour scales are used in the two panels. In the figure, the grid of the ocean model is used (distorted in the north Atlantic and Arctic), to avoid interpolation errors.

where t is time, a_1, \dots, a_4 are the fit parameters, and B is a constant background that represents the state of the system at infinite time. The theoretical equilibrium state computed from this procedure is 0.31°C colder and $7.2 \cdot 10^{-4}$ psu fresher than the coupled CLIM run. Little drift, but a substantial reduction of the variability due to the restoring term, is observed in the global average SST (figure 2.7, black line in the bottom panel). The NH average SST increases by 0.18°C (difference between last 200 years of regCLIM and CLIM). The maximum of the AMOC is, at the end of regCLIM, approximately 1 Sv weaker than in the CLIM run (bottom panel of figure 2.7, in red). The AMOC, as the left bottom panel of figure 2.11 shows, is weaker and approximately 500 m shallower in the HCM. The freshwater transport by the AMOC at 30°S in the last 200 years of regCLIM (grey shaded area on the right of figure 2.7)

is $M_{ov} = -0.06$ Sv. To keep $M_{ov} < 0$, the freshwater corrections described in section 2.2 are 50% stronger than in the fully coupled model.

To investigate the origin of the changes in the AMOC strength, we diagnose the surface fluxes of density for the CLIM and regCLIM runs. The surface density flux Φ_ρ can be estimated using the formula [48, 110]:

$$\Phi_\rho = -\frac{\alpha}{c_p}\Phi_H + \rho_0\beta\frac{\Phi_E \cdot SSS}{1 - SSS \cdot 10^{-3}}, \quad (2.14)$$

where $\alpha = -1/\rho_0(\partial\rho/\partial T)$, $\beta = 1/\rho_0(\partial\rho/\partial S)$, Φ_H is the total surface heat flux into the ocean ($\Phi_H = \Phi_Q + \Phi_{SW}$), ρ_0 is the reference water density, SSS is the surface salinity measured in ppt. The density flux into the ocean is shown in figure 2.8 in units of $10^{-6} \text{ kg m}^{-2} \text{ s}^{-1}$ for the CLIM run (top panel). The effect of sea-ice cover is taken into account in the computation of the density flux, and the model grid (distorted over north Atlantic and Arctic) is used to avoid interpolation errors. The difference between the fluxes from the regressions in the last 200 years of regCLIM and CLIM is reported in the bottom panel of figure 2.8. Even if the changes are generally small (note the different colour scales in the figure), when the difference is averaged over the GIN seas and the Arctic Mediterranean (taking as southern boundaries the Bering strait and the latitude of the southern tip of Greenland), we find that the density flux decreases by $2 \cdot 10^{-8} \text{ kg m}^{-2} \text{ s}^{-1}$. This value represents a 10% decrease of the average density flux over the same area, that nicely fits the relative change in maximum overturning strength.

The definition of the HCM, that does not include any high frequency stochastic component, causes a strong reduction of variability, but low frequency variability of the system seems to be preserved. To show this, a multi taper method (MTM) analysis [40] was performed on the time series of the maximum of overturning streamfunction of the Atlantic. The analysis is performed on the yearly data of CLIM (a longer control run is used, 1000 years long) and the last 1000 years of regCLIM (figure 2.9). At the lower end of the spectrum, energy is concentrated at similar frequencies in the two models, below approximately 0.02 year^{-1} . At higher frequencies, instead, the broad peaks found in the HCM between 0.02 year^{-1} and 0.09 year^{-1} are not present in the original coupled model, while the peaks found above 0.1 year^{-1} in CLIM are lost in the HCM. Also the first empirical orthogonal function of SST computed from the HCM resembles the one from CLIM only in the northwestern Atlantic. This approach is thus limited when the internal variability of the ocean is of interest, but in the present work the focus is only on the quasi-equilibrium response. Atmospheric noise and lagged correlations are probably needed to better represent and excite the modes of variability of the system.

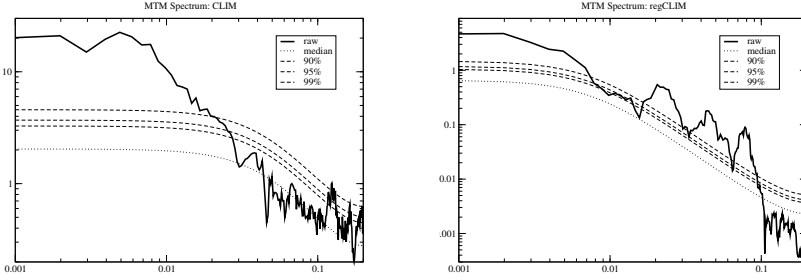


Figure 2.9: MTM spectra of the time series of the maximum AMOC (solid lines) for CLIM (left) and regCLIM (right). The dashed smooth lines represent, from the lowest to the highest, the estimated red noise background and the median, 90%, 95% and 99% significance levels associated with it. In both cases, the resolution is $(5 \text{ years})^{-1}$ and 7 tapers were used. Time series are 1000 years long.

As a final test, a pulse experiment was performed in the HCM. In this test, that will be shorthanded as regPULSE, we apply the same freshwater anomaly as in PULSE (see section 2.3), also increased by 50% as the corrections already applied in regCLIM. The initial conditions for regPULSE are provided by the final state of regCLIM: year 5200 of figure 2.7. In regPULSE, as in PULSE, the anomaly is applied for 1000 years, letting the model reach a new equilibrium afterwards. We focus our analysis on the response of the system during the first hundred years of the run, where the regressions are expected to be significant.

The AMOC maximum for regPULSE is reported in figure 2.10 as a dashed line. The response of the AMOC in regPULSE, when measured by this quantity, follows closely the one in PULSE. The only substantial differences are its lower initial condition and the weaker variability of the regPULSE signal. The weaker variability of regPULSE signal is no surprise, considering the fact that our regressions do not add any high frequency variability to the system, depending only on SST.

Looking at the entire overturning streamfunction of the Atlantic, the results are also encouraging. On the right hand side of figure 2.11, the overturning of the collapsed state that is established after the first 100 years of the pulse experiment are compared in PULSE and regPULSE. In the top right panel of figure 2.11, the streamfunction of years 101-110 of PULSE run is shown as a reference. The difference between regPULSE and PULSE during the same years is reported below. The results of the HCM are in good agreement with those of SPEEDO, showing a reversed cell only slightly weaker than in PULSE. The largest differences are at the southern border of the Atlantic basin, likely

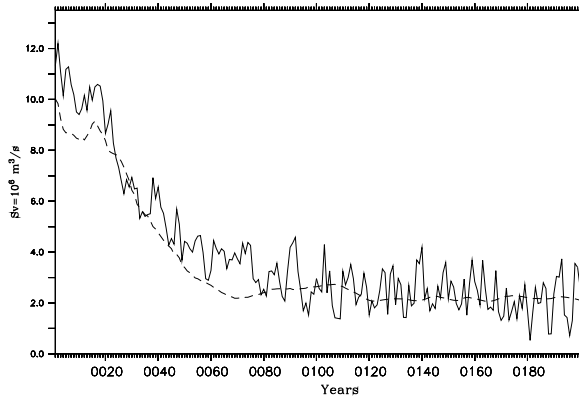


Figure 2.10: Maximum AMOC for first 200 years of PULSE (full line) and regPULSE (dashed line) in Sv.

in connection with the general underestimation of the density flux over the southern ocean (figure 2.8). For what concerns the barotropic streamfunction during the pulse experiments, the only significant differences are found in the southern ocean (not shown). Over the Pacific sector of the Southern ocean, the underestimation of the barotropic streamfunction represents about 20% of the transport predicted by PULSE. This discrepancy is probably connected with an overestimation of the decrease of the southern westerly winds in the regressed forcing in response to the collapse of the AMOC.

2.6 SUMMARY AND CONCLUSIONS

In this paper we described a new technique for developing a global HCM that includes a basic representation of the feedbacks due to the ocean–atmosphere interaction, relevant for the stability of the AMOC. The steady state feedbacks of the system were represented through linear regression terms depending on the local deviation of SST from its mean value. The large-scale response of the atmosphere to an externally forced AMOC collapse is included with a regression on the NH hemisphere average temperature.

The results of the regressions give a quantitative representation of the changes in the surface fluxes that is consistent with other model experiments [59, 65, 101]. In particular, we can detect the changes in heat flux at the surface due to the cooling of the NH after a AMOC collapse. Significant changes are observed also in the freshwater flux, in connection with the response of the general circulation in the atmosphere to the changes in the equator to pole temperature profile, that determine the response of the winds as well. The boundary condi-

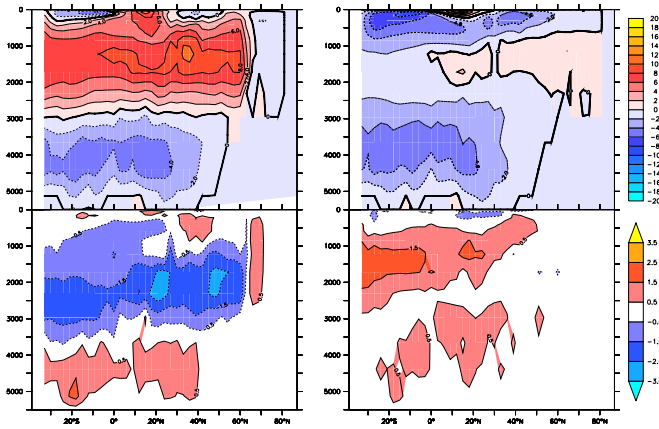


Figure 2.11: Overview of overturning streamfunction in the various models. In the top panels, AMOC for the CLIM mean state (top left) and for years 101 to 110 of PULSE (top right) are shown. The shaded contours are every 2 Sv, the red filling is for positive values, blue for negative. The thick line is the zero contour. In the left bottom panel, the difference of the overturning streamfunction between the last 200 years of regCLIM and the CLIM mean state is shown. In the right bottom panel, the difference of the overturning streamfunction between years 101 to 110 of regPULSE and PULSE runs. The contours in the lower panels are every 1 Sv.

tions computed in section 2.3, were then successfully used as a dynamic forcing for an ocean-only model.

This ocean forced by a “minimal atmospheric model” guarantees a decrease of the computation time between ten and twenty times with respect to the original coupled model. The ocean model forced by the regressions which form the HCM reaches a steady state close to the one of the original coupled model. Furthermore, an experiment is performed where the AMOC is collapsed in both the fully coupled model and in the ocean forced by the regressions. The two results are in good agreement. This enables us to proceed to further use the HCM to investigate the impact of the atmospheric feedbacks on the stability of the AMOC. In particular, the formulation of the forcing shown in section 2.3 enables us to selectively choose which fluxes are fixed to a climatological value, and which ones are computed dynamically as a function of SST. We can thus investigate the impact of each feedback separately on quantitative grounds, and we can aim at a deeper understanding of the main physical processes involved in the collapse and recovery of the AMOC. It is also important to analyse the response of the HCM to weaker freshwater anomalies. Reducing the anomaly that forces

the AMOC collapse, the atmospheric feedbacks are likely to play an increasingly dominant role.

The model can obviously be extended in many ways. Using higher order (nonlinear) models in the data fit is unlikely to be worth the effort. The study of the role of atmospheric noise and of correlations lagged in space and time, and their inclusion in the HCM, may instead greatly improve the representation of atmosphere–ocean interaction with respect to the variability of the AMOC.

As a final remark, we want to stress that our technique to design the HCM is general. We do not rely on any ad-hoc assumption connected with the nature of the EMIC that was used for this work. For this reason, this technique is potentially interesting for many other problems (apart from the stability of the AMOC) where a computationally efficient, simple representation of the ocean–atmosphere interaction is desired. For instance, instead of using data from the atmospheric component of SPEEDO, the ocean component could be coupled to a statistical atmosphere derived from a state-of-the-art coupled climate model or from reanalysis data, at least for the computation of local regressions.

SENSITIVITY OF THE ATLANTIC MERIDIONAL
OVERTURNING CIRCULATION TO SOUTH ATLANTIC
FRESHWATER ANOMALIES.

The sensitivity of the Atlantic Meridional Overturning Circulation to changes in basin integrated net evaporation is highly dependent on the zonal salinity contrast at the southern border of the Atlantic Ocean. Biases in the freshwater budget strongly affect the stability of the AMOC in numerical models. The impact of these biases is investigated, by adding local anomaly patterns in the South Atlantic to the freshwater fluxes at the surface. These anomalies impact the freshwater and salt transport by the different components of the ocean circulation, in particular the basin-scale salt-advection feedback, completely changing the response of the AMOC to arbitrary perturbations. It is found that an appropriate dipole anomaly pattern at the southern border of the Atlantic Ocean can in fact collapse the AMOC entirely even without a further hosing. The results suggest a new view on the stability of the AMOC, controlled by processes in the South Atlantic.

This chapter has been published as:
A. A. Cimadoribus, S. S. Drijfhout, M. den Toom and H. A. Dijkstra. Sensitivity of the Atlantic Meridional Overturning Circulation to South Atlantic freshwater anomalies. *Clim. Dyn.*, 39:2291–2306, 2012.

3.1 INTRODUCTION

The instability of the Atlantic Meridional Overturning Circulation (AMOC) is often invoked to explain the paleoclimatic evidence of abrupt climate change in North Atlantic areas [37, 107]. Also, the possibility of a collapse of the AMOC, triggered by melt water discharge due to global warming, has been suggested [66]. These hypotheses originate from the seminal work of Stommel [99], who suggested a view of the AMOC as a two-dimensional circulation between a tropical and a polar box, driven by density differences between the boxes. In this simple view, multiple equilibria under the same boundary conditions can exist: an ON AMOC, dominated by the dense water production in the north of the basin (due to the strong heat flux) and a reverse OFF circulation with downwelling in the tropical areas (due to the strong evaporation). The Stommel model captures the central non-linearity involved: the present-day AMOC is maintained by a positive salt-advection feedback between the northward transport of high salinity waters in the upper ocean and the salinity (and, as a consequence, density) of northern North Atlantic waters.

Although an obvious oversimplification of the real system, Stommel's results have provided a minimal explanation for the hysteresis behaviour of the AMOC in several other models of higher complexity. An abrupt collapse of the AMOC in response to a quasi-equilibrium increase in freshwater forcing in the North Atlantic, not followed by any spontaneous recovery, has been reported in various ocean and climate models of different complexity [50, 88]. These results are not conclusive, though, as they either come from ocean-only and simplified atmosphere models [88] or from a coarse-resolution coupled General Circulation Model (GCM) [50], leaving open the questions on the role of ocean-atmosphere feedbacks and of the presence of ocean eddies. Concerning the ocean-atmosphere interaction, in Schmittner et al. [91] no abrupt collapse of the AMOC is observed in response to increasing CO₂ concentrations. These findings are not directly comparable with those using a direct (and stronger) freshwater forcing in the North Atlantic, but still raise the question whether the multiple equilibria regime of the AMOC is an artefact of simpler climate models, or of ocean-only models. A different perspective on this debate is given in Huisman et al. [54] using an ocean-only model and Drijfhout et al. [30] analysing the CMIP3 archive coupled climate models. In both works, the existence of a permanent shut-down state of the AMOC is connected with the salt/freshwater budget of the Atlantic Ocean. In particular, Drijfhout et al. [30] suggest that the lack of a collapsed state in IPCC-class climate models may be attributed to a bias in the salt transport by the AMOC, in connection with the salt-advection feedback at the Atlantic basin scale.

The value of the net equivalent freshwater import, or scaled salt export by the overturning circulation at the southern border of the Atlantic Ocean (usu-

ally taken to be 30°S), shorthand M_{ov} , is the key quantity that signals the coexistence of two stable equilibria of the AMOC. A short summary is provided below, with details in the Appendix A; for a complete discussion of the subject of the equivalent freshwater budget of Atlantic Ocean we refer to Drijfhout et al. [30]. The following definitions will be used: for a generic field f the barotropic operator is $\bar{f} = \int f dz / \int dz$, the baroclinic operator is $\tilde{f} = f - \bar{f}$, the zonal operator is $\langle f \rangle = \int_{60^\circ\text{W}}^{20^\circ\text{E}} f dx / \int dx$ and the azonal operator is $f' = f - \langle f \rangle$. Using the above notation, the equivalent freshwater import (i.e. the salt export) by the overturning circulation is defined as:

$$M_{ov} = -\frac{1}{S_0} \int_{30^\circ\text{S}} \tilde{v} (\langle S \rangle - S_0) dx dz, \quad (3.1)$$

where v is the meridional velocity (\tilde{v} is thus the baroclinic meridional velocity), S is the salinity and $S_0 = \overline{\langle S \rangle}_{30^\circ\text{S}}$. If M_{ov} is positive, the overturning circulation is exporting salt out of the Atlantic basin and only the present day ON state of the overturning is stable. In other terms, a *positive* M_{ov} corresponds to a *negative* salt-advection feedback at the basin scale, i.e. more salt is accumulated in the Atlantic Ocean if the AMOC transport decreases. If M_{ov} is negative, on the other hand, salt is imported into the basin by the overturning, and a second stable state of the AMOC exists, with reversed or no overturning in the Atlantic Ocean.

The equivalent freshwater import by the gyre is measured by the azonal part of the equivalent freshwater import, M_{az} :

$$M_{az} = -\frac{1}{S_0} \int_{30^\circ\text{S}} v' S' dx dz. \quad (3.2)$$

The complete equivalent freshwater budget for the Atlantic basin is given by

$$EPR = M_{ov} + M_{az} + M_d + M_{BS} - Q_t - V_t + Res, \quad (3.3)$$

where EPR is the basin net evaporation. M_d is the transport of equivalent freshwater by subgrid-scale processes (e.g., eddies) at the southern border and M_{BS} is the sum of total volume transport and total equivalent freshwater transport through Bering Strait. The quantities Q_t and V_t are the basin integrated equivalent freshwater content drift rate due to changes in total salt content and due to changes in volume and sea-ice, respectively. The last term, Res , is a residual term that closes the budget. It arises due to technical limitations in the determination of Q_t and V_t , unavoidable when computing these quantities from model output. The last five terms of Eq. 3.3 are generally much smaller than the others. Eq. 3.3 states that changes in the net evaporation of the Atlantic Ocean

must be mainly compensated by the equivalent freshwater (salt) transport by the baroclinic circulation at the southern border. In particular, if EPR remains constant, variations in the equivalent freshwater (salt) transport by the gyre will tend to be compensated by the equivalent freshwater (salt) transport of the overturning and vice versa.

While the role played by M_{ov} in determining the existence of multiple equilibria of the overturning circulation has been extensively studied in Huisman et al. [54] and de Vries and Weber [21], the importance of the zonal salinity contrast in the South Atlantic, determining M_{az} , has received little attention. Its relevance has been suggested in de Vries and Weber [21] where the compensation between M_{ov} and M_{az} has been exploited to control M_{ov} through a small change in the zonal salinity contrast in the subtropical South Atlantic. The recent work of Drijfhout et al. [30] has pointed again to the possible impact of the east–west salinity contrast in the South Atlantic for the stability of the AMOC. The present study is aimed at further understanding this particular issue: its main aim is to explore the relationship between M_{ov} and M_{az} in a systematic way, and to determine whether changes in the zonal salinity contrast in the South Atlantic can affect AMOC stability. The rationale of the experiments and the models used are described in section 3.2 and the main results in section 3.3. A discussion and conclusions follow in section 3.4.

3.2 MODEL EXPERIMENTS: METHODS

In this study, we use three different models: the Hybrid Coupled Model (HCM) SPEEDO, the Earth Model of Intermediate Complexity (EMIC) SPEEDO and the fully implicit model THCM (both described in subsections below). In the experiments with these models, the effect on the AMOC strength of two different freshwater anomaly patterns is investigated. One is a dipole freshwater flux (DIPO) pattern (with amplitude δ_p) applied over the southern part of the South Atlantic (Fig. 3.1). This freshwater anomaly is aimed at studying the effect of different zonal salinity contrasts in this area on the AMOC. The anomaly is expected to have a direct impact on M_{az} , but will also affect M_{ov} , in particular when EPR remains approximately constant, which is the case as long as the AMOC does not drastically change (collapses).

The second freshwater anomaly (EVAP) pattern (with amplitude γ_p) changes the net evaporation of the Atlantic basin and is compensated by an opposite anomaly over the tropical Pacific and Indian oceans (Fig. 3.1). This pattern changes the net evaporation and as a result is expected to change M_{ov} , with M_{az} remaining relatively unaffected. This anomaly pattern turns out to be an effective control parameter for the AMOC strength, as will be shown below. The precise region where this anomaly is applied does not change the sign of the

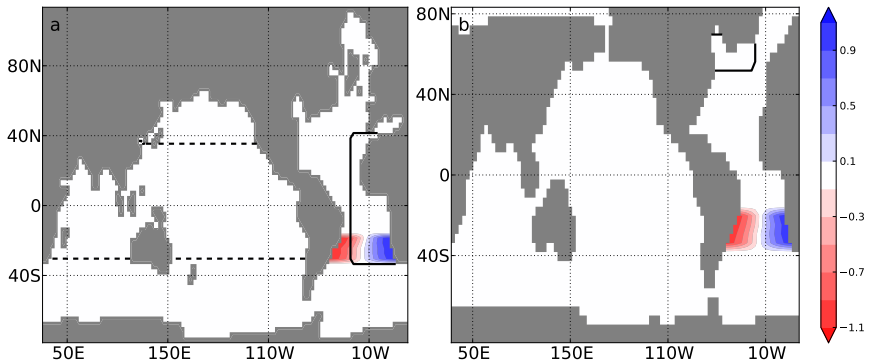


Figure 3.1: Areas where the freshwater flux anomalies DIPO and EVAP are implemented in SPEEDO (a) and THCM (b). The original model grids have been used (distorted in the North Atlantic and Mediterranean Arctic in the case of SPEEDO). The colour shading is the normalised intensity of the DIPO anomaly, the solid contour marks the area where EVAP is implemented, the dashed contour shows for SPEEDO the area used for the compensation of the Atlantic EPR reduction over the Pacific Ocean. For THCM, EVAP anomaly is compensated homogeneously over the rest of the ocean. Positive values correspond to an increased freshwater flux into the ocean.

sensitivity of the AMOC to γ_p , as demonstrated in [23], as long as it is applied inside the Atlantic basin. When the change in net evaporation is applied closer to the sinking regions of North Atlantic, it has a larger impact in magnitude (but with the same sign) than when the change is applied further south. Hence two different areas for applying γ_p were chosen in the two models used for this study.

3.2.1 *SPEEDO*

3.2.1.1 *SPEEDO EMIC*

In this work the EMIC SPEEDO [93] has been used to construct the HCM (see next subsection) and to validate the HCM results. The EMIC SPEEDO is an intermediate complexity coupled atmosphere/land/ocean/sea-ice general circulation model with fully resolved ocean and atmosphere dynamics, but simplified physics in its atmospheric component. The ocean component (CLIO) has a horizontal resolution of approximately 3° and 20 unevenly spaced vertical levels. Convective adjustment is used to avoid static instability in the water column. The LIM sea-ice model [45] is included. The atmospheric component of the EMIC is an atmospheric GCM, having a horizontal spectral resolution of T30 and

8 vertical density levels. Simple (linearised) parameterisation are included for large-scale condensation, convection, radiation, clouds and vertical diffusion.

3.2.1.2 *SPEEDO HCM*

The HCM SPEEDO [16, 43] includes the same ocean and sea-ice model as the EMIC, forced at the surface by a statistical atmospheric model that, in this case, consists of linear regressions of atmospheric fluxes to the Sea Surface Temperature (SST). The HCM has been constructed from data of the EMIC SPEEDO. This model is used for most of the experiments. A complete description of the definition and test of the HCM can be found in Cimadoribus et al. [16].

It is forced by a daily climatology for heat, freshwater and momentum fluxes and additionally includes a basic representation of the ocean–atmosphere interaction. At each time step linear perturbation terms are calculated, derived from the fully coupled model data and depending on SST. They are introduced to mimic the effect of atmospheric feedbacks on both local and large scale. The local perturbations are a minimal representation of ocean–atmosphere interactions in a statistical steady state. The large scale term represents the response of the surface fluxes to changes in meridional overturning circulation strength. These perturbation terms reproduce the changes in the surface fluxes connected with e.g. changes in convection, wind intensity and direction, runoff etc. [16]. This model design benefits from the fact that the atmosphere, on sufficiently long time scales, can effectively be treated as a “fast” component that adjusts to the ocean anomalies. The use of a minimal atmosphere renders integrations of tens of thousand years feasible with modest computational requirements.

The equilibrium solution of SPEEDO, both for the EMIC and the HCM, consists of an Atlantic basin integrated net evaporation overestimated both with respect to most other models and to the few available observations (0.6 Sv in the model as compared to the recent estimate of 0.28 ± 0.04 Sv by Talley [105]). Furthermore, the zonal gradient of salinity in the South Atlantic is reversed, with a maximum on the eastern side. These problems are inherited in the HCM, that features very similar biases.

3.2.1.3 *Experimental details*

The high evaporation over the basin, combined with the low salt export by the gyre due to the reversed zonal salinity profile, force the overturning circulation to export salt ($M_{ov} = 0.29$ Sv) to close the budget. As proposed in [21] and [54], this situation is connected with the presence of a single equilibrium of the thermohaline circulation, as salt export by the overturning circulation is associated with a negative salt-advection feedback at the basin scale. In

de Vries and Weber [21] and Cimatoribus et al. [16], small freshwater corrections were successfully used to change the sign of the salt-advection feedback. The anomaly patterns in the two references above are defined in a similar way, even though the sign is opposite there; here anomalies have the same sign as in Cimatoribus et al. [16].

The regions for the flux anomaly patterns are i) the South Atlantic between 30°S and 20°S for the DIPO pattern, which is centred at the zonal midpoint of the basin, and is positive to the east (that is, increased freshwater flux into the ocean in the east) and (ii) the part of the basin east of 20°W , south of Gibraltar Strait and north of the southern tip of Africa for the EVAP pattern (see Fig. 3.1a). The choice of area (ii) is based on the fact that this is the part of the basin where salinity is overestimated the most. It may be argued that this choice of EVAP has a dipole component too, and may thus project on DIPO. It will be shown that this does not affect the results substantially; they are comparable with results obtained using an EVAP pattern with no dipole component at all. The freshwater anomalies are always implemented as a virtual salt flux at the surface, in order not to influence the heat budget of the basin. In SPEEDO the anomalies will always have the same sign, implying that the control run of SPEEDO is taken as the extreme case of highest net evaporation and strongest zonal salinity contrast bias. Through the freshwater anomalies these model biases are compensated and even reversed. This guarantees that an area of the parameter space is explored that includes the present day state of the ocean.

Table 3.1 summarises the experiments performed with this model, listing the starting and ending values of the integrated freshwater flux due to each of the two anomaly patterns. The experiments are conducted with the following procedure. First, in the spin-up phase, the model is brought to a statistical steady state, keeping the freshwater anomalies constant at the initial value listed in Table 3.1. For instance, in experiments A, B or HCMc both anomalies in the initial state are set to zero. For C or D, instead, one of the two is kept at a nonzero constant value in the spin-up phase. The spin-up time, needed to obtain an ocean in statistical equilibrium, is in the order of thousand years. For the reversed experiments Crev and Drev, the initial state is the end state of C and D respectively. During the main run, the flux anomalies are changed linearly in time, towards the final value. All runs last 12,000 years, except for HCMc and GCMc, lasting 4,000 years. These last two runs are meant for checking the consistency of the results from the SPEEDO HCM and the fully coupled model. The shorter length of the integration is due to the much higher computational requirements for the fully coupled EMIC.

Name	Model	γ_p [Sv]	δ_p [Sv]
A	HCM	0.0 – 0.4	0.0 – 0.0
B	HCM	0.0 – 0.0	0.0 – 0.5
C	HCM	0.0 – 0.4	0.5 – 0.5
Crev	HCM	0.4 – 0.0	0.5 – 0.5
D	HCM	0.4 – 0.4	0.0 – 0.5
Drev	HCM	0.4 – 0.4	0.5 – 0.0
HCMc	HCM	0.0 – 0.4	0.0 – 0.5
GCMc	EMIC	0.0 – 0.4	0.0 – 0.5

Table 3.1: List of the simulations with the abbreviations used in the text. The initial and final values of the two freshwater anomaly amplitude are listed. The anomalies change linearly in time during the experiment. All experiments last 12,000 years with the exception of HCMc and GCMc lasting 4,000 years.

EPR	$6.1 \cdot 10^{-1} \text{ Sv}$	M_{ov}	$3.2 \cdot 10^{-1} \text{ Sv}$
M_{az}	$1.5 \cdot 10^{-1} \text{ Sv}$	M_d	$3.0 \cdot 10^{-2} \text{ Sv}$
M_{BS}	$6.1 \cdot 10^{-2} \text{ Sv}$	Q_t	$-4.0 \cdot 10^{-5} \text{ Sv}$
V_t	$-1.3 \cdot 10^{-3} \text{ Sv}$	Res	$4.7 \cdot 10^{-2} \text{ Sv}$

Table 3.2: Values of the different terms in Eq. 3.3 as computed in the control run of the EMIC SPEEDO. The budget is computed from yearly data, using a 1,000 years long simulation at statistical steady state.

The rate of change of the freshwater anomalies, approximately 0.04 Sv per thousand years for the long runs, is far from the values needed to correctly approximate the bifurcation diagram of the AMOC (less than 0.001 Sv per thousand years), in particular close to a bifurcation point [87, 108]. The focus is here not on the determination of the exact position of the bifurcation points, but rather on the qualitative aspects of the presence/absence of an abrupt collapse of the AMOC for different patterns and amplitudes of the freshwater anomalies applied. Despite this deficiency of the experimental setup, it will be shown that the results are consistent with a model (THCM) explicitly solving the steady state problem for the large scale circulation in the ocean.

3.2.2 THCM

3.2.2.1 Model details

The ThermoHaline Circulation Model (THCM, [119]) is a fully-implicit ocean-only model that is designed to perform numerical bifurcation analysis of the large-scale circulation. The model is based on the rigid-lid primitive equations and includes a realistic global model geometry. The horizontal resolution is about 4° , and there are 12 levels, ranging in thickness from 50 m for the top layer to 950 m for the bottom layer. The configuration used is the same as in [54], to which we refer for further details. The model has several deficiencies [28] that make it less well suited for quantitative analyses. Rather, it allows for an efficient way of exploring qualitatively the properties of the large-scale global circulation.

In THCM, heat fluxes are determined by a simple two-dimensional energy balance model that is coupled to the upper ocean layer [119]. Sea-ice is not included in the model. For the wind stress, the annual mean field provided by [109] is used. The reference (unperturbed) freshwater flux is diagnosed from the sea surface salinity restoring to the Levitus [68] climatology. The zonal salinity contrast in the South Atlantic is hence approximately correct, with basin-integrated net evaporation amounting to 0.3 Sv. In the reference case ($\delta_p = \gamma_p = 0$), the surface loss of freshwater is compensated by freshwater transport by both the AMOC ($M_{ov} = 0.10$ Sv) and the azonal transport ($M_{az} = 0.05$ Sv); the remainder due to diffusion and transport across the northern border of the Atlantic. Azonal transport is weak compared to SPEEDO due to the weak barotropic circulation, so that diffusive transport plays a primary role in closing the equivalent freshwater budget.

3.2.2.2 Experiment details

With the aim of building a framework for understanding the SPEEDO HCM results, the sensitivity of THCM to changes in δ_p and γ_p is explored. As in [28, 54, 119], but different from what is done in the HCM experiments, the net evaporation change is achieved by applying an anomalous flux of strength γ_p south of Greenland (see Fig. 3.1b), compensating this flux everywhere else. The pattern of the dipole anomaly is similar to the one used in the HCM SPEEDO experiments (Fig. 3.1a). γ_p is used as the primary bifurcation parameter and parameter space is explored by constructing bifurcation diagrams for a number of discrete values of δ_p . From the bifurcation diagrams, a regime diagram can be constructed, delineating the regions of existence of the present-day and collapsed states of the overturning circulation.

3.3 MODEL EXPERIMENTS: RESULTS

First, the results from the SPEEDO HCM are discussed, analysing in particular the relationship between the freshwater anomalies and the AMOC strength, and the equivalent freshwater transport by the overturning and azonal components of the circulation. Results from the SPEEDO HCM and the EMIC are reported in figures 3.2 to 3.6. Thereafter, the results will be interpreted in the framework of dynamical systems, using the regime diagram obtained from THCM (Fig. 3.7).

3.3.1 SPEEDO HCM

The freshwater anomalies induce a strong overshooting of the AMOC (Figs. 3.2 and 3.5, black lines). Changes in the boundary conditions can trigger convection at new sites, that will then give a substantial contribution to the overturning strength in our low resolution configuration. In these experiments, the freshwater anomalies are applied far from the convection sites, so the initial response in the North Atlantic can actually be that of a slight increase in surface density, that in turn triggers convective adjustment at new grid cells with a consequent AMOC overshooting. Even if the magnitude of the increase in overturning strength is overestimated, there is no reason to believe that the sign of the response is wrong. Moreover, the overshootings have an intermittent character and the overall trend in AMOC strength is not affected by them.

3.3.1.1 Decreasing *EVAP*, no *DIPO* anomaly

The first experiment, A, includes no dipole anomaly, but solely a decrease of net evaporation over the Atlantic basin. The ocean state of this experiment can be considered as an extreme case of an ocean model with a zonal salinity bias. The final value of the evaporation anomaly is 0.4 Sv, giving a substantial decrease in *EPR* (Fig. 3.2A, red line). The response of the AMOC, after an initial overshooting, is that of a strong decrease in strength (maximum is halved at the end of the run). No abrupt collapse is observed, and the decrease slightly deviates from linear behaviour only after year 10,000 of the simulation. M_{ov} (Fig. 3.2A, blue line) is positive in the initial phase, and approaches zero only at the end of the experiment. The change in *EPR* impacts only M_{ov} , leaving the other terms in the equivalent freshwater budget unchanged (the terms of Eq. 3.3 not plotted in Fig. 3.2 are, to a very good approximation, constant in all experiments (see Appendix A)). No compensation is seen between M_{ov} and M_{az} , and the change in *EPR* is thus almost completely balanced by a change in M_{ov} . The change in M_{ov} can be explained by the decrease in overturning strength (M_{ov} scales linearly with the overturning strength) and by the changes

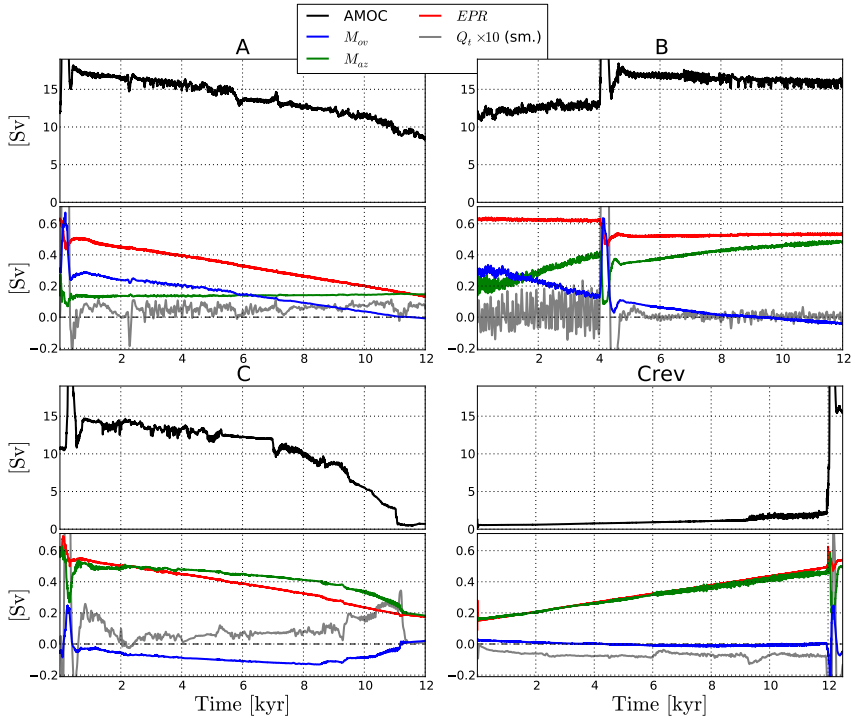


Figure 3.2: AMOC and equivalent freshwater budget at the southern border of Atlantic Ocean for experiments A, B, C, Crev. For each experiment, two panels are shown: in the upper one the evolution of the maximum of the AMOC streamfunction below 550m is shown, in the lower panel the evolution of some of the terms of the equivalent freshwater budget (equation 3.3) are reported. Q_t (grey line) is magnified 10 times and smoothed for plotting purposes, through a convolution with a Hanning window 71 years wide. This is done to remove fast fluctuations that would otherwise render the plot unreadable.

in the zonally averaged salinity profile at 30°S (see Fig. 3.3A). The latter figure shows that the *EPR* anomaly affects the deeper branch of the AMOC (freshening) as well as the upper one (becoming saltier). The net effect is an increased salt transport into the Atlantic basin by the overturning circulation, consistently with M_{ov} in Fig. 3.2A. The grey line of Fig. 3.2A shows the rate of change of the equivalent freshwater content in the Atlantic basin (Q_t in Eq. 3.3, multiplied by a factor 10). M_{ov} does not compensate exactly for the change in *EPR*, as Q_t is greater than zero.

The basin is thus freshening, suggesting that this is the main cause for the decrease in AMOC strength. As the strength of the AMOC is determined by the amount of sinking in the high latitudes of the North Atlantic, the equivalent freshwater transport in the basin is also diagnosed at 30°N (Fig. 3.4)¹. The AMOC strength seems to be controlled by the overturning component of the salt transport at this latitude (shorthand M_{ov}^{30N} , as it is defined in the same way as M_{ov} at the southern border of the basin). This quantity is negative, since at this latitude the salt transport is always northward. The *EPR* reduction makes M_{ov}^{30N} less negative. Even if this change is almost fully compensated by the azonal part of the transport at 30°N, the decreased salt transport to higher latitudes brings an effective freshwater perturbation in the sinking regions, as shown by the positive value of Q_t^{30N} (multiplied by a factor 5, grey line in Fig. 3.4A), i.e. the drift in equivalent freshwater content north of 30°N in the Atlantic and Arctic. *EPR* north of 30°N (EPR^{30N} , red line in Fig. 3.4A) remains on the other hand almost constant. The deviation from the linear decrease of the AMOC appears after the azonal transport at 30°N (M_{az}^{30N}) becomes negative. This evidence, confirmed by the other experiments, suggests that a qualitative change in the AMOC response takes place when the overturning circulation is not able to import enough salt from the tropics into the subpolar region to compensate for precipitation change over the area.

3.3.1.2 Increasing *DIPO*, no *EVAP* anomaly

In experiment B, *EPR* is unchanged, while the dipole anomaly increases from 0 to 0.5 Sv during the run. In response to this, the AMOC slightly increases until year 4,000. After a sharp rise between years 4,000 and 4,600, the AMOC starts to decrease until the end of the simulation. M_{ov} and M_{az} at the southern border change with opposite sign in this case, and approximately compensate each other (Fig. 3.2B). This is connected with the fact that, in the budget of Eq. 3.3, all terms remain approximately constant, with the exception of M_{az} ,

¹ As the model grid is distorted in North Atlantic and Arctic Oceans, the latitude of this transect is only approximate. The model grid is needed in order to avoid interpolation errors.

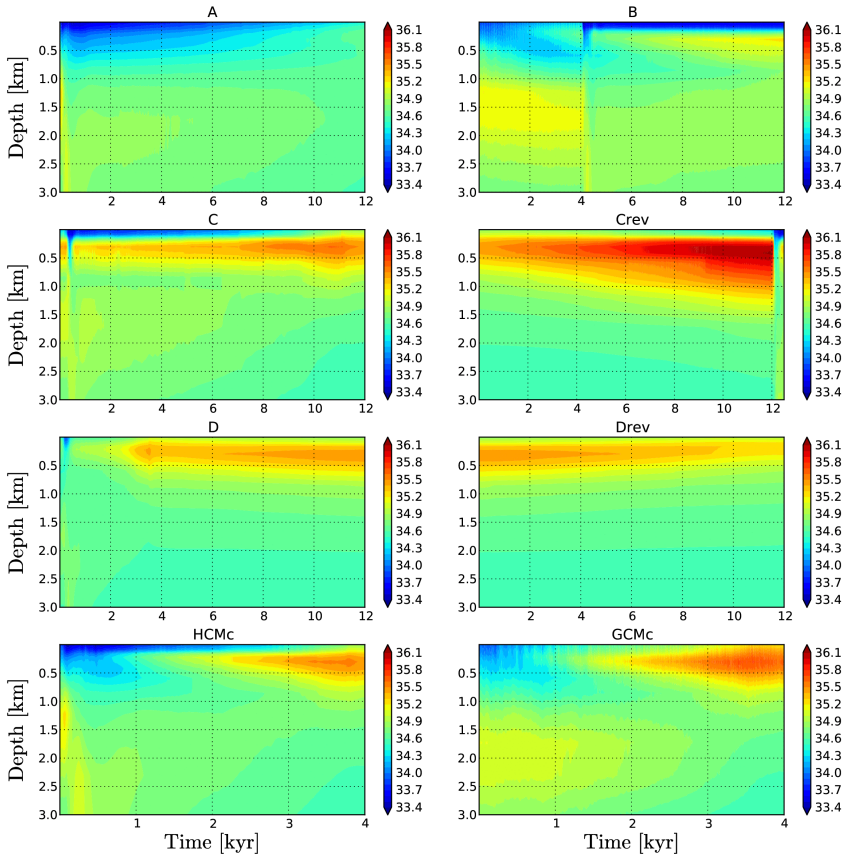


Figure 3.3: Temporal evolution of the zonal average of salinity between 60°W and 20°E at the southern border of the Atlantic Ocean as a function of time and depth.

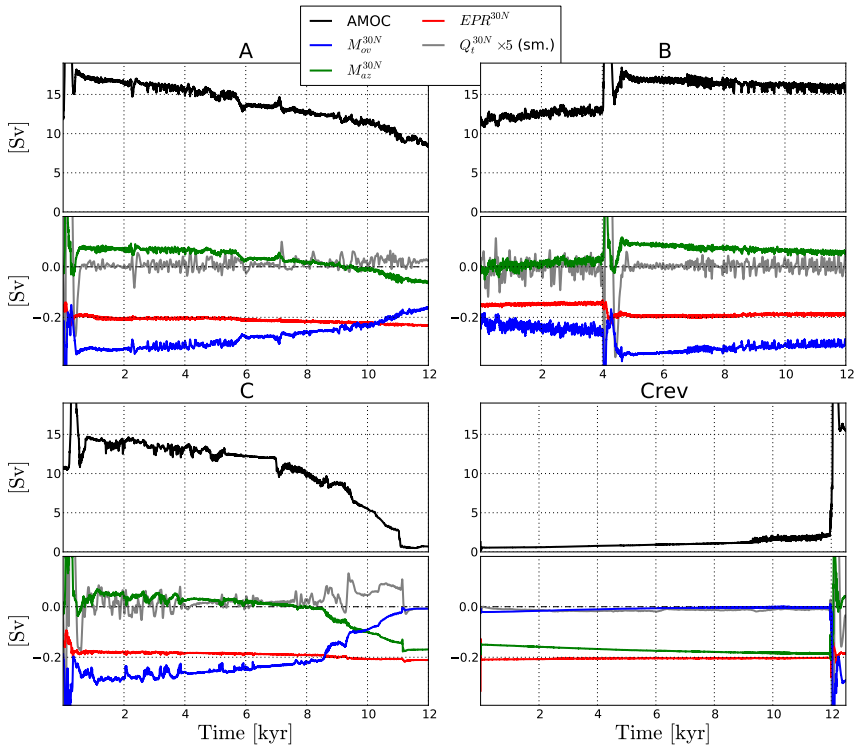


Figure 3.4: Same as figure 3.2, but considering a section at approximately 30°N , and the portion of the Atlantic and Arctic basin northwards.

controlled by the dipole anomaly, and M_{ov} , opposing the azonal term, while EPR remains almost constant. By means of this compensation mechanism, the sign of M_{ov} changes during the experiment. The total salinity content of the basin is not significantly affected by the changes in the dipole anomaly ($Q_t \approx 0$ in the time mean, see figure 3.2B). This is the principle exploited in the experiments of de Vries and Weber [21] and Cimadoribus et al. [16], where a dipole anomaly was applied to change the sign of M_{ov} . Because of the compensation between M_{ov} and M_{az} , the dipole anomaly has to induce changes in zonally averaged salinity as well on the longer time scale. Figure 3.3B shows that the main effect of the dipole anomaly on the zonally averaged salinity is to increase the salinity in the upper branch of the AMOC (between approximately 250 and 1000m). Virtually no changes are observed in the lower branch (approximately between 1000 and 2500m) before and after the overshoot, but during the overshoot a significant freshening takes place, reflecting changes in deep convection. The dipole anomaly is changing M_{ov} modifying the intermediate waters, whose salinity increases in response to the increased salinity export by the azonal part of the circulation (salinity increases not only in south-western Atlantic, but also more to the south). During the whole run the dipole anomaly shifts the salt transport between different terms of the transport, but the overall salt content of the Atlantic Ocean is not changed, nor is EPR (again, excluding the discrete jump during the overshooting). Also in this case, changes in AMOC strength are controlled by the equivalent freshwater transport by the overturning at 30°N (AMOC increases when $M_{ov}^{30^\circ\text{N}}$ decreases, and vice versa, see Fig. 3.4B).

3.3.1.3 Changing EPR , constant DIPO anomaly

In experiment C, the same EPR reduction as in A (0.4 Sv) was applied to an ocean state that already includes a dipole anomaly of 0.5 Sv. The zonal salinity contrast in the South Atlantic is reversed compared to experiment A (salinity maximum in the west of the basin instead of the east). The response of the AMOC is now totally different. The initial strength (discarding the initial overshooting) is just 2 Sv lower than in experiment A, but in experiment C the EPR reduction causes the AMOC to completely collapse at year 11,000. The initial (linear) response of the AMOC in C is not stronger than in A, but the linear behaviour breaks down near approximately year 8,000, with a faster linear decrease at first, and then a final complete collapse. Thus, the AMOC may collapse by freshwater anomalies applied far from the sinking regions. This is a clear evidence of the fact that the sign of the sensitivity of the AMOC to freshwater anomalies, on longer time scales, is not dependent on the area where the anomaly is applied [23, 50]. Also the behaviour of M_{ov} and M_{az} is totally different from that in experiment A. In the initial state, M_{ov} is slightly negative,

and tends to decrease as long as the linear response of the AMOC is maintained. Both the zonal and azonal components of the transport are affected by the reduction in EPR , and both contribute to closing the equivalent freshwater budget of the basin. As in A, the net EPR change affects both the upper and the lower branches of the AMOC, but the zonally averaged salinity profile is very different in C (compare Fig. 3.3 panels A and C). The constant dipole anomaly applied in C induces a reduction in contrast between the upper and lower branches of the AMOC. As in A, M_{ov} decreases when EPR decreases, but the lower salinity contrast reduces the ability of the AMOC to import more salt into the basin as EPR decreases. The budget must be closed by a decrease in M_{az} as well. The changes in the equivalent freshwater transport do not fully compensate the reduction in EPR , and the basin is freshening more than in experiment A. This can be seen by comparing the grey lines in figure 3.2A and C, showing that Q_t is more positive in the latter experiment. In correspondence with the break of the linear response of the AMOC, the relationship between M_{ov} and M_{az} is suddenly modified, and their changes start to be of opposite sign (M_{az} keeps decreasing, but M_{ov} starts to increase). This increase (M_{ov} becomes less negative) is due to the quickly weakening AMOC. The decreased salt import by the AMOC brings an effective freshwater anomaly in the basin. This is the manifestation of the basin scale salt-advection feedback. The decreasing intensity of the AMOC amplifies the initial perturbation through M_{ov} which leads to the collapse. Considering the section at 30°N (Fig. 3.4C), the situation is very similar to experiment A, but the subpolar Atlantic is freshening much more in this case (grey line). As for experiment A, the initial linear response of the AMOC is broken down when M_{az}^{30N} becomes negative.

The reversed experiment, Crev, starts from the end of experiment C and consists of a reduction of the EPR anomaly from 0.4 Sv back to zero (i.e. an increasing EPR) over the Atlantic Ocean. The changes in the net evaporation of the basin are compensated only by M_{az} (Fig. 3.2Crev), as the (reverse) overturning is weak and shallow. This compensation is incomplete, and the salinification of the basin (grey line in Fig. 3.2Crev) leads to a recovery at the end of the run (a few hundred years after year 12,000). The area where the two equilibria exist seems to extend over almost the whole parameter range covered by experiments C and Crev. It must be kept in mind, however, that the boundaries of the multiple equilibria region are likely to be overestimated in these transient hysteresis experiments. The fact that the anomalies change too fast for an equilibrium to be maintained will tend to delay the transitions between the two states, due to the inertia of the system (see e.g. [61]). Furthermore, the low noise level in the HCM provides an unrealistically weak source of perturbations to the circulation, that reduces the chances of transitions to occur before the bifurcation points are reached [77]. The initially slow recovery is already accompanied by a strong increase of salinity in the upper Atlantic (Fig. 3.3Crev),

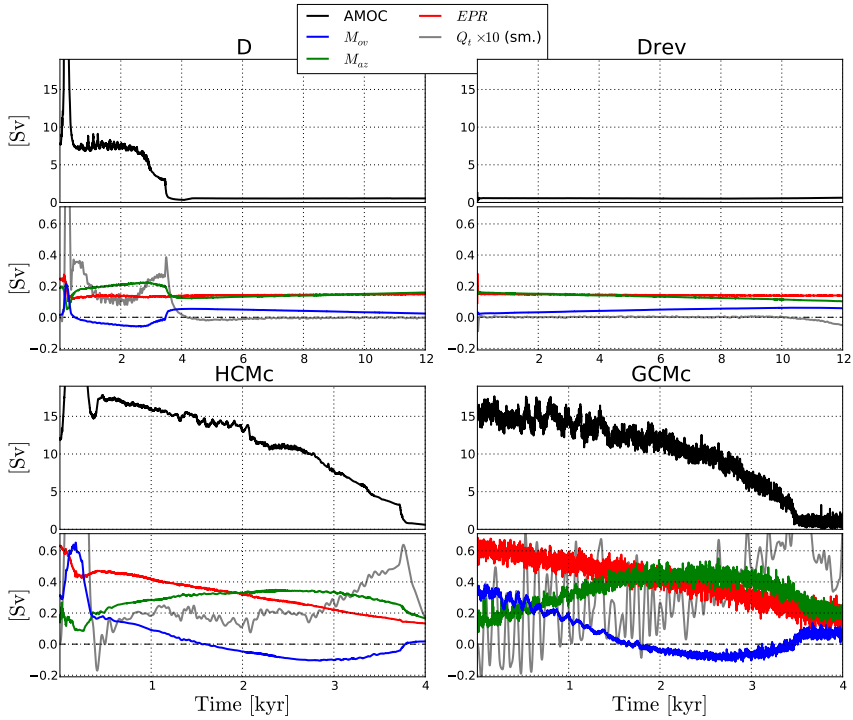


Figure 3.5: Same as Fig. 3.2 for experiments D, Drev, HCMc and GCMc.

which provides a positive density perturbation eventually triggering the AMOC onset.

3.3.1.4 Changing DIPO, constant EVAP anomaly

In the last full length experiment, D, the increase in the dipole freshwater anomaly is applied over an Atlantic Ocean with reduced net evaporation. The initial state features an AMOC that, although stable, is markedly weaker than in the previous cases. Figure 3.6D shows that M_{az}^{30N} is already negative at the beginning of the run, a situation that is connected with an increased sensitivity of the AMOC to *EPR* perturbations. During the experiment, the AMOC shows little sensitivity to the changes in the dipole anomaly before approximately year 3,000. After this point, the circulation quickly collapses. This experiment shows that the dipole anomaly, that does not affect the integrated net evaporation of the Atlantic basin, is sufficient to collapse the AMOC provided that the basin is not too strongly evaporative. Also in this case a compensation between M_{ov}

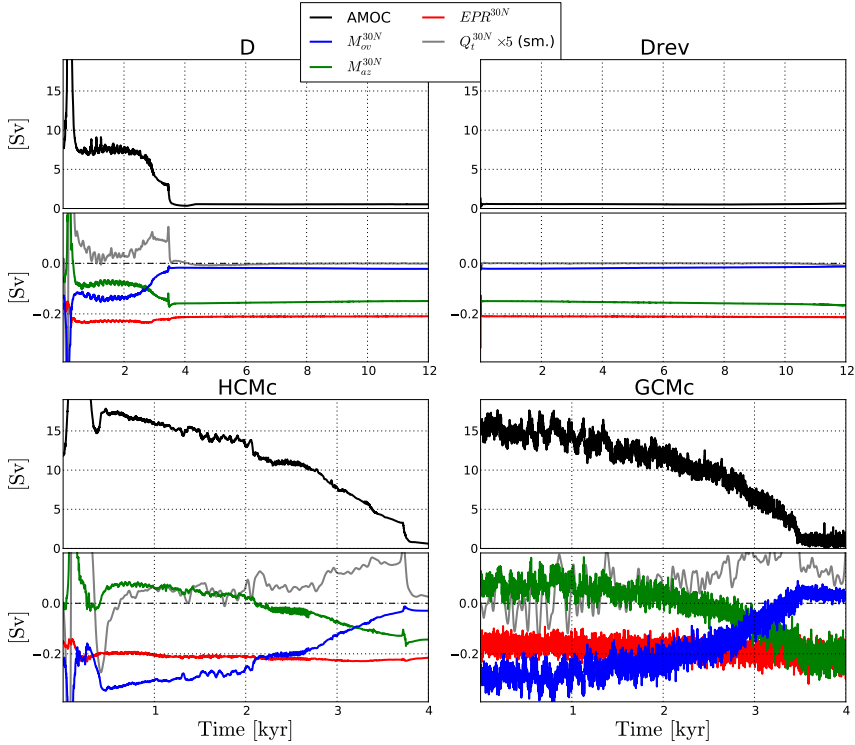


Figure 3.6: Same as figure 3.4 for experiments D, Drev, HCMc and GCMc.

and M_{az} at the southern border is observed, up to the point where the collapse is triggered (Fig. 3.5D). In this case, M_{ov} is negative, and a strong freshening of the basin is observed before the collapse, showing that the overturning circulation is not able to completely compensate the increasing salt export by the azonal component. After the collapse is triggered, the basin scale salt-advection feedback is playing a major role in increasing Q_t , through the increase in M_{ov} becoming less negative as the AMOC weakens. The reversed circulation that establishes after the collapse has a slightly positive M_{ov} , that guarantees the closure of the budget, bringing Q_t to zero.

To check whether this collapse is permanent, the experiment is repeated, decreasing again to 0 the value of the dipole anomaly (Drev). The AMOC shows no sign of recovery, despite the fact that M_{az} and M_{ov} are (slowly) responding to the increasing freshwater anomaly. At the end of the run Q_t deviates markedly from zero towards negative values. The salinification of the basin is likely a

prelude to a recovery for negative values of the dipole anomaly, but the run was not extended into that unrealistic parameter regime.

It is concluded from these experiments that the zonal salinity contrast plays a fundamental role in determining the sensitivity of the AMOC, and a zonal bias in the salinity distribution in the South Atlantic can completely change the sensitivity of the AMOC to perturbations in the basin integrated surface freshwater forcing (experiments A and C). In particular, the zonal salinity contrast strongly affects the equivalent freshwater transport by the azonal and overturning circulation, and can determine as a consequence the stability of the AMOC. The dipole freshwater anomaly that corrects such a bias does not have a large impact on the AMOC strength, but can cause a collapse in a basin with low *EPR*.

3.3.1.5 *EMIC–HCM comparison*

Last, a comparison between the HCM and the full EMIC is performed, with two runs named HCMc and GCMc respectively. Both models start from the initial state of experiment A, and the two freshwater anomalies are then both increased during 4,000 years. The response in the two models is very similar (Fig. 2-4), supporting the choice for the HCM in the other runs. The main differences are the lower variability in HCMc and the earlier collapse in GCMc. The weak variability of the HCM model originates from the model definition itself, which does not include any noise term able to mimic atmospheric variability on short time scales. This issue has already been discussed in Cimattoribus et al. [16], and is not affecting the very long time scales considered in this work. The collapse for lower values of the anomalies in GCMc can be explained by GCMc having higher noise levels that provides stronger perturbations to the AMOC (higher chances of switching between two equilibria). The sensitivity of the overturning strength to the freshwater anomalies, as well as that of the salt transports, is indeed very similar in the two experiments.

3.3.2 *THCM*

The results of the previous section will be further interpreted with a bifurcation analysis obtained with THCM. Due to the substantial differences between the models, the comparison will be mainly qualitative, enabling to interpret the findings reported above in the framework of bifurcation theory. The results from THCM are summarised in Fig. 3.7, showing first the maximum of the AMOC streamfunction as a function of the two control parameters γ_p and δ_p , i.e. the integrated intensity of the freshwater anomalies (Fig. 3.7a). The paths of the saddle-node bifurcations (the points where the abrupt transition between the two states takes place) are plotted as the dotted curves in Fig. 3.7a, shown on the bifurcation diagrams as circles and, in more detail, in the regime

diagram in Fig. 3.7b. When δ_p is changed, two modifications of the bifurcation diagram occur: (i) the saddle-node bifurcations both shift in the same direction along the γ_p axis (rigidly shifting the whole multiple equilibria (ME) regime region) or (ii) the two saddle-node bifurcations shift in opposite directions (affecting the width of the ME regime in the γ_p direction). The path of the one on the ON branch (L_1) is plotted in red and the one on the OFF state (L_2) in green. From this regime diagram, the shift of the ME regime and the changes in hysteresis can be distinguished.

The estimate of the initial control state of SPEEDO, marked with CS in Fig. 3.7b, is based on the surface salinity biases diagnosed in the model, and on the qualitative comparison of the behaviour of the HCM with respect to THCM. The trajectories in the phase space of the different experiments performed with the SPEEDO HCM are drawn as white arrows. These trajectories are, by necessity, only rough estimates since γ_p scales differently in the two models, being applied in different regions. The area where two steady states are possible under the same boundary conditions (ME) is marked in blue in the figure. This region is bounded by the two saddle node bifurcation lines, that in turn merge in two cusps at sufficiently large values of the dipole anomaly ($\mathcal{O}(1\text{ Sv})$ for the model used here). In the vicinity of the two cusps, the computational time needed for finding steady state solutions diverges, and the results are thus missing there; their actual position can only be guessed. The AMOC is substantially weakened outside the region bounded by the cusps, for any value of EPR (Fig. 3.7a).

The diagram is not symmetric with respect to the $\delta_p = 0$ line: for positive values of the DIPO anomaly ($\delta_p > 0$, i.e., freshwater added in the east) the two saddle nodes slowly approach each other moving towards the cusp, but quickly shift towards the $\gamma_p = 0$ line (in particular the first saddle node, red line in Fig. 3.7). For negative values of the DIPO anomaly ($\delta_p < 0$), the bifurcation points approach each other much faster, with an evident shift of the second saddle node towards positive γ_p . Outside the multiple equilibria regime, only one steady state is available. Two distinct ON and OFF states are well defined in the ME interval between the two cusps, as in this area an unstable solution is dividing the two states (see e.g. [54]). Changes in the net freshwater anomaly, here, force the system to jump from one solution to the other when a saddle node is reached. The transition in the two opposite directions takes place at different values of γ_p , i.e. the response of the circulation shows hysteresis. Outside this area, a continuous change between the two states, as a function of the net evaporation change, is observed. In this region of the diagram, no hysteresis behaviour is possible. It must be noted that in a more realistic framework, where variability in the ocean and the atmosphere would provide a source of stochastic perturbations, the area where hysteresis can be

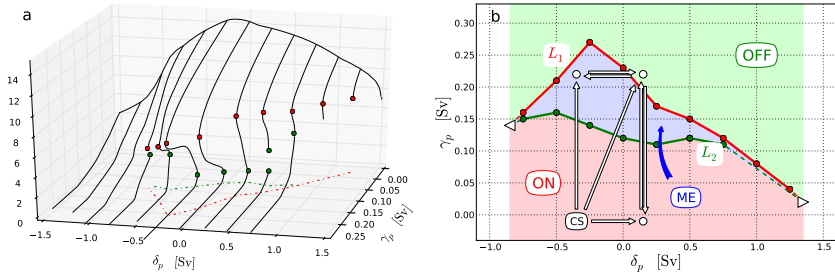


Figure 3.7: a. Collective three-dimensional plot of bifurcation diagrams from THCM experiments. The maximum AMOC streamfunction is shown as a function of the two control parameters δ_p (strength of the DIPO anomaly) and γ_p (strength of EVAP anomaly). Some solution branches are incomplete due to computational problems (see text). In both panels, the red dots mark the saddle node at the end of the ON solution branch (L_1); the green dots refer to the saddle node marking the end of the OFF solution branch (L_2). The projection of the position of the saddle-node bifurcations on the (δ_p, γ_p) plane is also shown (enlarged in panel b).

b. Regime diagram for the AMOC streamfunction in THCM. The dots mark the positions of the saddle nodes and the lines are guides for the eye. The two triangles mark the purely hypothetical positions of the two cusps, where the two saddle nodes merge. The red (green) shaded area is the region where only the ON (OFF) solution exists, the blue area marks the multiple equilibria regime (ME). Outside the area horizontally bounded by the cusps, the two solutions are not separated by an unsteady state, and no abrupt transition is possible changing γ_p . Superimposed to the regime diagram, in white, are the approximate trajectories of the experiments performed with the SPEEDO HCM. The end and initial states of SPEEDO HCM experiments are marked by white dots. The control state of the SPEEDO HCM (marked "CS") is shifted with respect to that of THCM (see text), and all the anomalies applied to it are shifted as a consequence. γ_p has different scales for the two models (see text).

detected would shrink, as stochastic perturbations would render the positions of the two saddle nodes practically indistinguishable if close enough [77].

With a larger positive dipole anomaly, a smaller γ_p is needed to reach the multiple equilibria regime, and eventually to collapse the AMOC. This is confirmed by the results from the SPEEDO HCM, experiments A and C (represented by the vertical white arrows in Fig. 3.7b). When the dipole anomaly is applied (experiment C), the same net evaporation reduction used in A is sufficient to completely collapse the AMOC, crossing the first saddle node L_1 . In experiment C, the value of M_{ov} is also much lower than in A and it is negative, suggesting that the AMOC in the HCM, with the dipole anomaly applied, is in the multiple equilibria regime, as confirmed by the reversed experiment Crev.

The strength of the AMOC for $\gamma_p = 0$ only weakly depends on δ_p , with a maximum close to $\delta_p = -0.25$ Sv (Fig. 3.7a), but the basin integrated net evaporation is the main control parameter of the AMOC strength. A similar, weak dependence of the AMOC strength on δ_p was found in SPEEDO (experiment B). Finally, experiment D (upper horizontal arrow) shows how the δ_p interval for which an ON state of the overturning circulation is available quickly shrinks for decreasing *EPR* values (increasing γ_p), up to the point where a small dipole anomaly at the southern border of the Atlantic (approximately 0.125 Sv in experiment D) is sufficient for causing a complete collapse of the AMOC.

3.4 DISCUSSION AND CONCLUSIONS

In this work, the central importance of the Atlantic equivalent freshwater budget in determining the stability of the AMOC has been demonstrated. In particular, it was shown that a correct representation of the zonal salinity contrast at the southern border of the Atlantic is fundamental in determining the stability properties of the overturning circulation and the existence of the ME regime. The strength of a freshwater anomaly necessary to collapse the overturning is highly sensitive to biases in the salinity import by the azonal circulation at the southern boundary, in turn mainly determined by the zonal salinity difference. It was also shown that a dipole freshwater anomaly summing up to zero, applied over Southern Atlantic, is sufficient to collapse the overturning circulation if the basin net evaporation is sufficiently low. These results demonstrate that the azonal transport, connected to the three dimensional wind-driven gyre, plays a major role in controlling the AMOC stability, through the compensation mechanism between salt transport by the overturning and the gyre, whenever the net evaporation over the Atlantic basin remains approximately constant. This interplay of the meridional and horizontal circulation challenges the two dimensional view of the AMOC, and once again suggests that the results from Stommel-type models (e.g. [47, 57, 84, 86, 92, 99]) should be evaluated with

great care. In particular, the idea of the AMOC stability determined only by salinity in the sinking regions of North Atlantic seems to be an oversimplification of the real system. In summary, the salinity in the subpolar North Atlantic is one of the main controls of the strength of the AMOC, but the existence of a stable collapsed state of the AMOC is controlled by the equivalent freshwater budget of the entire basin.

Based on the results of these experiments, we can identify different regions in the parameter space, with markedly different sensitivity of AMOC to external perturbations. These regions could serve as a guide for assessing the AMOC sensitivity in different climate models. Starting point is the estimation of the equivalent freshwater budget for the Atlantic Ocean and in particular the coupling between the M_{ov} and M_{az} in the freshwater budget. As sketched in figure 3.8, a positive value of δ_p induces a fresher eastern part of the South Atlantic which causes an increase in the azonal freshwater transport M_{az} . Keeping other terms constant, an increase in M_{az} is compensated by a decrease in M_{ov} leading to more freshwater export out of the Atlantic by the AMOC due to changes in the zonally averaged salinity profile.

The freshwater budget gives direct hints to the stability properties of the overturning circulation in the model [54] and provides an estimate of the position of the model in the regime diagram of Fig. 3.7. A dipole anomaly can move the system closer to the regime of multiple equilibria, as the second bifurcation point L_2 (green line in Fig. 3.7) moves towards smaller values of γ_p for increasing values of the dipole anomaly. This is, incidentally, a clear indication of the fact that a model with a correct zonal salinity contrast is likely to be closer to the multiple equilibria region as well. From experiment Crev it can be inferred that a $\delta_p = 0.5$ Sv anomaly is able to extend the multiple equilibria area almost to the $\gamma_p = 0$ Sv line.

Even if the values of δ_p and γ_p needed to collapse the model, or even reach the multiple equilibria regime, are obviously model-dependent, the anomalies associated with these transitions in SPEEDO can provide an efficient guide to demonstrate whether ME of the AMOC exist in other climate models.

Our experiments are based on artificially imposing changes to surface freshwater fluxes but we argue that similar results may hold when the surface fluxes change due to either physical processes as global warming or modifications in a climate model aimed at e.g. correcting biases in surface fluxes. Regarding the latter point, underestimation of stratocumulus cover at low latitudes is a well known issue in numerical models [58] that is very likely to have a strong impact on surface salinity in the south eastern Atlantic. Such a model bias, and its correction, would lead to anomaly patterns very similar to the dipole used in the present work. Also Agulhas leakage, its misrepresentation in ocean models, in particular at low resolution, and possible changes in it due to natural

likely to be affected by changes in resolution, or by different parametrization. The results of Hawkins et al. [50] and de Vries and Weber [21] hint at the possibility that M_{ov} could be a reliable indicator of an approaching collapse of the AMOC. It is anyway of fundamental importance to carefully consider all the different components of the freshwater budget, as different models may have a markedly different behaviour for some of the terms that were not considered in this work (e.g. the magnitude of Bering Strait transport may be non negligible, the deep overturning between the Southern Ocean and the Atlantic may give a substantial contribution to M_{ov} and relative importance of advective and diffusive terms may change the compensating behaviour of M_{ov} and M_{az}). It is also important to stress that there is no theoretical background, at present, supporting the use of M_{ov} as a stability indicator far from the steady state, so that great care should be taken when analysing transient experiments as done by Hawkins et al. [50]. We also can not exclude that simulations at higher resolution, or with more sophisticated parametrization, may uncover the importance of other processes that could not be taken into account in the present work. In the work of Farneti et al. [32], as an example, the mesoscale eddies provide a sink to the potential energy produced by the Ekman flux in the Southern Ocean that would otherwise be absent at lower resolution, markedly changing the response of the ocean to wind stress variability. Whether this, or similar processes, are relevant for the stability of the AMOC is at the moment unclear.

A correct representation of salinity, and consequently of the equivalent freshwater fluxes, is needed if any inference or prediction on the stability of the AMOC has to be drawn from model results. Changes in the surface fluxes, either physically motivated or artificially imposed as in the case of this work, can change entirely the response of the overturning circulation to an identical perturbation. A key result of this study is that the stability of the AMOC crucially depends on salinity/freshwater anomalies in the South Atlantic. This result challenges the traditional view of the stability of the AMOC being solely determined by processes in the North Atlantic.

MERIDIONAL OVERTURNING CIRCULATION: STABILITY AND OCEAN FEEDBACKS IN A BOX MODEL.

A box model of the inter-hemispheric Atlantic meridional overturning circulation is developed, including a variable thermocline depth for the tropical and subtropical regions. The circulation is forced by winds over a periodic channel in the south and by freshwater forcing at the surface. The model is aimed at investigating the ocean feedbacks related to perturbations in freshwater forcing from the atmosphere, and to changes in freshwater transport in the ocean. These feedbacks are closely connected with the stability properties of the meridional overturning circulation, in particular in response to freshwater perturbations.

The role of the freshwater transport by the overturning circulation (M_{ov}) as a stability indicator is discussed. It is investigated under which conditions its sign at the latitude of the southern tip of Africa can provide information on the existence of a second, permanently shut down, state of the overturning circulation in the box model. M_{ov} will be an adequate indicator of the existence of multiple equilibria only if salt-advection feedback dominates over other processes in determining the response of the circulation to freshwater anomalies. M_{ov} is a perfect indicator if feedbacks other than salt-advection are negligible.

This chapter has been accepted for publication as:

A. A. Cimadoribus, S. S. Drijfhout and H. A. Dijkstra. Meridional overturning circulation: stability and ocean feedbacks in a box model. *Clim. Dyn.*, in press, 2012.

4.1 INTRODUCTION

The stability of the Atlantic Meridional Overturning Circulation (AMOC) in the ocean has been a topic of investigation in oceanography and climatology since the pioneering work of Stommel [99]. The central idea of Stommel [99] is that the AMOC is linked to a feedback between the circulation and the salinity advected from the tropics to the subpolar regions, increasing density where sinking occurs and enhancing the AMOC strength. This mechanism, usually referred to as salt-advection feedback, is also responsible for the collapse and reversal of the circulation, if a sufficiently strong freshwater anomaly is dumped in the subpolar areas. This concept was originally developed to describe the AMOC in a single hemisphere, with the circulation being driven only by buoyancy forcing and, implicitly, by mixing-induced vertical diffusivity at low latitudes. It has been used to describe the inter-hemispheric AMOC as well, with the circulation being driven by a north–south, instead of equator–pole density difference [54, 86, 89]. Even if extremely simple, this paradigm has been helpful in understanding the behaviour of the AMOC in more complex General Circulation Models (GCMs) of various complexity, which all show that the AMOC can substantially weaken if a sufficiently strong perturbation is applied.

It has been shown in several earth system models of intermediate complexity that if the freshwater forcing over the North Atlantic (say measured by a parameter γ) is increased, the AMOC will first slow down and then undergo a more or less abrupt transition to a collapsed state [88]. The point of collapse is believed to be associated, in the terminology of dynamical systems theory, to a saddle node bifurcation. At such a point, which we will call L_1 , a previously stable steady state of the system (the present day ON state of the AMOC, see Fig. 4.1) loses its stability, and the system jumps to another stable steady state with little or reversed overturning in the Atlantic (the OFF state, see Fig. 4.1). If the forcing is then reduced again, the AMOC does not recover immediately, but stays collapsed until another critical value of the freshwater forcing is reached. At this second point, named L_2 , the OFF state loses its stability and the system jumps to the ON state, with vigorous overturning. In the region of γ between L_1 and L_2 , called the ME regime, two stable steady states coexist under the same boundary conditions, separated by an unstable steady state of the system, usually not observable in numerical models performing time integration.

In this context, it has been suggested that the freshwater transport by the AMOC at the southern border of the Atlantic Ocean, usually shorthanded $M_{ov}^{30^\circ S}$, may play a special role in determining AMOC stability [21, 54]. In analogy with the original salt-advection feedback of the Stommel model, the sign of the freshwater transport may determine whether the AMOC could be permanently

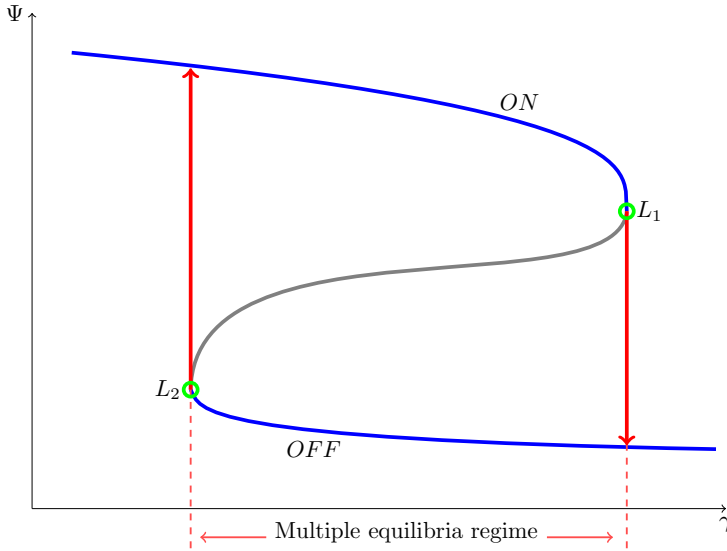


Figure 4.1: Sketch of a bifurcation diagram for the AMOC strength Ψ , as a function of a generic freshwater forcing strength γ . The blue lines mark the two stable steady state solutions, ON and OFF; the grey line marks the unstable solution connecting the two stable ones. At points L_1 and L_2 , marked by green circles, the stability of the steady state solution changes. The range of γ -values between the two dashed vertical red lines is the ME regime, where two stable states coexist under the same boundary conditions. Changing γ further, the system jumps from one solution to the other at the two limit points L_1 and L_2 , as indicated by the red arrows.

collapsed or, in other words, if a second stable steady solution, with a very weak or reversed AMOC, exists.

If $M_{ov}^{30^\circ S}$ is negative, the AMOC is importing salt into the basin. A negative perturbation on the AMOC would determine a negative salinity anomaly, and consequently a negative density anomaly, within the Atlantic basin. If sufficiently strong, this density anomaly can be advected northward up to the sinking regions of the northern North Atlantic, either by the gyres or by the AMOC itself. There, it would feed back onto the AMOC strength, reducing the downwelling rate and amplifying the initial negative AMOC perturbation, providing a mechanism for the collapse of the AMOC. If, on the other hand, $M_{ov}^{30^\circ S}$ is positive, the AMOC is importing freshwater into the Atlantic basin. A negative perturbation in AMOC strength would then lead to a positive density perturbation, as it would bring a positive salinity anomaly in the Atlantic, and no amplification of the initial perturbation is possible. In this second case, even if the AMOC can be slowed down substantially or even reversed by a sufficiently strong freshwater

perturbation, it will spontaneously recover when the perturbation is removed, as no stable OFF state of the AMOC exists under the unperturbed boundary conditions.

In de Vries and Weber [21], it is shown that bringing $M_{ov}^{30^{\circ}S}$ to negative values through appropriate surface freshwater flux anomalies it was possible to permanently collapse the AMOC if net evaporation over the North Atlantic is below a critical value. In particular, it was shown that a dipole freshwater anomaly applied over the southern portion of the Atlantic Ocean affects the freshwater transport by the southern subtropical gyre circulation (usually referred to as $M_{az}^{30^{\circ}S}$), and hence can affect $M_{ov}^{30^{\circ}S}$. With an increase of $M_{az}^{30^{\circ}S}$, $M_{ov}^{30^{\circ}S}$ can eventually become negative, enabling a permanent shut-down of the AMOC.

Recently, a series of numerical experiments with two different GCMs was performed to further explore the importance of freshwater budget of the Atlantic Ocean. In Cimadoribus et al. [15], it is shown that the freshwater transport by the southern subtropical gyre is of paramount importance in determining the stability of the AMOC, even if the overturning rate is only weakly sensitive to $M_{az}^{30^{\circ}S}$. Similarly to de Vries and Weber [21], $M_{az}^{30^{\circ}S}$ and $M_{ov}^{30^{\circ}S}$ were tuned through freshwater anomalies at the surface, showing that the sensitivity of the AMOC to changes in the net precipitation over the Atlantic Ocean depends strongly on how the freshwater transport at the southern border of the Atlantic is divided between the gyre and the AMOC. In particular, as the freshwater transport by the gyre is increased, $M_{ov}^{30^{\circ}S}$ decreases and this leads to a permanent collapse of the AMOC for weaker reductions of the net evaporation. The AMOC can even be collapsed by solely increasing $M_{az}^{30^{\circ}S}$, without changing the integrated net evaporation over the Atlantic basin. A similar sensitivity of the AMOC to the freshwater transport in the South Atlantic can be inferred from the work of Marsh et al. [74]. They show that, in a low resolution model, changes in the zonal salinity contrast over the South Atlantic control the AMOC sensitivity to freshwater perturbations.

The results above consistently point to the importance of the freshwater (that is, buoyancy) forcing in setting the AMOC stability and strength in connection with the salt-advection feedback, but they are in apparent contradiction with the point of view of Ferrari and Wunsch [33], who suggest that the direct mechanical forcing by the wind over the Southern Ocean is the main driver of the AMOC. A synthesis of these two views was attempted in Wolfe and Cessi [121] and Nikurashin and Vallis [81]; a series of numerical experiments with an ocean-only GCM (both at eddy-resolving and non eddy-resolving resolutions) contribute to a description of the AMOC as driven by the wind-induced upwelling in the Southern Ocean, but with buoyancy distribution controlling whether an active pole-to-pole overturning can actually take place. A similar

synthesis of these two views was attempted in simple models by Gnanadesikan [42] and Johnson et al. [57] (from now on J07).

On the other hand, the results of Longworth et al. [69] point to the importance of the transport of salinity by the wind driven gyres (represented in a box model by horizontal diffusion) for the stability of the AMOC. In particular, they show that a simultaneous increase in the horizontal diffusivity in both hemispheres is in general a stabilising factor for the AMOC, providing a way to transport salt from low to high latitudes that bypasses the salt-advection feedback mechanism.

In this paper, the main goal is to understand the results of Cimatoribus et al. [15] in the framework of a box model, and to better understand the validity of $M_{ov}^{30^{\circ}S}$ as an indicator of AMOC stability. The box model is based on that developed by J07 and Gnanadesikan [42], with a few important differences. Its formulation and solution method are described in Sec. 4.2. We are particularly interested in understanding the role of the freshwater transport by the gyre and overturning circulation at the southern entrance of the Atlantic Ocean on the changes in stability of the AMOC found in Cimatoribus et al. [15]. This can be done by including a representation of the transport by the southern subtropical gyre as a horizontal diffusive transport, similarly to what was done by Longworth et al. [69]. The sensitivity of the solutions of the model to this as well as to other parameters of the system is described in Sec. 4.3. In relation to this, the conditions under which $M_{ov}^{30^{\circ}S}$ can provide useful information on the stability properties of the AMOC are discussed in Sec. 4.3.3.

4.2 METHODS

4.2.1 Model definition

The box model (see Fig. 4.2) used in this work consists of a basin spanning both hemispheres (which represents the Atlantic Ocean) connected in the south to a periodic channel (representing the Southern Ocean, shorthanded s). It is assumed that the entire flow at depth from the Atlantic Ocean is upwelled into the mixed layer represented by box s , due to Ekman pumping. Upwelling in other basins, due to diapycnal mixing, is thus neglected in this work. The basin has four other boxes: a pycnocline (made of two boxes: t and ts) and a deep box (box d) separated by a thermocline at a variable depth D , and a northern box (box n) of fixed volume.¹ The northern box only represents that portion of the Northern Seas where downwelling actually takes place. Differently from J07 and Gnanadesikan [42], the Atlantic thermocline and the Southern

¹ Since density differences in the model are dominated by (fixed) temperature differences, the words pycnocline and thermocline can be used equivalently.

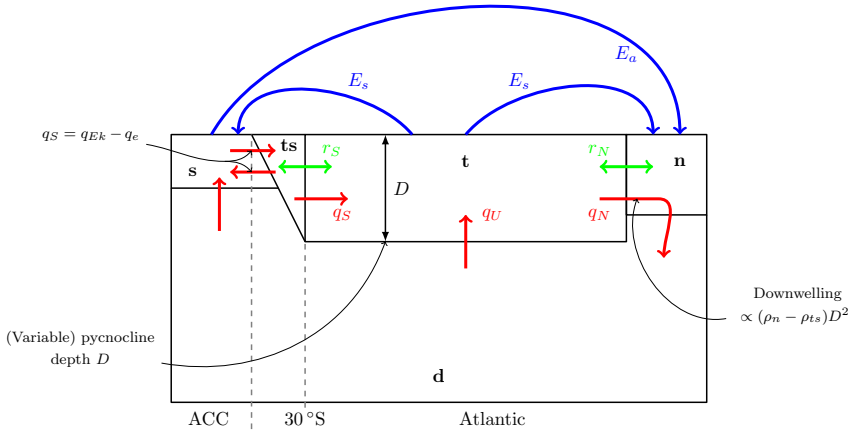


Figure 4.2: Structure of the box model, with flow pathways connecting the different boxes. Red arrows represent net volume fluxes (with names in the same colour), green arrows represent gyre exchanges between the different boxes (with names in the same colour), blue arrows are water vapour transports through the atmosphere (with names in the same colour). In black, the boxes names.

Ocean are connected through a further box, named ts . The box extends south of the latitude of the tip of the African continent (approximately 30°S). The use of this box, motivated in detail in the following sections, enables to compute the meridional density gradient within the Atlantic basin, assumed to be the driver of the overturning circulation (see Secs. 4.2.1.1 and 4.2.1.2). This region is characterised by larger isopycnal slopes than within the Atlantic basin (see, e. g. Lumpkin and Speer [70]), with the thermocline becoming shallower moving poleward. The box ends in the south at the latitude where the deepest Antarctic Intermediate Waters (northward flowing) outcrop, approximately 40°S [70]. The depth of this box at its northern end is the same depth scale D used for the main thermocline box t . This depth scale is obtained from the thermocline model used by J07 and Gnanadesikan [42], but with the thermocline box divided in the two boxes t and ts , as described. The temperature is fixed in all boxes, while the salinities are prognostic variables of the model. This is a common choice in simple models of the AMOC, stemming from the much shorter decay time of large scale temperature perturbations in the ocean, with respect to salinity ones. This choice implies that we will neglect any feedback with the atmosphere. This appears as an obvious limitation of the work; but it may not

be, as recent studies suggest that atmospheric feedbacks play a secondary role for AMOC stability [3, 23, 92].

The thermocline model results from a balance between the following terms:

1. Ekman transport into the Atlantic basin from the Southern Ocean (and through the ts box), associated with the wind-driven upwelling in the Southern Ocean (q_{Ek});
2. eddy induced flow out of the Atlantic basin (from box ts to box s) due to baroclinic instability (q_e);
3. diffusively controlled upwelling of water from the deep layer (q_U);
4. downwelling in the North Atlantic (q_N).

Within box t, we assume that the AMOC can be approximated as a coherent flow, northward in the thermocline and southward at depth. This thermocline model can be paralleled to the view of the AMOC by Wolfe and Cessi [121], which also includes a wind-driven upwelling (“pushed” from the south) and a diffusively controlled upwelling inside the basin, the latter compensating only for a small part of the downwelling in the north. The volume of the Atlantic thermocline is the sum of the volumes of boxes t and ts, and the volume budget of the thermocline thus reads:

$$\begin{aligned}
 \frac{\partial(V_t + V_{ts})}{\partial t} &= \frac{\tau L_{xS}}{\rho_0 |f_S|} - A_{GM} \frac{L_{xA}}{L_y} D + \frac{\kappa A}{D} - q_N \\
 &= q_{Ek} - q_e + q_U - q_N \\
 &= q_S + q_U - q_N, \text{ with } q_S = q_{Ek} - q_e.
 \end{aligned}
 \tag{4.1}$$

In the equation, τ is an average zonal wind stress amplitude over the periodic channel region, L_{xS} is the zonal extent of the Southern Ocean, L_{xA} is the zonal extent of the Atlantic Ocean at its southern end, D is the thermocline depth, ρ_0 is a reference density, f_S is the Coriolis parameter in the frontal region of the Southern Ocean, A_{GM} is an eddy diffusivity, L_y is the meridional extent of the frontal region, A is the horizontal area of the Atlantic thermocline and κ is the vertical diffusivity. The total volume flux at the southern boundary of boxes t and ts is called q_S ; it is the difference between the Ekman inflow and the outflow due to baroclinic instability, while q_N , the downwelling flux in the north, is left unspecified for the moment. As the Ekman inflow in the Atlantic Ocean is related to the wind forcing over the whole Antarctic Circumpolar Current (ACC) [2, 35], the zonal width of the entire Southern Ocean is used in the computation of q_{Ek} . The zonal width of the Atlantic Ocean is used instead for computing the eddy outflow into the periodic channel. The volume of the box t is given by $V_t = AD$, while that of box ts by $V_{ts} = L_{xA}L_yD/2$. It can be

seen from Eq. (4.1) that the volume flux from the box s goes through box ts into the main thermocline without any change, we thus neglect any diapycnal upwelling within box ts . As far as the thermocline model is concerned, boxes t and ts behave as a whole, and the model is in fact completely equivalent to that of J07 and Gnanadesikan [42].

The model can be interpreted as an analogue of the adiabatic pole-to-pole circulation paradigm of Wolfe and Cessi [121] and Nikurashin and Vallis [81]. Diabatic fluxes mainly take place in the north, at the interface between boxes t and n , where thermocline waters are made denser by the interaction with the atmosphere, and in the Southern Ocean, where water flowing northward in the Ekman layer gains buoyancy. In the interior, the flow is mainly adiabatic, and the lower branch of the overturning is virtually isolated from the upper one, apart from the diffusive upwelling q_U , very small in our configuration. The upwelling in the south is also adiabatic, as water mass transformation only takes place when the lower branch of the AMOC enters the box s , the mixed layer of the ACC.

4.2.1.1 *The scaling for q_N*

Based on geostrophy, J07 used the scaling $q_N \propto D^2(\rho_d - \rho_t)/\rho_0$ for the downwelling [42, 56, 83], with ρ_d the density of the deep box and ρ_t that of the thermocline box. Since at steady state the densities of the deep and northern boxes are equal, this scaling can be written as $q_N \propto D^2(\rho_n - \rho_t)/\rho_0$, with ρ_n the density of the northern box. The density difference between the northern and thermocline boxes is almost entirely determined, in the box model, by the temperature difference (fixed in J07 and here). Using this scaling, the sensitivity to freshwater fluxes is thus too low (more than 1 Sv is needed to collapse the AMOC—not shown). Furthermore, if a representation of the southern subtropical gyre is included in the box model of J07, the AMOC shows no sensitivity to the gyre strength and to the freshwater transport associated with it (not shown). This latter result is in striking disagreement with the results of Cimadoribus et al. [15], as discussed in section 4.1.

Levermann and Fürst [67] tested the scalings used in J07 and Gnanadesikan [42]. They show that the downwelling can be described by $q_N = \eta D^2 \Delta\rho$, with $\Delta\rho$ the density difference between north-western and tropical water at the base of the thermocline. Even if the validity of the above results for different models is still uncertain [20], the connection between overturning strength and meridional pressure gradients is well established (see e. g. Cessi and Wolfe [14], Sijp et al. [95]). In the simple context of the box model, this translates into a meridional density gradient in the thermocline [83]. We exploit this idea by taking $\Delta\rho = (\rho_n - \rho_{ts})/\rho_0$. In our model, the box ts is the southern end of the thermocline, which means that the overturning circulation is proportional

to the density difference between the sinking regions in the north and the southern end of the thermocline. The thermocline model then reads:

$$\left(A + \frac{L_{xA}L_y}{2}\right) \frac{dD}{dt} = \frac{\kappa A}{D} + \frac{\tau L_{xS}}{\rho_0 |f_S|} - A_{GM} \frac{L_{xA}}{L_y} D - \eta \frac{(\rho_n - \rho_{ts})}{\rho_0} D^2. \quad (4.2)$$

From a heuristic point of view, this scaling for q_N implies that, when a large meridional density gradient is present, the sensitivity of the AMOC is mainly determined by changes in thermocline depth (neglecting the variable thermocline depth leads in fact to unrealistic sensitivity to wind stress, not shown), while a freshwater flux in the north leads to a collapse due to the reduction of the inter-hemispheric density difference. We thus view the collapse due to a freshwater perturbation as “buoyancy driven”, even though the sensitivity of the AMOC in the ON state is dominated by “wind driven” dynamics (e. g. changes in the Ekman inflow). Even though we can collapse the AMOC exploiting a buoyancy flux, reducing the wind stress over the Southern Ocean below a critical value also brings q_S to zero (see Sec. 4.3.1.1), leaving a purely diffusive intrahemispheric AMOC ($q_N = q_U > 0$) similarly to what is suggested by the results of Wolfe and Cessi [121].

4.2.1.2 *The role of the box ts*

The thermocline model of Eq. (4.2) is equivalent to the one defined in J07, the only difference being our thermocline box split into two boxes, in order to emphasise the importance of the meridional density gradient.

Considering the salinity transport, instead, we proceed in a different way from J07. We argue that at the southern border of the thermocline (the southern border of box ts in our model) the Ekman inflow and eddy outflow, whose difference gives the net volume flux, have to be taken into account separately concerning the salt transport. The salt flux from box s to box ts has then to be written as $q_{Ek}S_s - q_eS_{ts}$. In other words, even if the net volume flux and net density flux may sum to zero, there can still be exchange of salt between the Southern Ocean and the thermocline. In case of no net volume flux ($q_{Ek} = q_e$) the salt transport must be compensated in density by heat transport (not considered explicitly in this work). This salinity transport must then be associated to transport of spiciness: it represents in this case an isopycnal salinity flux. In general, for $q_{Ek} \neq q_e$, the net volume flux will be associated with density transport on top of this isopycnal salinity transport. Although the Ekman and eddy fluxes may compensate globally, they will not do so locally, so that transport of properties is still present. From box ts to box t, instead, we assume that the flow is coherent because the flow is already within the thermocline layer, in geostrophic balance and with less prominent baroclinic eddy flow. The transport of salt from box ts to box t can then be written simply as $q_S S_{ts}$ (for the

case of a northward net flow). Upwelling in the box s is also taken proportional to the net flow q_S .

A last connection between boxes ts and t is added through a diffusive constant, to represent in the simplest possible way the transport by the southern subtropical gyre, similarly to what was done by Longworth et al. [69] and J07 (the latter only considered the northern subpolar gyre). We argue that, if the AMOC is sensitive to the difference between the sinking regions and the thermocline waters north of the ACC, the southern subtropical gyre may play a very important role in setting this density difference. The argument in J07 of the effect of r_S being negligible, at least in comparison with the gyre in the northern part of the basin, does not seem to be applicable in this context.

With this configuration, we neglect the interaction with the atmosphere of the area represented by box ts . This choice is done for simplicity, but seems to be at least indirectly supported by Garzoli and Matano [38], who show that little mass water transformation takes place for lighter water classes in this region (their Fig. 6).

A more important assumption in this work is the neglect of the exchanges between the Atlantic Ocean and the other Ocean basins, in particular with the Indian Ocean through Agulhas Leakage. This is still a highly debated subject, outside the scope of the present paper.

4.2.1.3 Salt conservation equations

The equations needed to close the system are given by salt and volume conservation in each box. They comprise the following set of equations for a state of the AMOC similar to the present day one ($q_N > q_S > q_U > 0$):

$$\frac{d(V_t S_t)}{dt} = q_S S_{ts} + q_U S_d - q_N S_t + r_S(S_{ts} - S_t) + r_N(S_n - S_t) + 2E_s S_0, \quad (4.3a)$$

$$\frac{d(V_{ts} S_{ts})}{dt} = q_{Ek} S_s - q_e S_{ts} - q_S S_{ts} + r_S(S_t - S_{ts}), \quad (4.3b)$$

$$V_n \frac{dS_n}{dt} = q_N(S_t - S_n) + r_N(S_t - S_n) - (E_s + E_a)S_0, \quad (4.3c)$$

$$\frac{d(V_d S_d)}{dt} = q_N S_n - q_U S_d - q_S S_d, \quad (4.3d)$$

$$V_s \frac{dS_s}{dt} = q_S S_d + q_e S_{ts} - q_{Ek} S_s - (E_s - E_a)S_0, \quad (4.3e)$$

$$S_0 V_{tot} - V_n S_n - V_d S_d - V_t S_t - V_{ts} S_{ts} - V_s S_s = 0, \quad (4.3f)$$

with V being the volume of the various boxes and $V_{tot} = V_n + V_t + V_{ts} + V_d + V_s$. The last equation states salt conservation in the model. S is the salinity in the various boxes, r_S is the gyre exchange between boxes t and ts , while

r_N is the gyre exchange between the thermocline and northern box. The salt transport by the gyres takes in this simple framework the form of a diffusive constant. E_s is the symmetric part of the atmospheric freshwater flux, from the thermocline to the boxes n and s. E_a is the asymmetric part of the atmospheric freshwater flux, transferring freshwater from the Southern Ocean into the box n. Physically, the asymmetry in the freshwater forcing is due to the different sizes of the boxes in the north and in the south, differences in precipitation amount connected with the fact that box n is closer to the pole than box s and differences in the runoff from the continents. We will change E_a , changing the North–South density gradient, for collapsing the AMOC. In reality, possible sources of the freshwater flux are ice-sheets at high latitudes or Arctic sea-ice, not represented in the box model; these will generally cause a net change in the total freshwater content of the ocean. Using E_a as a “hosing” flux, enables to maintain a closed salinity budget, and thus to explore steady states of the system; the approach is similar to that used in GCMs, where “hosing” fluxes are usually compensated over the rest of the Ocean surface. Both E_s and E_a are represented through a virtual salt flux. Despite the different definition used here, the atmospheric freshwater fluxes E_a and E_s can be cast in a form equivalent to that used in Longworth et al. [69] and Scott et al. [92]. S_0 is a reference salinity and a linear equation of state is used, i. e. $\rho = \rho_0(1 - \alpha(T - T_0) + \beta(S - S_0))$, where α and β are the constant thermal expansion and haline contraction coefficients respectively, T_0 is a reference temperature.

To summarise, there are six differences in our model definition from J07: (i) a different choice of the box sizes, to account for our interpretation of the model as the Atlantic and Southern Oceans alone; (ii) the thermocline layer is split in two meridionally at the latitude of the southern tip of Africa; (iii) the two components of salt advection between the southern box and the thermocline, due to the Ekman and eddy fluxes, are treated separately; (iv) the meridional density gradient used in the scaling of q_N ; (v) the use of a term representing gyre exchange (r_S) between boxes t and ts and (vi) a slightly different parameter choice including lower vertical and eddy diffusivities.

4.2.1.4 Reference solution

At steady state, if $q_N > q_S > 0$, it follows that $S_d = S_n$ from Eq. (4.3d), as $q_S = q_N - q_U$. The reference parameter values are shown in Tab. 4.1. A solution for the system of Eqs. (4.2) and (4.3) can be found using Mathematica software [122], but only after substituting the parameters with their numerical values. The solution for the reference configuration of Tab. 4.1 is reported in Tab. 4.2.

V_{tot}	$3.0 \times 10^{17} \text{ m}^3$	V_s	$9 \times 10^{15} \text{ m}^3$
V_n	$3 \times 10^{15} \text{ m}^3$	A	$1.0 \times 10^{14} \text{ m}^2$
ρ_0	1027.5 kg m^{-3}	α	$2 \times 10^{-4} \text{ K}^{-1}$
β	$8 \times 10^{-4} \text{ psu}^{-1}$	T_0	5°C
S_0	35 psu	L_{xS}	$3.0 \times 10^7 \text{ m}$
L_{xA}	$1.0 \times 10^7 \text{ m}$	L_y	$1.0 \times 10^6 \text{ m}$
f_S	-10^{-4} s^{-1}	T_n	5.0°C
T_{ts}	10.0°C	A_{GM}	$1700 \text{ m}^2 \text{ s}^{-1}$
E_s	$0.25 \times 10^6 \text{ m}^3 \text{ s}^{-1}$	E_a	$-0.1 \times 10^6 \text{ m}^3 \text{ s}^{-1}$
r_N	$5 \times 10^6 \text{ m}^3 \text{ s}^{-1}$	r_S	$10 \times 10^6 \text{ m}^3 \text{ s}^{-1}$
τ	0.10 N m^{-2}	η	$3.0 \times 10^4 \text{ m s}^{-1}$
κ	$1 \times 10^{-5} \text{ m}^2 \text{ s}^{-1}$		

Table 4.1: Reference values of the parameters used in Eqs. (4.2) and (4.3).

D	696 m	S_n	35.0 psu	S_d	35.0 psu
S_t	35.2 psu	S_{ts}	34.6 psu	S_s	34.4 psu
q_N	18.8 Sv	q_S	17.4 Sv	q_U	1.4 Sv

Table 4.2: Steady solution for the reference configuration of the model (using the parameters in tab. 4.1).

Similarly to J07, the reference solution consists of a flow northward in the boxes ts and t and southward at depth, downwelling from box n to box d and upwelling from box d to box s. Diffusive upwelling takes place from box d to box t. The northern box is saltier than the southern one under symmetric forcing, due to the asymmetry of the circulation itself (in other words, the circulation is maintained by the salt-advection feedback). Differently from J07, the value of thermocline depth is close to what commonly observed in the real ocean and in GCMs. This is mainly due to smaller downwelling flux than in J07, closer to the present day estimate of $18.7 \pm 2.1 \text{ Sv}$ [18], given by the different scaling for q_N and by the smaller vertical diffusion considered here. The value of the hydraulic constant η used is the one estimated in [67], but we stress that this quantity is badly constrained since it will strongly depend on the choice of the temperature difference between boxes n and ts (or, in a more realistic framework on the locations used for the computation of the meridional density difference). For this reason, we will study the model at different values of the

hydraulic constant η (0.5, 1 and 1.5 times the value given by Levermann and Fürst [67]), in order to assess the robustness of the results.

The temperature chosen for the box T_{ts} is 10°C , giving a difference of 5°C between the northern box and the southern end of the thermocline. This temperature is representative of the waters north of the periodic channel in the South Atlantic. This temperature, or the temperature difference between boxes n and ts ,² is particularly important since it determines the strength of the AMOC for fixed η and a given salinity distribution. The choice of this temperature difference was made in order to use the estimate of η given by Levermann and Fürst [67], the most recent we are aware of, and to obtain at the same time a realistic AMOC rate.

A negative value of E_a is used for the reference solution, to account for the different interpretation of the boxes in the model, with respect to J07. A negative E_a is needed in order to reduce the export of freshwater from the Atlantic Ocean, and also to reduce the net precipitation over the sinking regions of the North Atlantic, also considering the asymmetry of the sizes of box n and s .

4.2.1.5 Freshwater budget

In order to compare our results with those from more complicated models, we compute the equivalent freshwater budget of the ‘‘Atlantic’’ basin north of 30°S (see Fig. 4.2). With the definitions:

$$M_{ov} = -\frac{1}{S_0} q_S (S_{ts} - S_d),$$

$$M_{az} = -\frac{1}{S_0} r_S (S_{ts} - S_t),$$

valid under the same conditions considered in Eqs. (4.3), we find that the net steady evaporation from the Atlantic basin must be balanced by the freshwater import by the ocean circulation:

$$(E_s - E_a) = M_{ov} + M_{az}. \quad (4.4)$$

This budget includes the dominant terms in GCMs of various complexity [15, 30]. Eq. (4.4) states that the freshwater transported through the atmosphere out of the basin must be balanced by the freshwater transport by the ocean circulation, split into its overturning (M_{ov}) and gyre (M_{az}) components. M_{az} can be controlled by varying r_S , and M_{ov} will change in the opposite way, as long as the net evaporation is kept constant. This behaviour, which is trivial in

² Since the equation of state is linear, only temperature (or salinity) differences are physically relevant.

this model, has been observed in GCMs as well. In Cimadoribus et al. [15], M_{az} is changed using anomalies in the surface freshwater flux instead of perturbing the gyre strength, and M_{ov} reacts in a similar way as here, compensating for the changes in the azonal transport and keeping the total budget closed.

4.2.2 Solution method

The system of equations (4.2) and (4.3) is studied using the software AUTO-07p, which enables the continuation and bifurcation of solutions of systems of Ordinary Differential Equations (ODEs) [29]. Only exact (within numerical accuracy) steady states are obtained with this technique, and no transient behaviour is studied in any part of this work.

The system of equations (4.2) and (4.3) can be written as the autonomous ODEs system:

$$\frac{d\mathbf{x}(t, \mathbf{p})}{dt} = \mathbf{G}(\mathbf{x}(t), \mathbf{p}), \quad (4.5)$$

with \mathbf{x} the 6-dimensional state vector, \mathbf{p} the vector containing the system parameters, and \mathbf{G} a nonlinear mapping. Given a steady state solution \mathbf{x}_0 of (4.5) for a particular parameter set \mathbf{p}_0 , AUTO-07p can track the evolution of the steady-state solution as the value of one parameter of the system is changed; the solutions can be stable or unstable, and their stability is determined as well. The initial solution \mathbf{x}_0 can be analytical or numerical, as long as it is known with sufficient numerical precision. The software is based on Newton's method for continuation of steady states; for further details, see Doedel and Oldeman [29] and references therein. Special points, such as saddle node bifurcations, are detected and can be continued in two parameters, obtaining the locus of those special points in a parameter plane. Multiple steady states can be identified following the solution beyond a special point and, more in general, a systematic exploration of the parameter space is possible. All the results are obtained with small continuation step sizes, so that the results are not sensitive to the value actually used. The relative convergence criterion for the steady solution in AUTO-07p is set to 10^{-7} .

In the next section, starting from the reference solution obtained from Mathematica (see Sec. 4.2.1.4), the sensitivity of the model to several parameters is studied. Solutions are continued within physically plausible regions of the parameter space, or down to the point where $q_S = 0$. When the sensitivity to freshwater fluxes is studied, the solution is continued for $q_S < 0$ down to the point at which the downwelling in the north stops. When q_S changes sign, the

definition of the box model has to be changed. In particular, Eqs. (4.3a), (4.3b), (4.3d) and (4.3e) become:

$$\begin{aligned}\frac{d(V_t S_t)}{dt} &= q_S S_t + q_U S_d - q_N S_t + r_S (S_{ts} - S_t) + r_N (S_n - S_t) + 2E_s S_0, \\ \frac{d(V_{ts} S_{ts})}{dt} &= q_{Ek} S_s - q_e S_{ts} - q_S S_t + r_S (S_t - S_{ts}), \\ \frac{d(V_d S_d)}{dt} &= q_N S_n - q_U S_d - q_S S_s, \\ V_s \frac{dS_s}{dt} &= q_S S_s + q_e S_{ts} - q_{Ek} S_s - (E_s - E_a) S_0,\end{aligned}$$

for a negative q_S , while the equations for the northern box and total salt conservation are unchanged. The two sets of equations are automatically chosen in order to match the solution at $q_S = 0$.

The solutions are not continued below $q_N = 0$ as then the AMOC is completely reversed and the scaling for q_N is not meaningful anymore. In fact, if q_N was allowed to reach negative values, the scaling used in the ON state would represent an enhanced upwelling in the high latitudes of the North Atlantic, for which no plausible physical mechanism is known. Furthermore, a reversed AMOC is determined by the shallow outflow from the Atlantic, in the present box model this is due to an eddy flux stronger than the Ekman transport. Whether such a situation could exist in reality is unclear. With these limitations in mind, the study stops at the point where $q_N = 0$ with q_S small and negative. The change in sign of q_S when the downwelling in the north is weaker than the mixing-driven upwelling ($q_N < q_U$) does not affect the fundamental properties of the model, which is still controlled by the same scaling law for q_N . On the contrary, the model is no more valid when $\Delta\rho$ and q_N change sign. An extension of the model including a consistent representation of the completely reversed AMOC is beyond the scope of this work.

4.3 RESULTS

This section is comprised of three subsections. In subsection 4.3.1 we investigate the sensitivity of the model solutions to the southern ocean wind stress and the strength of the southern gyre. In subsection 4.3.2, the stability of the AMOC to freshwater perturbations is considered while in subsection 4.3.3, the results in 4.3.2 are interpreted using the freshwater budget of the box model.

4.3.1 Model sensitivity

In general, the sensitivity to the model parameters is very similar to that found in J07. We will briefly discuss the importance of wind stress, and then analyse the sensitivity of the model to the gyre transport and to changes in the freshwater fluxes.

4.3.1.1 Southern Ocean wind stress

In Fig. 4.3 the sensitivity of D , q_S and q_N to the wind stress τ is shown. When the wind stress is changed, the role of thermocline depth in determining the AMOC strength is dominant. The values of the volume transports change mostly due to the increased Ekman inflow at the southern border, generating a deeper thermocline and a consequently stronger outflow in the north, which is qualitatively the same behaviour as in J07. The changes in the meridional density difference, with a reduction of the salinity in the box ts (due to the increased inflow from the fresher box s) but little change in the northern box, enhance the changes in q_N and q_S . Below a certain critical value of τ (approximately 0.02 N m^{-2}) the eddy flux becomes as large as the Ekman inflow, and the waters sinking in the north are upwelled only through diffusion within the Atlantic basin. Without a net inflow from the Southern Ocean, the AMOC can not extend beyond the Atlantic basin, consistently with what is shown in the numerical experiments of [121]; no pole-to-pole AMOC is possible without wind-stress over the Southern Ocean.

4.3.1.2 Southern gyre

As discussed in Sec. 4.2.1.4, a basic representation of the southern subtropical gyre is included in this work. The sensitivity of D , q_S and q_N to r_S is shown in Fig. 4.4. In addition, the sensitivity of M_{ov} and M_{az} is also shown in the bottom panel. Both q_S and q_N decrease when the gyre strength increases, with stronger sensitivity for lower values of r_S . This is a purely buoyancy driven response, which we could not reproduce using the J07 model with a term equivalent to r_S added to their equations (not shown). Downwelling in the north decreases due to the lowering of the north-south density difference, caused by the increased exchange between boxes ts and t which leads to a salinification of the southern end of the thermocline and a slight freshening of the box t. The thermocline depth increases moderately, in connection with the slightly stronger decrease of q_N compared to q_S , and a slightly decreased upwelling flux q_U . The northward volume transport into box ts is reduced by the stronger eddy outflow, associated with a deeper thermocline. This response is absent from J07 since r_S strongly

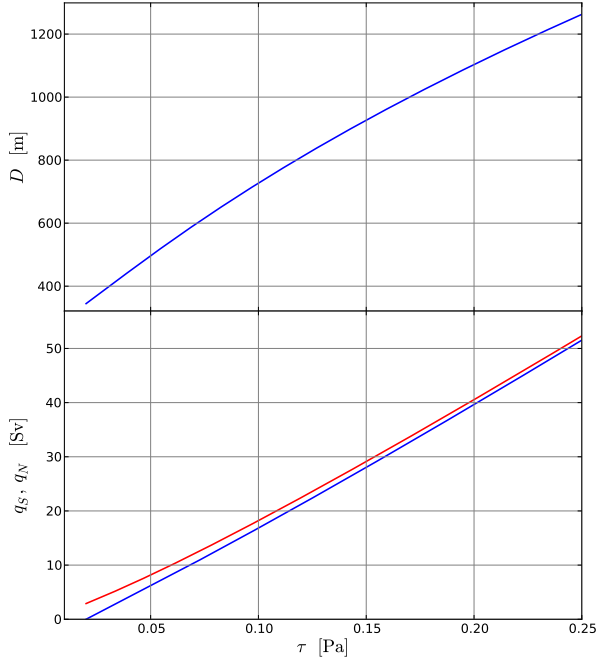


Figure 4.3: Sensitivity of D (top panel, blue), q_S (lower panel, blue) and q_N (lower panel, red) to the wind stress τ . All other parameters are kept at the reference values of Tab. 4.1.

increases the salinity of box ts, but very little that of boxes t, n and d. The scaling used in this work for q_N is thus affecting the AMOC (as it depends on $(\rho_n - \rho_{ts})$), contrary to the one used in J07 ($\propto (\rho_d - \rho_t)$).

As expected from the freshwater budget, Eq. (4.4), M_{ov} decreases and becomes negative as M_{az} increases from zero, similarly to what is observed in numerical experiments with GCMs [15, 21, 54]. This behaviour, trivial in the box model, has been exploited in GCMs to change M_{ov} , in order to reach the ME regime [15, 21]. In GCMs, this behaviour is usually induced by different means; M_{az} is increased not by modifying the gyre strength, but rather by perturbing the surface salinity, and M_{ov} compensates M_{az} due to changes in the intermediate depth ocean stratification [15].

The response of M_{az} to r_S saturates for large values of r_S . This is due to the decrease in the salinity difference between boxes ts and t as r_S increases, which limits the ability to tune M_{az} using r_S in the box model. Another limit of representing the gyre through a diffusive constant, already discussed by Longworth et al. [69], is the fact that the freshwater exchange depends on the

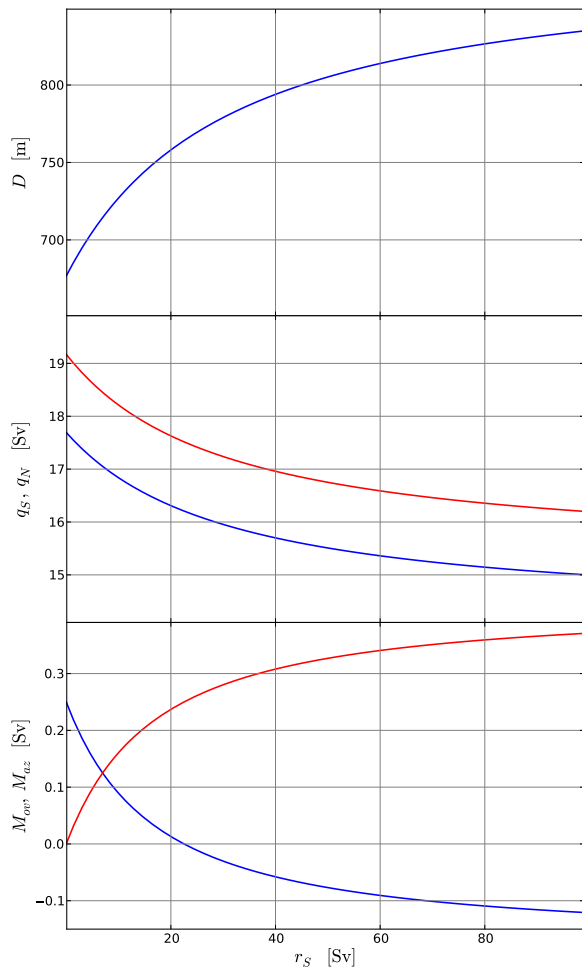


Figure 4.4: Sensitivity of D (top panel, blue), q_S (central panel, blue), q_N (central panel, red), M_{OV} (lower panel, blue) and M_{qz} (lower panel, red) to the gyre exchange between the boxes t_s and t (r_S). All other parameters are kept at the reference values of Tab. 4.1.

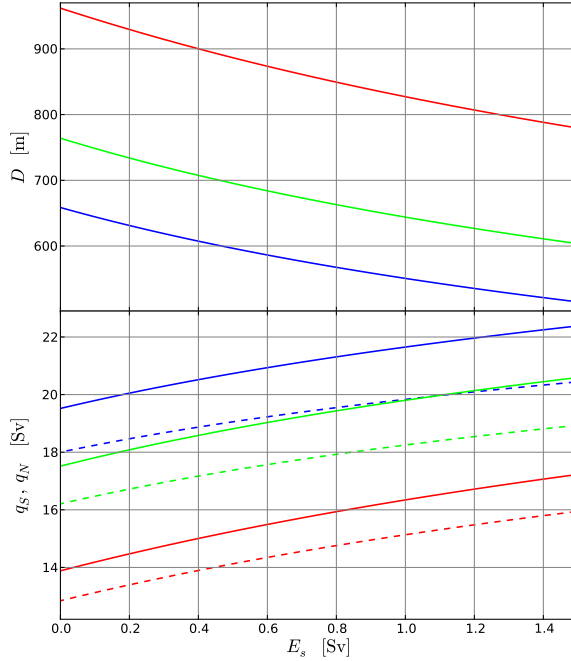


Figure 4.5: Sensitivity of D (top panel, blue), q_S (central panel, dashed) and q_N (central panel, full) to the symmetric freshwater flux E_s . The different colours (red, green and blue) refer to different η values: $(1.5, 3.0, 4.5) \times 10^4 \text{ m s}^{-1}$ respectively.

meridional density difference while in reality the freshwater transport by the wind-driven gyre will rather scale with the zonal salinity gradient.

4.3.2 Stability to freshwater perturbations

4.3.2.1 Symmetric freshwater flux

Opposite to what found in J07, the AMOC strength increases when E_s is increased (Fig. 4.5, the results are shown for three different values of η). The different sign of the sensitivity to E_s is due to the new definition of the q_N scaling. Increasing E_s , freshwater is moved from the thermocline box to the two high-latitude boxes. Given the sense of the overturning circulation, this produces an increase in the density difference between boxes n and ts, as the freshening by the freshwater forcing in the box n is partly compensated by increased salt advection from the thermocline, while box ts is made fresher by

its exchange with the southern box. The response is thus due to the asymmetry between north and south, induced by the AMOC itself; the sense of the circulation (northward above the thermocline) causes a stronger salt transport from the thermocline towards the north than towards the south. It is interesting to note that an increase of E_s amounts to a decrease of the freshwater forcing over the entire Atlantic basin, as the net evaporation from the Atlantic (boxes ts, t and n) is given $(E_s - E_a)$. The thermocline depth decreases in response to the stronger outflow from box t to box n.

Extending the study to the non physical regime $E_s < 0$ (net evaporation in the high latitudes) confirms the role of the AMOC asymmetry; the AMOC can not be collapsed decreasing E_s below some threshold because, as the AMOC weakens, also the impact of E_s on the north–south density difference decreases. The sensitivity of the AMOC thus goes to zero for large enough negative values of E_s (not shown). Similarly, as the value of r_s increases, the sensitivity of q_N to E_s decreases (not shown) as the southern subtropical gyre transports salty waters from box t to box ts regardless of the sense of the overturning circulation.

4.3.2.2 *Asymmetric freshwater flux*

In Fig. 4.6, three bifurcation diagrams computed for different values of η are shown, including D , q_N , q_S and M_{ov} .

As expected, we find that an increase in the freshwater flux E_a leads to a decrease of the AMOC strength. We thus recover the result of [15, 23], that the AMOC strength is controlled by the net evaporation of the overall Atlantic basin. Even if the area where a freshwater anomaly is applied determines quantitative changes in the sensitivity of the AMOC, the sign of this sensitivity is the same as long as the perturbation is applied within the basin. In the framework of our box model, both increasing E_a or decreasing E_s amounts to a reduction of net evaporation out of the Atlantic basin, and both determine a decrease of the AMOC strength. An increase of E_a is, however, much more effective in reducing the AMOC strength than a decrease of E_s , since it changes directly the north–south density difference to which q_N is proportional, and can completely collapse the AMOC, differently from E_s , as discussed in the previous section. The freshwater flux needed to collapse the AMOC is about 0.4 Sv, a value comparable to that used in several “hosing” experiments with models of various complexity (e. g. [50]) and much smaller than the symmetric freshwater flux needed to collapse the J07 model. Even if a similar freshwater flux E_a is used as a “hosing” in the model of J07, the sensitivity in this model is still relatively weak.

In Fig. 4.6, the solution is continued to negative values of q_S , down to the point where the downwelling stops in the north. This implies that, at $q_S = 0$,

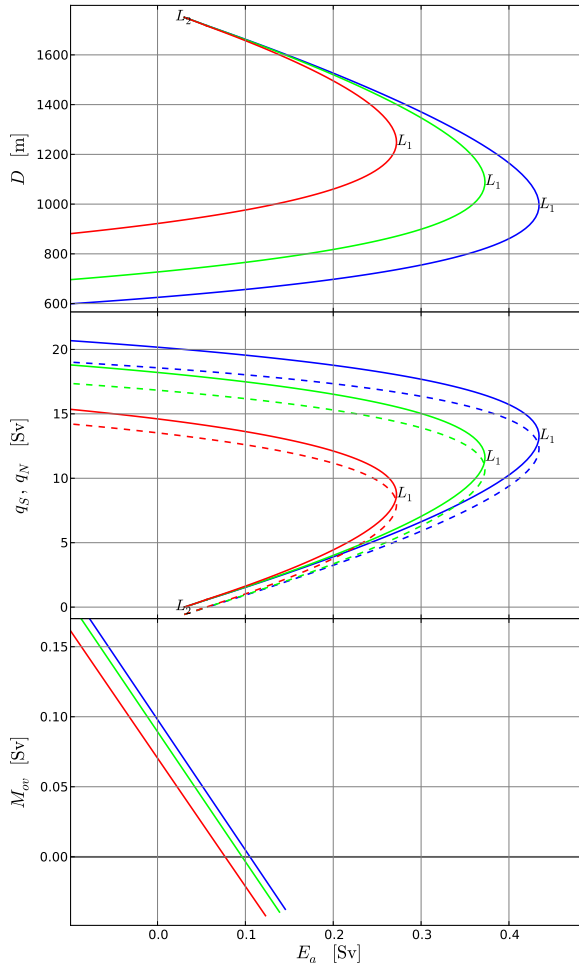


Figure 4.6: Sensitivity of D (top panel, blue), q_S (central panel, dashed), q_N (central panel, full) and M_{OV} (lower panel) to the asymmetric freshwater flux E_a . The different colours (red, green and blue) refer to different η values: $(1.5, 3.0, 4.0) \times 10^4 \text{ m s}^{-1}$ respectively. L_1 marks the position of the saddle node bifurcation ending the ON state of the AMOC. After L_1 , the solution is unstable, and for higher values of E_a only a collapsed state of the AMOC is possible. L_2 marks the position of the saddle node bifurcation ending the OFF state of the AMOC. The plot of M_{OV} stops before the saddle node bifurcations for clarity.

Eqs. (4.3a), (4.3b), (4.3d) and (4.3e) are changed in order to account for the reversal of the advection direction at the boundaries of the boxes s and ts (see Sec. 4.2.2). The continuation to negative q_S , down to the point $q_N = 0$, is performed for discussing the relevance of M_{ov} as a stability indicator (Sec. 4.3.3).

At the point where q_N reaches zero, an increase of the freshwater flux E_a maintains the collapsed state with $q_N = 0$ and a weakly negative q_S compensating the upwelling in the Atlantic, as an increase of E_a decreases ρ_n with respect to ρ_{ts} . On the other hand, if starting from the point where q_N reaches zero the freshwater flux is decreased further, the reversed solution can no longer exist, as a decrease of E_a determines an increase of ρ_n with respect to ρ_{ts} , which must be associated at the steady state with downwelling in the north. We thus conclude that the point defined by $q_N(E_a) = 0$ is the second saddle node bifurcation L_2 of the bifurcation diagram of the AMOC strength of the box model (Fig. 4.1).

4.3.2.3 Sensitivity of AMOC stability to changes in the gyre circulation

We now turn to the assessment of the sensitivity of the collapse position, the saddle node bifurcation L_1 , to changes in the gyre circulation. The position of the saddle node bifurcations of Fig. 4.6 is tracked while r_S or r_N are changed. This enables to compute the critical value of E_a in a range of values of r_S (Fig. 4.7) and r_N (Fig. 4.9), for each value of η used in the bifurcation diagram of Fig. 4.6. The regime diagram obtained divides the parameter plane in two regions: below the critical curve an ON state of the AMOC is possible, while above the line only a collapsed state is present.

Considering first the dependence of L_1 position on r_S (top panel of Fig. 4.7), we see that the asymmetric freshwater flux needed to collapse the AMOC is reduced by an increase of the gyre strength in the south. The decrease with r_S of the freshwater forcing needed for collapsing the AMOC is substantial, and leads almost to the disappearance of the ON state for the highest values of r_S and lowest η . Even if a gyre exchange of 50 Sv or more is unrealistic, the value of M_{az} associated with it (Fig. 4.7, lower panel) is well within the range observed in GCMs [30]. A more effective way of changing M_{az} , i. e. changing the South Atlantic freshwater fluxes, may actually lead to the total disappearance of the ON state for realistic E_a values [15]. Longworth et al. [69], on the other hand, did not observe this behaviour in their box model, finding that the effect of the gyres was always a stabilising one. The difference in results is due to the fact that they only considered the impact of changes in both northern and southern gyres at the same time, in a much more symmetrical configuration (no periodic channel and ACC in the south, boxes of equal sizes in the north and south, and no box ts).

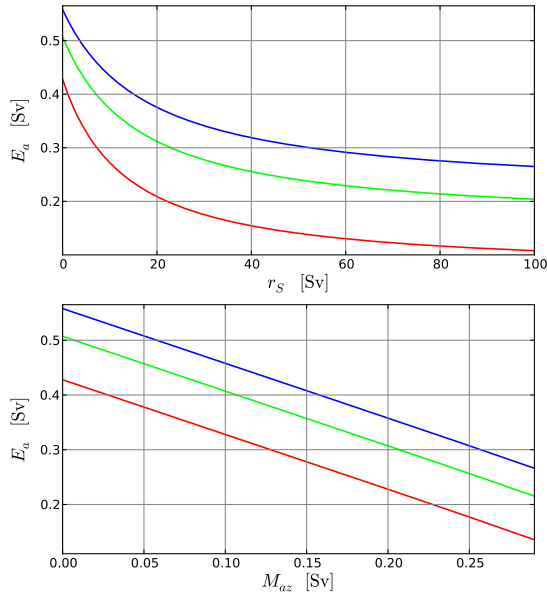


Figure 4.7: Continuation of the limit point L_1 , determining the collapse of the AMOC, (see Fig. 4.6). A stable ON state exists only below the lines, marking the position of L_1 . On the top panel, the continuation in (E_a, r_S) is shown, while in the lower panel the same regime diagram is shown using M_{az} instead of r_S for plotting. The different colours (red, green and blue) refer to different η values: $(1.5, 3.0, 4.5) \times 10^4 \text{ m s}^{-1}$ respectively.

The sensitivity of the position of L_1 can be understood considering the lower panel of Fig. 4.7, where the value of E_a at L_1 is plotted versus M_{az} instead of versus r_S . The loss of stability of the ON state is connected to an increase of the amount of freshwater transported by the southern gyre into the Atlantic basin. This reduces the north–south density difference by increasing the salinity of the box ts and slightly decreasing that of the box t; a smaller E_a is then sufficient to bring $(\rho_n - \rho_{ts})$ to zero, stopping the sinking in the north. We conclude that an increase of M_{az} , in this case obtained by increasing r_S , brings an effective negative density perturbation in the basin. In terms of changes in the bifurcation diagram, we have a shift to the left of the bifurcation diagram and a slight decrease of the width of the ME regime as r_S increases (see Fig. 4.8, top panel).

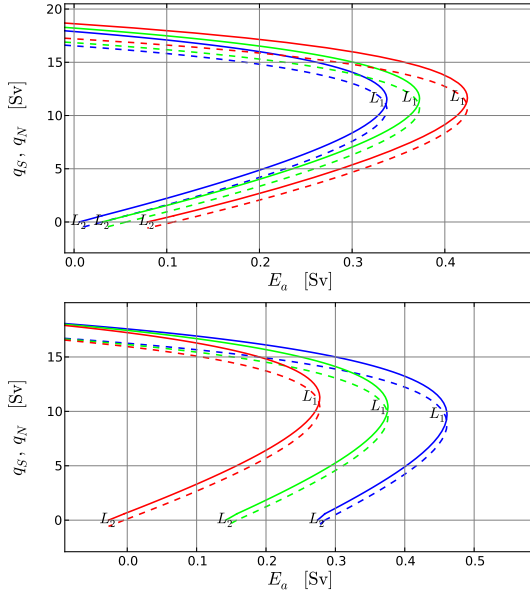


Figure 4.8: Changes in the bifurcation diagram of the AMOC as a function of E_a , as the strength of the gyres are changed; the full (dashed) line refers to q_N (q_S). On the top panel, r_S is changed, while in the lower panel r_N is changed. The different colours (red, green and blue) refer to different r_S or r_N values: 5, 10, 15 Sv respectively. For the case of r_N , the discontinuity in the AMOC strength at the point where $q_S = 0$ is due to the fact the when q_S reverses the sensitivities of the AMOC change abruptly. L_1 and L_2 mark the limit points ending the ON and OFF state respectively.

The impact of the northern gyre on the stability of the AMOC (Fig. 4.9) is opposite to that of the southern gyre. A strengthening of the northern gyre increases the salinity in the northern box, increasing the AMOC strength (not shown) and reducing the sensitivity of the AMOC to freshwater perturbations. This translates into two effects: (i) L_1 moves to higher values of E_a , i. e. a stronger freshwater flux from outside the Atlantic into the n box is necessary to collapse the AMOC and (ii) the collapse of the AMOC takes place at weaker AMOC rates (Fig. 4.9). A strong gyre in the north brings salty waters in the n box independently of the state of the AMOC, and thus reduces on one hand the effectiveness of a freshwater anomaly (L_1 moves to higher E_a), and on the other hand the importance of the salt-advection feedback (L_1 takes place at

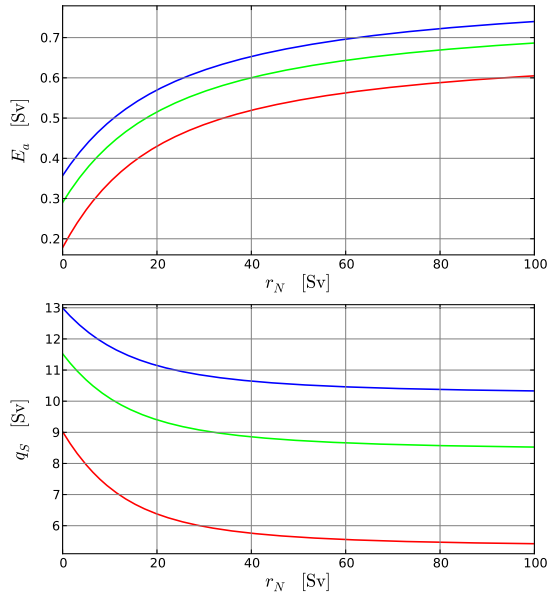


Figure 4.9: Continuation of the limit point L_1 determining the collapse of the AMOC (see Fig. 4.6). A stable ON state exists only below the lines, marking the position of L_1 . On the top panel, the continuation in (E_a, r_N) is shown, while in the lower panel the same regime diagram is shown considering q_S instead of E_a , that is the strength of the flux in the south at the point of collapse. The different colours (red, green and blue) refer to different η values: $(1.5, 3.0, 4.5) \times 10^4 \text{ ms}^{-1}$ respectively.

lower q_S and q_N), as it reduces the relative importance of the salt transport by the AMOC. In connection with the latter point, also the width of the ME regime shrinks markedly (see Fig. 4.8, lower panel). This response to changes in r_N is consistent with what was found by Longworth et al. [69].

4.3.3 The role of M_{ov}

In Fig. 4.6, the bifurcation diagram of M_{ov} as a function of E_a was shown, together with the AMOC strength. M_{ov} monotonically decreases as the freshwater flux in the north is increased until L_1 is reached. A decrease in M_{ov} is thus a robust indication of a reducing distance from the limit point L_1 , where the ON state is no longer stable. It must be kept in mind that all the results pre-

sented here refer to steady state solutions. Changes in M_{ov} are thus differences between different steady states, and not trends in time. The validity of the box-model approach, and that of M_{ov} , far from the steady state is unclear; for this reason we focus on the equilibrium solutions alone.

We can then consider the ME regime, that is the part of the bifurcation diagram between L_1 and the end of the OFF branch, L_2 . In this region, a shut down state of the AMOC is present besides the ON state under the same boundary conditions. As discussed in the introduction, it has been suggested that the change in sign of M_{ov} may mark the entrance into the ME regime, or in other words M_{ov} may change sign at the value of E_a for which L_2 is reached. If $q_N = 0$ is taken as L_2 , we see that M_{ov} is not a perfect indicator of the ME regime, but it gives a good approximation of the ME regime, at least for low values of η .

To analyse this issue in more detail, we study the difference between $E_a|_{q_N}^0$, the value of E_a for which $q_N = 0$ and $E_a|_{M_{ov}}^0$, the value of E_a for which $M_{ov} = 0$ but $q_S, q_N > 0$. The first can be computed considering the system:

$$q_N = 0, \quad (4.6a)$$

$$r_N(S_t - S_n) - (E_s + E_a)S_0 = 0, \quad (4.6b)$$

$$q_{Ek}S_s - q_eS_{ts} - q_S S_t + r_S(S_t - S_{ts}) = 0, \quad (4.6c)$$

$$q_S S_s + q_e S_{ts} - q_{Ek}S_s - (E_s - E_a)S_0 = 0, \quad (4.6d)$$

$$E_s - E_a = M_{ov} + M_{az}, \quad (4.6e)$$

$$q_U + q_S = 0, \quad (4.6f)$$

where the equations represent, in order, the condition of no downwelling in the north, the salt budget of the northern box, the salt budget for the box ts, the salt budget for the box s, the freshwater budget of the Atlantic Ocean (the latter three for the case $q_S < 0$, with $M_{ov} = q_S/S_0(S_d - S_t)$), and the volume budget for the thermocline, all under the condition $q_N = 0$.

From Eq. (4.6f) the thermocline depth at L_2 can be computed; choosing the positive solution of the second order equation we obtain:

$$D|_{q_N}^0 = \frac{1}{2} \frac{L_y}{L_{xA}} \frac{q_{Ek}}{A_{GM}} \left(1 + \sqrt{1 + 4 \frac{L_{xA}}{L_y} \frac{A_{GM} \kappa A}{q_{Ek}^2}} \right), \quad (4.7)$$

where we write the value of D at L_2 as $D|_{q_N}^0$, and the Ekman inflow into the thermocline, $q_{Ek} = (\tau L_{xS}) / (\rho_0 |f_S|)$, is left implicit. Eliminating S_t, S_{ts}, S_s, S_d

and S_n from Eqs. (4.6a)– (4.6e) and using Eq. (4.7), an expression for $E_a|_{q_N}^0$ can be obtained:

$$E_a|_{q_N}^0 = E_s \frac{r_N q_{Ek} - q_e|_{q_N}^0 (q_e|_{q_N}^0 - q_{Ek} + r_S)}{r_N q_{Ek} + q_e|_{q_N}^0 (q_e|_{q_N}^0 - q_{Ek} + r_S)} + r_N \frac{\Delta T \alpha}{S_0 \beta} \frac{q_e|_{q_N}^0 (q_e|_{q_N}^0 - q_{Ek} + r_S)}{r_N q_{Ek} + q_e|_{q_N}^0 (q_e|_{q_N}^0 - q_{Ek} + r_S)}, \quad (4.8)$$

where $q_e|_{q_N}^0$ represents the value of the eddy flux at the point where $q_N = 0$ and $\Delta T = T_{ts} - T_n$. $E_a|_{q_N}^0$ does not depend on η , as confirmed by the numerical results in Fig. 4.6. It is interesting to compute the limit of $E_a|_{q_N}^0$ for r_S and κ going to zero. From Eq. (4.7), we find that:

$$\lim_{\kappa \rightarrow 0} D|_{q_N}^0 = \frac{L_y}{L_{xA}} \frac{q_{Ek}}{A_{GM}},$$

which simply states that if κ goes to zero, $q_{Ek} = q_e$ if $q_N = 0$, since also q_S must be zero. The non diffusive version of Eq. (4.8) is then easily obtained:

$$\lim_{\kappa \rightarrow 0} E_a|_{q_N}^0 = E_s \frac{r_N - r_S}{r_N + r_S} + \frac{\Delta T \alpha}{S_0 \beta} \frac{r_N r_S}{r_N + r_S}, \quad (4.9)$$

from which the $r_S \rightarrow 0$ limit of $E_a|_{q_N}^0$ can be computed:

$$\lim_{\kappa, r_S \rightarrow 0} E_a|_{q_N}^0 = E_s,$$

this shows that the OFF solution ends at the point where net evaporation over the Atlantic basin sums up to zero ($E_a = E_s$), if no vertical diffusion or gyre transport in the south are present: no OFF state is available for values of E_a lower than E_s . It is interesting to note that the presence of r_N is irrelevant in this limit, i. e. the redistribution of freshwater within the Atlantic basin is irrelevant. This limiting behaviour is the one discussed in Rahmstorf [86].

Similarly, the value of E_a associated with $M_{ov} = 0$, shorthanded $E_a|_{M_{ov}}^0$, can be obtained solving the system:

$$S_{ts} = S_n \quad (4.10a)$$

$$q_N (S_t - S_n) + r_N (S_t - S_n) - (E_s + E_a) S_0 = 0 \quad (4.10b)$$

$$q_{Ek} S_s - q_e S_{ts} - q_S S_{ts} + r_S (S_t - S_{ts}) = 0 \quad (4.10c)$$

$$q_S S_n + q_e S_{ts} - q_{Ek} S_s - (E_s - E_a) S_0 = 0 \quad (4.10d)$$

$$q_S - q_N + q_U = 0 \quad (4.10e)$$

where the first equation is the condition for $M_{ov} = 0$ if $q_S > 0$, the second is the salt budget for the northern box, the third is the salt budget for the ts box, the fourth is the salt budget for the s box (with $S_d = S_n$, as $q_S > 0$) and the last equation is the volume budget of the thermocline. The algebra is in this case more tedious, but an expression for $E_a|_{M_{ov}}^0$ can be obtained similarly to what done for $E_a|_{q_N}^0$, exploiting Mathematica software [122] (see Appendix B). The skill of M_{ov} as an indicator of ME can then be measured as

$$\Delta_E = E_a|_{q_N}^0 - E_a|_{M_{ov}}^0.$$

The analytical expression obtained for Δ_E and $E_a|_{M_{ov}}^0$ are very long, so that they are reported in the Appendix B. The expression of Δ_E in the limit $\kappa \rightarrow 0$ reads:

$$\lim_{\kappa \rightarrow 0} \Delta_E = \frac{r_S}{r_N + r_S} \times \left(r_N \frac{\Delta T \alpha}{S_0 \beta} - 2E_s \times \frac{q_{Ek} \Delta T \alpha \eta + \frac{1}{2} \left(\frac{A_{GM} L_{xA}}{L_y} \right)^2 \left(1 - \sqrt{1 + 4 \left(\frac{L_y}{A_{GM} L_{xA}} \right)^2 q_{Ek} \Delta T \alpha \eta} \right)}{\left[(q_{Ek} + r_N + r_S) \Delta T \alpha \eta + \frac{1}{2} \left(\frac{A_{GM} L_{xA}}{L_y} \right)^2 \left(1 - \sqrt{1 + 4 \left(\frac{L_y}{A_{GM} L_{xA}} \right)^2 q_{Ek} \Delta T \alpha \eta} \right) \right]} \right), \quad (4.11)$$

from which it trivially follows that $\Delta_E \rightarrow 0$ if also $r_S \rightarrow 0$. We thus obtain the important result:

$$\lim_{r_S, \kappa \rightarrow 0} \Delta_E = 0, \quad (4.12)$$

recovering the result of the simpler model of Rahmstorf [86]. Indeed, M_{ov} is a perfect indicator of ME if the response of diffusive upwelling and southern gyre transport to AMOC changes are neglected. From Eq. (4.12) we can expect M_{ov} to be a good indicator of the ME regime as long as feedback mechanisms other than the salt-advection feedback, which is measured by M_{ov} , do not play a relevant role. In particular, vertical diffusion and the freshwater transport by the gyre circulation (or by diffusion) at the southern border of the thermocline must not provide an effective feedback mechanism to changes in the AMOC, which in the simple framework of the box model is the limit $\kappa, r_S \rightarrow 0$. In the limit of no vertical diffusion and no gyre in the south, other mechanisms are irrelevant to the skill of M_{ov} as an indicator of ME.

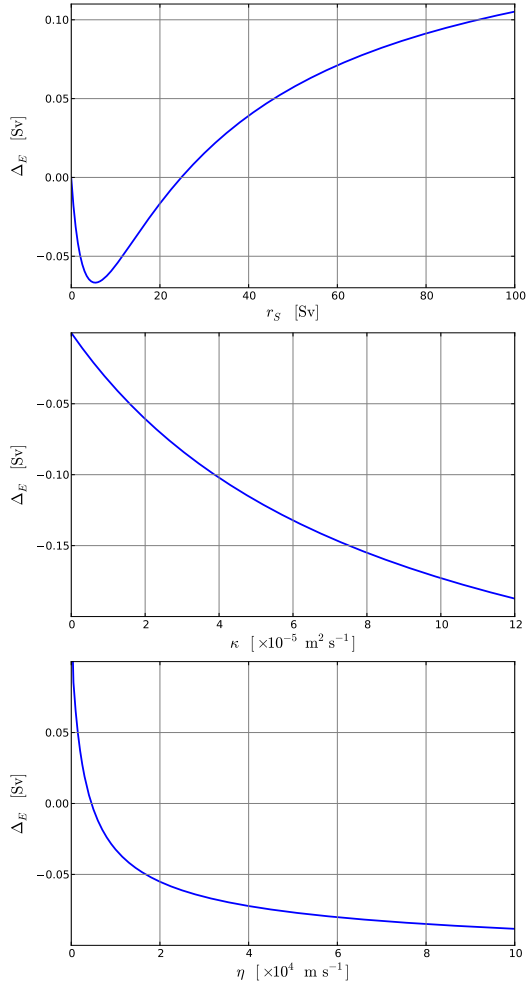


Figure 4.10: Dependence of Δ_E on r_S (top), κ (centre) and η (bottom). Δ_E is shown on the top (centre) panel as a function $r_S(\kappa)$, keeping $\kappa = 0 \text{ m}^2 \text{ s}^{-1}$ ($r_S = 0 \text{ Sv}$); all other parameters are kept at the reference value of Tab. 4.1. In the bottom panel, Δ_E is shown as a function of η with all other parameters as in Tab. 4.1.

In Fig. 4.10, the dependency of Δ_E on r_S , κ and η are shown (from top to bottom). The top panel shows the dependency of Δ_E on r_S in the non-diffusive limit $\kappa \rightarrow 0$ and the centre panel that of Δ_E on κ in the limit of $r_S \rightarrow 0$. In the case of the southern gyre, Δ_E first grows towards negative values, reaching a minimum at about 5 Sv to increase again and reach positive values for higher r_S values. An increase in r_S has two effects: (i) it increases M_{az} and consequently decreases M_{ov} (see Fig. 4.4, bottom), making $E_a|_{M_{ov}}^0$ smaller, and (ii) it shifts L_2 to lower values of E_a (see Fig. 4.8, top). The first change depends on how effective r_S is in increasing M_{az} , and from Fig. 4.4 it is clear that M_{az} increases quickly for low r_S , but then saturates for larger values of r_S , as the salinity difference between boxes t and ts decreases. The value of $E_a|_{q_N}^0$ decreases faster than $E_a|_{M_{ov}}^0$ at small r_S , but then saturates as well being almost constant above $r_S \approx 30$ Sv. For this reason, at first the shift of $E_a|_{q_N}^0$ dominates, but as r_S increases the change in $E_a|_{M_{ov}}^0$ becomes more important, and thus Δ_E crosses zero a second time for $r_S \approx 25$ Sv, and is positive afterwards. This second zero will move to higher values of r_S as κ increases, marking the position where the effects of r_S and κ compensate each other (not shown). The values of the shift are always relatively small in magnitude (< 0.05 Sv), as long as r_S is not unrealistically large.

The dependency of Δ_E on κ indicates that an increased vertical diffusion does not affect M_{ov} , but shifts L_2 towards more negative values of E_a , by stabilising the OFF state of the AMOC and widening the ME regime. This translates into the shift of Δ_E towards negative values as κ increases, as seen in Fig. 4.10. This stabilising effect of vertical mixing within the Atlantic basin for the OFF state was already recognised by Sijp and England [94]. In their study, they could not reach any permanently reversed state below a critical value of vertical diffusivity within the Atlantic basin. This is not the case in our study. This discrepancy is likely due to the use of perturbations too small to push the system to the OFF state with low diffusivity values in the work by Sijp and England [94]. Considering the values of vertical diffusion used in most numerical models ($\mathcal{O}(10^{-4} \text{ m}^2 \text{ s}^{-1})$), we may expect the skill of M_{ov} in identifying the ME regime to be often low. The fact that M_{ov} has been instead successfully used to identify the ME regime in different numerical models (e. g. [21, 50, 54]) is a sign that a compensation between the effects of vertical diffusion and horizontal advection (and/or diffusion) is taking place in numerical models.

When η is increased, Δ_E goes from positive to negative values, if r_S , κ or both are greater than zero (Fig. 4.10, bottom). This is due to the proportionality between M_{ov} and the AMOC strength: increasing the hydraulic constant η will increase M_{ov} , requiring a higher E_a for bringing it to zero, while the L_2 position is independent of η (Eq. (4.8)). Δ_E is always smaller than 0.1 Sv if η is taken in a range giving AMOC rates not too far from reality

($\eta \approx 2 - 6 \times 10^4 \text{ m s}^{-1}$). If the gyre in the south and vertical diffusion are both set to zero, Δ_E is identically zero independently of η , as discussed above.

4.4 SUMMARY AND CONCLUSIONS

A box model for the AMOC was developed, focusing on the effect of the exchanges between the Atlantic Ocean and Southern Oceans on the stability of the Atlantic AMOC. The model includes a shallow box of variable depth, providing a basic representation of the Atlantic thermocline depth dynamics in the tropics and subtropics, similarly to what was done in [42] and J07. The thermocline depth is set by a balance between inflow from the Southern Ocean due to Ekman pumping, outflow due to baroclinic activity near the southern subpolar front, upwelling at low latitudes due to vertical diffusion and downwelling at the high northern latitudes. Differently from previous studies, the scaling for the downwelling flux in the north depends on the density difference between the northern North Atlantic and the region above the thermocline north of the ACC, which is represented by a separate box. Furthermore, the transport (of salinity) between the ACC and the Atlantic is treated in a different way than in earlier studies: Ekman inflow and eddy outflow are considered separately for what concerns their associated salt transport.

Similarly to what obtained in J07 and Gnanadesikan [42], this configuration produces an inter-hemispheric AMOC only if sufficiently strong wind stress is acting over the Southern Ocean. The AMOC is, however, still buoyancy controlled, as changes in the north–south density difference, determined in the model only by changes in freshwater forcing or transport, can collapse the AMOC. The main advance with respect to previous works, is the ability to reproduce the sensitivity of the AMOC to changes in the freshwater transport by the southern subtropical gyre in the Atlantic Ocean. These results point to the fundamental importance of the region south of the tip of Africa and north of the ACC in determining the AMOC stability.

In particular, the freshwater transport at the latitude of the southern tip of Africa, by either the overturning or the azonal circulation, can change completely the response of the AMOC to perturbations in the surface freshwater flux. In this view, the net freshwater import into the Atlantic basin by the meridional overturning circulation, M_{ov} , is playing a fundamental role, being associated with the growth of perturbations due to the salt-advection feedback. If the salt-advection feedback is the dominant feedback connected with a AMOC collapse, the sign of M_{ov} completely determines whether a permanent collapse is possible. If other responses are important (gyre circulation, vertical diffusivity, atmospheric feedbacks or others not considered in this paper), the sign of M_{ov} will not be a perfect indicator of multiple steady states anymore, its skill

being dependent on the strength of the salt-advection feedback in comparison with other responses. For a parameter set representative of the real ocean, we can expect M_{ov} to be well below 0.1 Sv when entering the ME regime. Considering the effect of noise and internal variability, this difference from zero is unlikely to be important. On the other hand, if vertical diffusion is providing a strong feedback during a AMOC collapse (in particular in numerical ocean models with high vertical diffusivity—both physical and numerical) the skill of M_{ov} as indicator of ME may be reduced. The observation that M_{ov} actually is a good indicator in different numerical models [21, 50, 54], suggests that a compensating mechanism between different feedbacks is operating, in particular between the response due to vertical diffusivity and horizontal advection by the southern subtropical gyre. Apart from its sign, a downward trend in M_{ov} in response to a slowly varying external forcing³ is a robust signal of an approach to the collapse point of the AMOC, independently of the source of the freshwater perturbation (i. e. any term of the freshwater budget Eq. (4.4)).

The box model enables to speculate on the importance of the latitude at which M_{ov} is computed: “Why thirty degrees south?” or, in other words, why should M_{ov} be computed at the southern edge of the Atlantic Ocean? One hypothesis is that the latitude of the southern tip of Africa marks the point north of which the AMOC can be considered as a coherent flow with approximately constant water properties in numerical models. Southward of this latitude and down to the northern end of the ACC, the interaction between the Ekman inflow from the Southern Ocean and the salt transport from the north by the subtropical gyre determines the density of the waters that flow into the Atlantic basin. North of this point, salinity anomalies entering the Atlantic Ocean will eventually be advected to the northern downwelling regions where they will translate to a AMOC strength anomaly (neglecting feedbacks other than the salt-advection feedback). Whether these anomalies are subject to a positive feedback loop or a negative one depends on the sign of the freshwater transport at the southern entrance of the basin. A second hypothesis, possibly related to the first one, concerns the presence of zonal boundaries north of the southern tip of Africa, which can support a zonal pressure gradient across the basin, controlling the AMOC strength through planetary geostrophic balance [11]. Changes in this region may affect the entire basin, setting the boundary conditions for the AMOC within the basin.

We have demonstrated that the box model is a useful diagnostic tool to understand results from GCMs, and that M_{ov} can be a good indicator of the stability of the AMOC, but one may ask if these results are relevant to interpret the results from high-resolution GCMs and, more importantly, observations from the real ocean. In order for our conclusions to hold in those cases as well, the main

³ That is, changes slow enough to leave the system close to the steady state.

assumption that must be satisfied is that the meridional overturning circulation should have a meridionally coherent response to freshwater perturbations on long time scales, at least within the Atlantic basin. Finally, even if the role of meridional density gradients in driving the AMOC is corroborated by various studies (see e. g. [75, 95]), the relevance of the scaling for the downwelling flux in an eddying ocean with complex geometry is still to be demonstrated. While the downwelling in the subpolar gyre seems to be well described by the theory of Spall [97], the connection between the downwelling in the subpolar gyre and the overturning circulation and its scaling law on the global scale is still unclear.

5

RECONCILING THE NORTH–SOUTH DENSITY DIFFERENCE SCALING FOR THE MERIDIONAL OVERTURNING CIRCULATION STRENGTH WITH GEOSTROPHY.

A scaling for the Meridional Overturning Circulation (MOC) strength depending on the north–south density difference, as the one used in Chap. 4, is discussed. A short review of the issue is done, with a focus on the links to pycnocline structure theory. An argument supporting a view of the MOC strength scaling with north–south density difference is proposed and numerical evidence supporting this hypothesis is presented.

5.1 INTRODUCTION

In the classical view of Stommel [99], the Meridional Overturning Circulation (MOC) is considered as an example of “horizontal convection” in a non-rotating fluid. In other words, the MOC is treated as a two dimensional overturning circulation where the horizontal scale is much larger than the vertical one, and where rotational effects can be neglected. The strength of the MOC is often measured by the maximum of the MOC streamfunction, defined by:

$$\Psi = \text{Max} \left[- \int_{-H}^z \int_W^E v \, dx \, dz' \right],$$

where v is the meridional velocity and the inner (definite) integration is performed from the western to the eastern boundary and the outer (indefinite) from the bottom, at depth $-H$, to the generic depth z . If horizontal convection is considered, Ψ is proportional to a power of the applied surface buoyancy restoring [53].

When rotational effects are included, the thermal wind relation is essential for diagnosing the MOC strength:

$$\frac{\partial v}{\partial z} = \frac{1}{f} \frac{\partial b}{\partial x}, \tag{5.1}$$

with f the Coriolis parameter and $b = -g\Delta\rho/\rho$ the buoyancy.

Thermal wind balance underlies in particular the scaling relationship between MOC strength and vertical diffusivity [see e.g. 26, 71, 85, and references therein]. Thermal wind balance underlies also the scaling used in the works of Gnanadesikan [42] and Johnson et al. [57], and derived in Johnson and Marshall [56] in a two layer model:

$$\Psi \sim \frac{1}{f} \Delta b_z D_E^2, \tag{5.2}$$

where by f we mean here a characteristic Coriolis parameter at the latitude of the MOC maximum, Δb_z is the buoyancy difference between the upper and lower branches of the MOC and D_E is the pycnocline depth at the eastern boundary at the same latitude where the pycnocline outcrops in the western boundary. This scaling can be derived by integrating thermal wind balance in a two layer ocean, assuming that the maximum of the MOC is achieved at the latitude where the pycnocline is outcropping in the western boundary.

For a closed basin extending over one hemisphere, various authors noted that the overturning rate would scale as [see e.g. 71]

$$\Psi \sim \frac{1}{f} \Delta b_{TP} D^2, \tag{5.3}$$

where D is a depth scale, set in Marotzke [71] by an advective–diffusive balance and representing the pycnocline depth. The buoyancy difference Δb_{TP} is measured at the surface, between the tropical and polar ends of the basin considered. The implicit assumption of this scaling is that the scales of zonal and meridional velocity are linearly related [85], allowing to use the meridional instead of the zonal density gradient.

The extension of a similar scaling, based on meridional density differences, for an inter-hemispheric overturning circulation is not straightforward but is supported by the numerical results of Marotzke and Klinger [72], Weijer et al. [118] and Levermann and Fürst [67], who consider the correlation between MOC strength and meridional density (or pressure) gradient. De Boer et al. [20] discussed the limits of this approach, finding that the depth scale that should be used in the scaling is the depth of the maximum of the overturning streamfunction, rather than the depth of the pycnocline. One of the main limits to the use of the scaling (5.3) for inter-hemispheric overturning is that geostrophy is not valid at the equator, and no well established theory for the overturning circulation at low latitudes exists at the moment.

On physical grounds, the scaling (5.3) suggests that a meridional density gradient causes a meridional pressure gradient, which in turn drives a circulation on the meridional plane. Such a mechanism can function only in the western boundary, where geostrophy can be overcome, and velocity can be aligned to the pressure gradient [46, 75, 118]. A similar view is put forward by Sijp et al. [95], where the MOC strength is linked to the meridional slope of the isopycnal separating upper and lower MOC branches in the tropical western boundary. The connection between the meridional density gradient and the MOC is analysed using the concept of available potential energy also by Tailleux [104].

Even if such an interpretation is valid, and the MOC driven by meridional pressure gradients in the western boundary, the MOC must still be in geostrophic balance on the basin scale, so the thermal wind relationship (5.1) still gives a valid scaling:

$$\Psi \sim \frac{1}{f} \Delta b_{EW} h^2, \quad (5.4)$$

where Δb_{EW} is the buoyancy difference between the eastern and the western boundary, and h is a depth scale. Both are measured at the position of the maximum of the MOC streamfunction.

The scaling used in Chap. 4 can be written as:

$$\Psi \sim \frac{1}{f} \Delta b_{SN} h^2, \quad (5.5)$$

where the relevant buoyancy difference is assumed to be the one between the region at the northern end of the Antarctic Circumpolar Current (ACC), where

Antarctic Intermediate Water forms, and the dense water formation regions in the North Atlantic. Is this latter scaling consistent with the others and, moreover, how can this be reconciled with geostrophy?

5.2 SCALING OF THE AMOC WITH NORTH–SOUTH DENSITY DIFFERENCE

Large numerical and observational evidence shows that the geostrophic approximation is a good diagnostic of the large scale motions of the ocean in general, and of the Atlantic Meridional Overturning Circulation (AMOC) in particular [see e.g. 14, 18, 49, 72, 123]. In fact, even boundary currents may be in geostrophic balance, even if only in the along boundary direction [14]. We thus expect the scaling (5.4) to hold, as long as the buoyancy difference and the depth scale are measured at the latitude and depth of the MOC maximum. The MOC maximum should then be determined by a balance between the maximum east–west density difference and the depth at which this maximum is reached. The density structure of the ocean has to be taken into account too. The upper ocean (generically referred to as the “pycnocline”) has relatively high buoyancy frequency. The deeper ocean has lower buoyancy frequency and is much denser than the upper ocean, being filled with dense water formed in the subpolar regions. The upper and intermediate ocean are separated by a local maximum of buoyancy frequency, the global one being close to the surface. The lower boundary of the pycnocline slopes down to the east at the latitudes where the subtropical and subpolar gyres meet in the Northern Hemisphere (NH) (around θ_b in Fig. 5.1), as the pycnocline shoals in the west colliding with the southward flowing deep western boundary current. The maximum of the MOC is likely to be associated with the strong buoyancy difference between the lowest part of the pycnocline and the water masses just below it. If this is the case, the MOC maximum is in thermal wind balance with the buoyancy difference between the lower pycnocline in the east, and the upper deep western boundary current in the west, as represented in Fig. 5.1.

A link between the zonal density difference and the north–south density difference can be made by considering the structure of the pycnocline in a basin with a periodic channel at its southern end. In the SH, the outcropping latitude of the pycnocline tends to be locked at the northern end of the periodic channel [111]. This outcropping latitude is marked in Fig. 5.1 by θ_o . In the real ocean, this is the formation region of the Antarctic Intermediate Water, east of the southernmost part of the American continent. In an enclosed basin, the basin-scale gyre circulation is very efficient in flattening the isopycnals below the mixed layer. On the other hand, in the periodic channel, no meridional flow

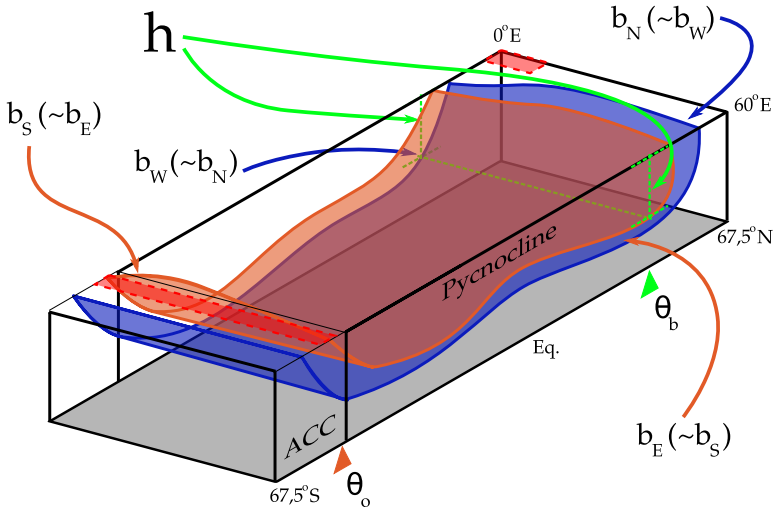


Figure 5.1: Idealised perspective view of the two surfaces of constant buoyancy involved in the scaling, $b_N \sim b_W$ and $b_S \sim b_E$, in a closed basin with a periodic channel at its southern end (ACC). The depth h and the latitude where the MOC reaches its maximum are shown by the green dashed lines. The green triangle and θ_b mark the latitude where b_S reaches its maximum depth at the eastern boundary. The red triangle and θ_0 mark the latitude where the pycnocline outcrops in the SH. The pycnocline, above the upper isopycnal drawn in the figure, is marked, as well as the periodic channel in the south, representing the ACC. The red dashed boxes mark the regions where the estimates of b_N and b_S are measured in the numerical model. The latitudes and longitudes in the drawing refer to the numerical model used.

can be supported in geostrophic balance and isopycnals have a steeper slope.¹ This different mapping of surface buoyancy onto vertical stratification, in the zonally enclosed basin and in the zonally periodic channel, is reflected on the lower buoyancy frequency of the waters outcropping south of θ_0 (see Fig. 5.2). The density class outcropping at the northern end of the periodic channel then becomes a natural choice for the lower boundary of the pycnocline, since this isopycnal separates lighter, more stratified waters above from colder, less stratified waters below. This is true even in presence of finite vertical diffusivity, as long as stratification does not become completely dominated by diabatic effects [111].

¹ In the periodic channel, the isopycnal slope is set by a balance between northern Ekman transport and southward eddy flow, as discussed in Chap. 4.

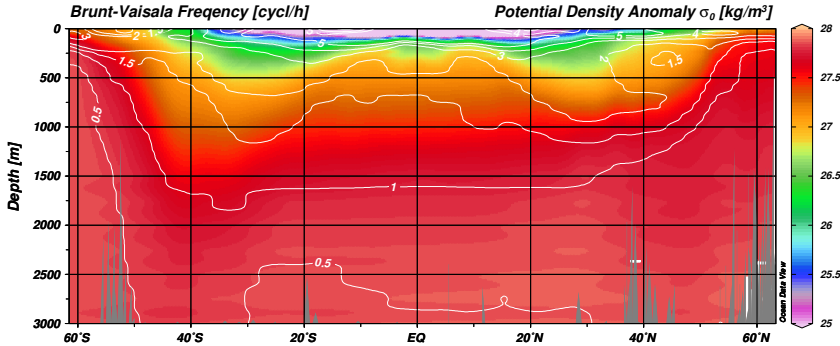


Figure 5.2: A section of potential density anomaly (shaded, referred to 0 db) and buoyancy frequency (white contours), averaged over the central Atlantic and the Atlantic sector of the Southern Ocean. The slope of outcropping isopycnals in the SH increases while moving southward, since the gyre in a zonally enclosed basin (north of approximately 35°S) is more effective in flattening the isopycnal slope than eddies. More to the south, eddies are on the other hand essential, due to the lack of zonal boundaries which makes meridional flow in geostrophic balance impossible. Buoyancy frequency decreases markedly approximately below the 27 kg m⁻³ isopycnal; heavier waters start outcropping in the ACC. Data from Gouretski and Koltermann [44].

If the above discussion holds, the highest buoyancy in the scaling (5.4), i. e. b_E , is in fact set in the SH, by the lightest water upwelling at the northern end of the periodic channel, or can at least be identified by measuring buoyancy in this region (so $b_E \sim b_S$). This is true as long as the circulation in the periodic channel is the main upwelling path for deep water or, in other words, as long as vertical diffusion is not the primary element setting stratification in the ocean interior.

Assuming, as is the case for the real ocean, that the surface buoyancy in the SH reaches lower values than in the NH, all the density classes formed in the NH can be upwelled in the periodic channel by Ekman pumping. We thus expect the lowest buoyancy involved in the scaling, b_W , to be limited by the dense water formation in the NH. The buoyancy at the western boundary, b_W , is thus a buoyancy representative of the sources of the deep western boundary current (and $b_W = b_N$).

In the limit of an adiabatic overturning circulation (with a vanishing value of vertical diffusivity), Wolfe and Cessi [120] argued that the scaling (5.4) can be rewritten using Δb_c instead of Δb_{EW} . The former is the buoyancy interval measured by the surface density classes shared between the periodic channel

(the Drake passage) where the ACC flows and the dense water formation regions in the North Atlantic, which feed the lower branch of the MOC. This can be linked to our hypothesis, noting again that Δb_c is limited by dense water formation in the north, and by the pycnocline upwelling in the south.

From this discussion, a rationale emerges for choosing the scaling (5.5), equivalent to the one used in Chap. 4. If the MOC is in thermal wind balance with the buoyancy difference between the deep western boundary current (in the west) and the lower part of the pycnocline (in the east), then the buoyancy at the eastern boundary will in fact be controlled to a large extent by the stratification in the periodic channel, in the SH.

This is evocative of the work of Spall and Pickart [98], which shows how the downwelling in a subpolar basin is related to thermal wind at the entrance of the basin. Spall and Pickart [98] demonstrated in particular that the contrast between the warm water source, flowing northward in the eastern boundary, and the deep boundary current in the west, are in balance with the downwelling within the basin. In the subpolar gyre, a north–south surface buoyancy gradient is thus projected into an east–west buoyancy gradient at depth, similarly to what suggested here for the basin-scale MOC.

To test this conjecture, we use an idealised numerical model, where a series of different boundary conditions can be imposed, evaluating the correlation between the scaling (5.5) and the strength of the MOC.

5.3 METHODS

The hypothesis discussed in the previous section can be tested with a set of numerical experiments. With this aim, a model was set up using the Massachusetts Institute of Technology General Circulation Model (MITgcm) [76], with a closed interhemispheric basin centred at the equator. The domain extends over 60° in longitude, 135° in latitude and 4500 m in depth. A zonally periodic channel, 3000 m deep and 16° wide in the meridional direction, is added at the southern end of the basin. The resolution of the model is 1.35° in the meridional direction and 1.5° in the zonal direction, while 20 layers are used in the vertical, with cell thickness ranging from 10 m at the top to 530 m at the bottom. Only temperature, and no salinity, is used in the model and a linear equation of state. Scale dependent Laplacian viscosity is used, and no explicit horizontal diffusion is imposed. An isopycnal diffusivity of $300 \text{ m}^2 \text{ s}^{-1}$ is used with the Gent and McWilliams [39] parametrization. Temperature is advected by the scheme of Daru and Tenaud [19] (advection scheme 7 in MITgcm), which reduces the amount of spurious numerical diffusion in the model. This configuration is a highly idealised representation of the Atlantic Ocean with the Southern Ocean and the ACC at its southern end. The model is forced

Name	SH wind [Pa]	T north [°C]	T max [°C]	T south [°C]	Vert. diff. [$\text{m}^2 \text{s}^{-1}$]
A	0.1	0.5	18.0	-0.5	$1.0 \cdot 10^{-5}$
B	0.15	0.5	18.0	-0.5	$1.0 \cdot 10^{-5}$
C	0.055	0.5	18.0	-0.5	$1.0 \cdot 10^{-5}$
D	0.1	0.5	18.0	-1.5	$1.0 \cdot 10^{-5}$
E	0.1	0.5	18.0	0.5	$1.0 \cdot 10^{-5}$
F	0.1	0.5	21.0	-0.5	$1.0 \cdot 10^{-5}$
G	0.2	0.5	18.0	-0.5	$1.0 \cdot 10^{-5}$
H	0.1	0.5	18.0	-0.5	$5.0 \cdot 10^{-5}$
I	0.1	0.5	18.0	-1.5	$5.0 \cdot 10^{-5}$
J	0.055	0.5	18.0	-0.5	$5.0 \cdot 10^{-5}$
K	0.1	0.5	21.0	-0.5	$5.0 \cdot 10^{-5}$
L	0.2	0.5	18.0	-0.5	$5.0 \cdot 10^{-5}$
M	0.1	0.5	18.0	-0.5	$1.0 \cdot 10^{-4}$

Table 5.1: Summary of the numerical experiments performed. From left to right, the table reports the name of the experiment, the maximum wind stress in the SH (westerlies), the restoring temperature at the northern end of the basin, the maximum restoring temperature (at or close to the equator), the restoring temperature at the southern end of the basin and the value of vertical diffusivity in the ocean interior.

at the surface by fixed winds and by restoring temperature to a fixed profile on a monthly time scale. The standard profiles of wind stress and restoring temperature are shown in Fig. 5.3. The experiments performed are summarised in Tab. 5.1. By considering the values in the table, the forcing profiles of the various configurations can be identified in the figure. Parameters that are changed are the strength of the westerlies in the SH, the temperature profile in the SH or in the low and mid latitudes, and vertical diffusivity. In all experiments, the value of vertical diffusivity in the interior, listed in the last column of Tab. 5.1, increases in the upper 50 m to reach $5.0 \cdot 10^{-3} \text{ m}^2 \text{ s}^{-1}$. All the experiments are performed by spinning up the model from rest for 5000 years with an asynchronous time stepping, to establish a preliminary stratification. The model is then run for 500 years more with the same time step for momentum and temperature, and the quantities discussed here refer to the last 50 years of integration. Even if the temperature in the deep ocean still shows a residual trend at the end of the simulations, no trends in the quantities considered here are seen. Some configurations have been run for 100 years more, but the results are unchanged.

To evaluate the skill of the scaling, a definition of the temperature difference to be used in (5.5) has to be chosen (since no salinity is included in the model, we can treat temperature equivalently to buoyancy). The northern temperature, b_N , is defined as the zonal average surface temperature at the northernmost latitude, west of 15°E (see Fig. 5.1). The results are not very sensitive to this particular choice; this particular definition is used since the highest surface density are reached in the model in the north-western corner of the domain. The southern temperature, b_S , is defined as the zonal mean surface temperature at a latitude of 50°S , at the northern end of the periodic channel. The southern temperature may be estimated also by averaging over a latitudinal interval, but by taking the zonal average at a single latitude we want to stress the fact the MOC strength is governed by the properties in a narrow region, at the bottom of the pycnocline and at its outcropping latitude. The depth scale can be measured as the maximum depth reached by the southern temperature on the eastern boundary in the NH. For reasons that will be clarified in the next section, the MOC maximum is measured south of the latitude where this maximum depth is reached.

5.4 RESULTS

A zonally averaged picture of potential temperature in run A is shown in Fig. 5.4. Taking the southern temperature (5.7°C in the case of run A shown in the figure) as the lower boundary of the pycnocline, the pycnocline depth is

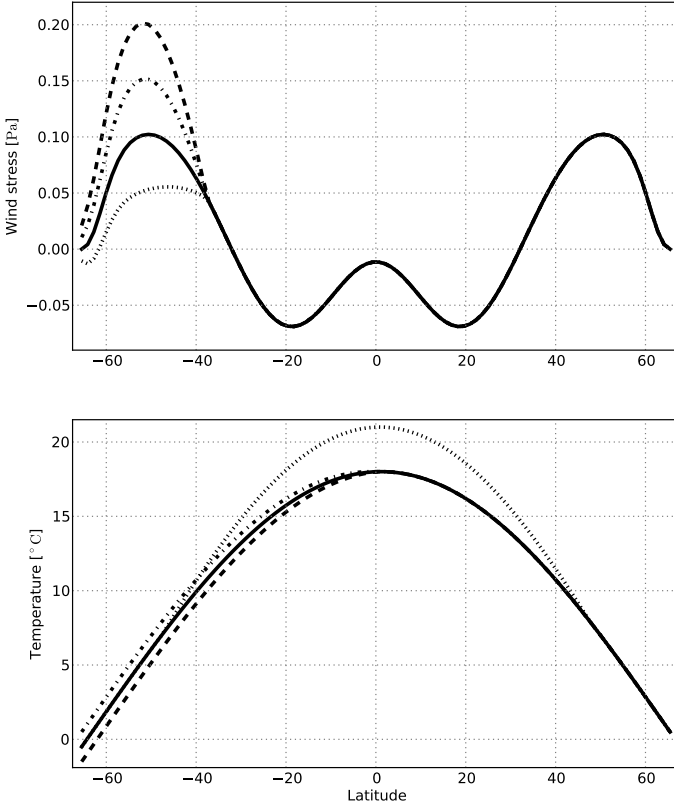


Figure 5.3: Forcing profiles for wind stress (top) and temperature (bottom), the different line styles refer to different experiments (see text and Tab. 5.1). The strength of the SH westerlies alone is changed, while temperature is changed only over the SH or in the tropics and subtropics (dotted line, run F). As an example, full lines in both panels give the forcing of run A, the dashed dotted line for wind and full line for temperature gives the forcing for run B.

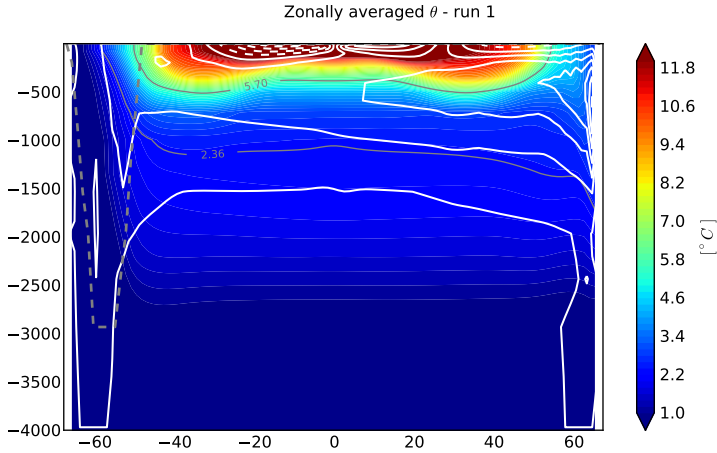


Figure 5.4: The filled contours show the zonally averaged potential temperature of run A, computed as an average over years 5, 450-5,500 of the simulation (the last 50 years of the simulation). The two continuous grey lines show the isotherms of the “northern” and “southern” temperature used in the scaling, 2.36°C and 5.7°C respectively (see text). The white lines show the MOC streamfunction: the contour interval is 2 Sv, with continuous contours being positive values (zero included) and dashed contours being negative. The dashed grey line marks the depth of the periodic channel in the SH.

underestimated with respect to the real ocean, and the MOC is rather shallow as well. In the model, the pycnocline depth is close to 500 m while in the real ocean, looking at Fig. 5.2, it is closer to 700 m. This can be expected from the fact that the periodic channel in the south has a zonal width of only $1/3$ of the real world, with a proportionally smaller Ekman pumping and a consequently shallower pycnocline depth [2]. In Fig. 5.4, the overall stratification discussed in Sec. 5.2 can be observed. Even if the details vary in the different simulations, the general picture is similar in all simulations. Stratification in the pycnocline, within the zonally enclosed part of the basin, is much higher while a weaker stratification is seen for the density classes outcropping in the periodic channel. A thermostad is also observed in the lower part of the lower branch of the MOC. The maximum of the MOC in the mid latitudes is found at a depth similar to the maximum depth reached by b_S (in the zonal average). This correspondence is not perfect in the various simulations, but the two depths are very similar in all experiments. Analogous conclusions may be drawn considering the temperature profile at the eastern boundary instead of the average one.

It is clear from Fig. 5.4 that a large part of the overturning is confined at the northern end of the basin, at least for the low-diffusivity simulations (as the

one in Fig. 5.4). A large part of the water sinking at the northern boundary is upwelled already in the centre of the subpolar gyre. This is, at least in part, an artefact of the low resolution model used here, that has a too broad and weak rim current in the subpolar gyre, not substantially warmer than the interior. It is also possible that a portion of the water sinking in the subpolar gyre is not dense enough to enter the subtropical ocean in the lower branch of the MOC, and consequently recirculates within the subpolar gyre. As we are interested in the basin scale MOC, we measure the MOC by its maximum south of the latitude where b_S reaches its maximum depth on the eastern boundary, before outcropping in the NH (this amounts in practice to considering the maximum in the subtropical ocean). Other measures of the MOC can in fact be used, e. g. the global MOC maximum, leading to similar conclusions; this one is used here since it gives the best results.

It is interesting to consider first the prediction of the MOC strength using the geostrophic scaling (5.4), based on the east–west buoyancy difference (Fig. 5.5, top left). The scaling plotted is in this case the maximum of the right hand side of (5.4) in the NH.² The scaling is very well correlated with the MOC strength (correlation 0.91). This is true particularly, but by no means exclusively, for the simulations with lower diffusivity (blue colour in the figure). We thus find further evidence that the MOC is indeed in geostrophic balance [14, 18, 72].

A step forward is made evaluating the MOC strength predicted by the scaling (5.5), based on the north–south buoyancy difference (Fig. 5.5, top right). Also this scaling, computed in a completely independent way from the other, gives a very good estimate of the MOC maximum in the simulations considered (the correlation between the two data sets is 0.88). The agreement is also here particularly good for the set of simulations with the lowest value of vertical diffusivity. We thus see that measuring the buoyancy difference between the northern end of the basin and the northern end of the periodic channel is in fact an effective way to estimate the MOC strength, since it is in fact a way to estimate the east–west buoyancy difference setting the MOC strength by thermal wind. This is confirmed by the bottom panel of Fig. 5.5, demonstrating the strong correlation (0.96) between the two scalings, one based on the east–west and the other on the north–south buoyancy difference. This holds even when vertical diffusivity is not negligible, when the diabatic downward propagation of the surface buoyancy signal can have a stronger impact on the stratification. In presence of finite vertical diffusivity, the properties at the surface in the periodic channel can only give an estimate of the stratification in the zonally enclosed part of the basin.

² Also in this case, to avoid contamination from the overturning limited to the subpolar gyre, the maximum considered is the southernmost one in the NH.

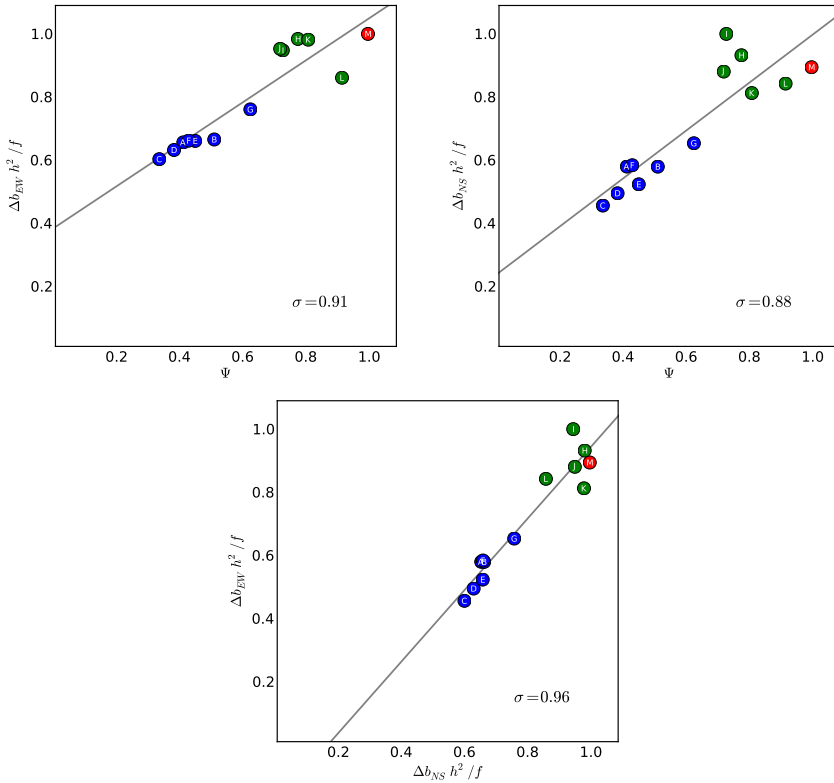


Figure 5.5: The MOC strength (Ψ) predicted from the scalings $\Psi \sim (1/f)\Delta b_{EW}h^2$ (top left panel) and $\Psi \sim (1/f)\Delta b_{SN}h^2$ (top right panel) as a function of the measured MOC. The correlation between the two scalings is shown in the lower panel. Colours refer to the vertical diffusivity prescribed in the ocean interior: $1.0 \cdot 10^{-5} \text{ m}^2 \text{ s}^{-1}$ (blue), $5.0 \cdot 10^{-5} \text{ m}^2 \text{ s}^{-1}$ (green), $1.0 \cdot 10^{-4} \text{ m}^2 \text{ s}^{-1}$ (red). The MOC strength is measured by the maximum in the subtropical ocean (see text). The values are normalised to the maximum in the two directions. The letters in the circles refer to the experiment names of Tab. 5.1. The grey lines are linear regressions through the data. The correlation between the data sets are reported in each panel.

It is also important to remember that the locking of the pycnocline outcropping latitude (θ_0 in Fig. 5.1) to the northern end of the periodic channel is only approximate. Better agreement between the scaling (5.5) and the MOC strength could be obtained by taking into account the shifts of the pycnocline outcropping position between the different simulations. This is particularly true for run I, for which a much better agreement with the other simulations in Fig. 5.5 (top right) would be obtained by computing b_S slightly more to the north (0.5°) than for the other simulations (the correlation increases from 0.88 to 0.91). However, the improved correlation would be traded with a loss of generality of the approach.

5.5 CONCLUSIONS

The main conclusion to be drawn from this work is that the north–south buoyancy difference can be connected to the east–west density difference in the NH, which in turn is in thermal wind balance with the MOC. This connection is possible by considering the pycnocline structure in presence of a zonally periodic channel in the SH. This link between meridional and zonal buoyancy gradients enables to predict the MOC strength from the meridional buoyancy gradient, without invoking ageostrophic effects. The relevant north–south buoyancy difference is identified unambiguously as the difference between the dense-water formation regions in the NH and the northern end of the periodic channel in the SH.

Our view is close to the one of Johnson and Marshall [56] (Eq. 5.2), with an important new element: the lightest buoyancy involved in the scaling is not an average over the whole pycnocline, but rather an estimate at its lower boundary. Considering a two layer system seems to be an oversimplification if the MOC strength has to be predicted, and if a connection has to be made between meridional density gradient and vertical stratification. This is evident considering in particular experiments A and F, which differ only for the restoring temperature in the tropical region. The zonally averaged temperature structure in the two simulations is markedly different (not shown), with both a warmer pycnocline and a warmer interior in run F (the configuration with warmer tropical surface temperature). However, the two simulations have very similar MOC strength. In fact the pycnocline depth and the temperature at the base of the pycnocline are virtually the same. The restoring surface temperature in the periodic channel is the same in the two simulations (only tropical surface temperatures are increased in run F), and the properties at the base of the pycnocline are thus very similar, since diffusivity plays a secondary role. The only significant difference between the two simulations is in the northern temperature, higher in run F since the water flowing northward from the pycnocline is warmer; this differ-

ence is responsible for the slightly lower MOC strength of run F. Measuring the southern temperature entering the scaling over a larger area, e. g. averaging over the tropical ocean as in [67], would clearly fail to predict the correct MOC strength. Considering runs H and K, equivalent to A and F respectively but with a higher vertical diffusivity of $5 \cdot 10^{-5} \text{ m}^2 \text{ s}^{-1}$, the boundary conditions in the tropics are instead more important. The upwelling at low latitudes is in this case a significant contribution to the total upwelling, and the conditions of the upper pycnocline have more impact on the MOC strength.

Even if the MOC is to a large extent in geostrophic balance, meridional pressure gradients are likely of fundamental importance as drivers of the MOC in the western boundary and at low latitudes. In fact, a meridional pressure gradient in the western boundary is likely to be caused by the density structure discussed here: the isopycnals at the bottom of the pycnocline are zonally flat in the south, close to the zonally periodic channel that prevents the maintenance of zonal pressure gradients. On the other hand, the isopycnals at the bottom of the pycnocline are sloping upwards to the west in the NH, due to the presence of the southward flowing deep western boundary current. This different zonal slope of the pycnocline may be the origin of the meridional pressure gradient which Sijp et al. [95] suggest as the main driver of the MOC at low latitudes.

It is also tempting to make a link between our hypothesis and the adiabatic overturning paradigm of Samelson [90] and Wolfe and Cessi [121]. Wolfe and Cessi [120] suggest that the adiabatic MOC follows a non-local scaling governed by the surface buoyancy range shared between the NH and the periodic channel in the south, Δb_c . This is equivalent to the north-south scaling (5.5) if one considers that Δb_c has to be computed as the same difference which has been used here, namely the difference between the lightest classes found at the northern end of the periodic channel in the south (b_S) and the densest class found in the north (b_N). This must be the case as, in the adiabatic limit, no water lighter than b_S can be upwelled from intermediate depth, and thus no water lighter than b_S can enter the MOC. The densest water which can enter the inter-hemispheric MOC is instead b_N , since no water denser than this class is formed in the NH, while the denser waters produced in the SH enter the deep overturning instead of the intermediate one considered here.

Concluding, we would like to stress that the results presented here, similarly to what seen in Chaps. 3 and 4, point to the fact that the SH, and in particular the region north of the periodic channel, exerts a strong control over the dynamics of the MOC.

CONCLUSIONS

In this thesis, a series of investigations on feedback processes connected with the Atlantic Meridional Overturning Circulation (AMOC) stability has been presented. In the study, a hierarchy of models of different complexity has been used. Given the limited observational data available on the AMOC properties and on its stability changes, and the limited understanding of the system, the work is of an idealised nature. The general aim has been trying to understand the steady state stability behaviour in the simplest numerical models available, i. e. coarse resolution models.

6.1 ATMOSPHERIC FEEDBACKS

Starting with a fully coupled General Circulation Model (GCM), even if a coarse resolution one, ocean–atmosphere feedbacks have been analysed during an externally forced collapse of the AMOC. A simplified representation of the feedbacks was obtained, in order to develop a Hybrid Coupled Model (HCM) with an ocean GCM coupled to a minimal empirical atmospheric model. This approach has proven to be successful, and the HCM is very efficient while still retaining a valid representation of ocean–atmosphere feedbacks at long time-scales. The boundary conditions developed in Chap. 2 were used in the study by den Toom et al. [23], in a detailed investigation of the impact of atmospheric feedbacks on the AMOC stability. It is worthwhile to briefly report here the main results of this study. The surface fluxes described in Chap. 2 are used in den Toom et al. [23] as boundary conditions for the implicit ocean model THCM, described in section 3.2.2. Bifurcation diagrams are constructed computing the overturning strength as a function of an anomalous freshwater flux centred south of Greenland (same as in Fig. 3.1), used as the bifurcation parameter. The feedbacks caused by the various atmospheric fluxes (heat, freshwater and momentum) are first considered separately, and then together. The results are summarised in Fig. 6.1. Heat feedback (panel b) contributes to destabilising the “ON” state of the AMOC, while stabilising the “OFF” state, without affect-

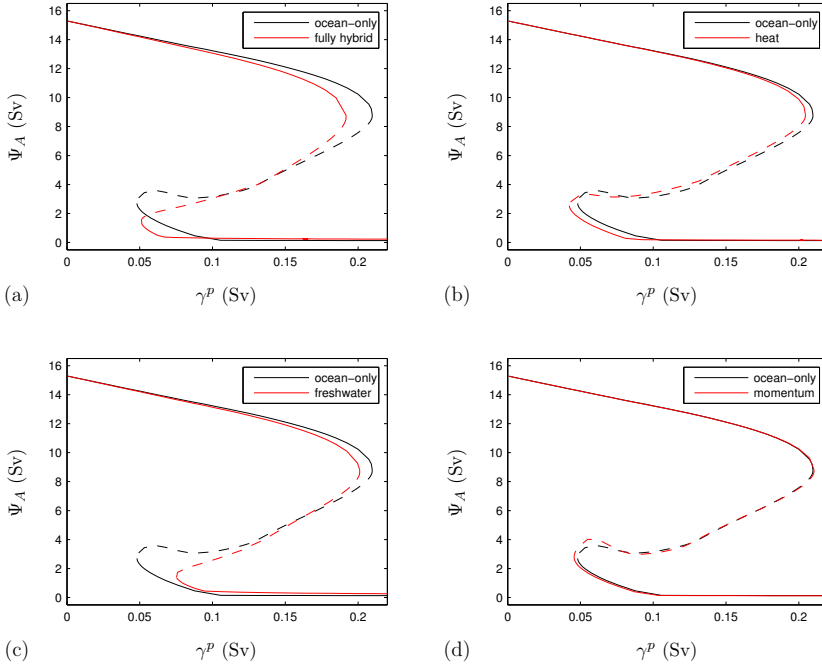


Figure 6.1: Changes in the bifurcation diagram due to the atmospheric feedbacks. The black line represents the ocean-only case and the red lines correspond to (a) the full HCM, and the cases with only (b) state-dependent heat fluxes, (c) state-dependent freshwater fluxes, and (d) state-dependent momentum fluxes enabled. Figure from den Toom et al. [23].

ing significantly the width of the Multiple Equilibria (ME) regime. Feedbacks connected to freshwater fluxes (panel c) cause a destabilisation of both the “ON” and the “OFF” states, reducing the width of the ME regime. Feedbacks connected to the wind (panel d) seem not have a large impact, but the highly viscous nature of the flow in THCM may be biasing the results in this case. The collective impact of all the feedbacks (panel a) is to narrow the ME regime, but the magnitude of the changes is not large in this model. These results suggest that the magnitude of the ocean–atmosphere feedbacks is not of primary importance, even if further research is needed in order to check whether these conclusions are robust in other models too.

6.2 SALT-ADVECTION FEEDBACK IN THE OCEAN

Chapters 3 and 4 focus on ocean-only feedbacks, in particular the salt-advection feedback. In two different numerical models and a simple box model, the control exerted from the South Atlantic on the AMOC stability has been demonstrated and investigated in detail. In particular, the zonal salinity gradient in the South Atlantic can control the sign of the salt-advection feedback, and can thus control the stability of the AMOC. A complete collapse of the AMOC can in fact be caused not only by a positive freshwater anomaly applied over the South Atlantic, but also by an appropriate dipole anomaly, modifying directly the zonal salinity contrast in the South Atlantic but not changing the net evaporation out of the basin.

These results are particularly interesting considering the ubiquitous biases in salinity and freshwater transport observed in numerical climate models [30]. Any inference on the fate of the AMOC in a warming climate should take into account the effect of such biases, which may have a deep effect on the response of the AMOC to global warming.

In this respect, the results from the box model on the skill of the quantity M_{ov} as ME indicator provides an important guide when trying to determine the importance of salt-advection feedback in more complex climate models. The box model suggests that M_{ov} can provide a first indication on the sign of the salt-advection feedback even if other feedback mechanisms are active, in particular horizontal gyres and vertical diffusion.

In Chap. 5, the control exerted on the AMOC from the Southern Hemisphere (SH) has been linked to the pycnocline theory, discussing why the region at the northern end of the Antarctic Circumpolar Current (ACC) plays a particularly important role in setting the AMOC strength and stability. Looking back at the results of Chap. 3, we can argue that the dipole anomaly used therein does not change substantially the density at the depth of the AMOC maximum (see Fig. 3.3 B), and is thus not strongly affecting the AMOC strength, but rather changing the properties of the bulk of the pycnocline. As seen in Chap. 5, this does not have a strong impact on the AMOC strength, but still pushes the system closer to the collapse point since a smaller perturbation will be needed to stop dense water formation.

6.3 TOWARDS AN UNDERSTANDING OF THE THREE DIMENSIONAL, TURBULENT AMOC

A more important result from the box model developed in Chap. 4 may be in fact a more abstract one. The box model reproduces the results of more complex numerical models in a relatively simple framework. In doing so, the as-

sumptions implicitly made when using a GCM, in particular at coarse resolution, are made explicit. These implicit assumptions, as such, should be challenged in future research focusing on the AMOC and its stability. The three fundamental ones may be identified as:

- (i) the assumption that the dynamics of the AMOC have a fundamentally two dimensional meridional character,
- (ii) the assumption that the AMOC is meridionally coherent on long time scales,
- (iii) the assumption that the ocean behaves as a diffusive system on long time scales.

Assumption (i) means that, discussing the AMOC as a two-dimensional phenomenon, the ubiquitous zonal asymmetries observed in the ocean are neglected, the most prominent of which are the horizontal gyres and the associated strong western boundary currents. Are these asymmetries a higher order effect, or is the interaction between the AMOC and the horizontal gyres essential? The results of this work point in the latter direction, stressing the essential role in particular of the freshwater transport by the southern subtropical gyre in the Atlantic Ocean. Other elements of the ocean circulation may be important in this respect too, e. g. the Agulhas current and the western boundary currents, in particular at the equator and in the Northern Hemisphere (NH).

Assumption (ii) means that the AMOC, and in particular its response to perturbations, is thought to be coherent on the meridional plane. An anomaly applied in the northern North Atlantic will have a basin-wide impact on time scales longer than the adjustment time, usually on the order of decades [41, 118].¹ In the steady state box-model of Chap. 4, this is reflected in the use of boxes spanning both hemispheres, which amounts to assuming that the AMOC will change in the same way from North to South. It is not obvious whether this assumption is true in a turbulent ocean [22].

Assumption (iii) is partly connected to (ii), and implies that the ocean is thought to behave as a diffusive system on large spatial and temporal scales. For instance, salinity anomalies applied in the South Atlantic will reach the convective regions of the northern North Atlantic on sufficiently long time scales. What would be the fate of such an anomaly in the real ocean, turbulent and non-diffusive? On one hand, anomalies may have a higher coherence, as signals are not spread out and damped by diffusion. On the other hand, a turbulent ocean may provide sharp barriers to transport [see e.g. 51]. It is still unclear to what extent and on which time scales these barriers would inhibit

¹ This time scale is obviously not the one needed for the system to reach an equilibrium state, but rather the time scale needed for an anomaly to propagate in the basin.

transport of tracers, but they may, in principle, have a strong impact on the dynamics of the basin-scale salt-advection feedback discussed in this work.

A further assumption is made neglecting the interaction with the atmosphere. This choice is supported in particular by den Toom et al. [23], but a stronger impact of ocean–atmosphere interaction can not be ruled out at the moment, in particular using a less viscous model, where wind feedback could have a much larger effect.

In conclusion, we see that the understanding of the AMOC in the real world, in particular for what concerns its stability properties, is far from being clear. Still, this work has made an attempt to make some progress in the understanding of the AMOC in numerical models that, despite their limitations, still provide one of the few tools with which hypothesis on the AMOC behaviour can be tested. In this framework, progress on the characterisation of the steady state behaviour has indeed been made, in particular concerning the importance of salt-advection feedback and freshwater exchange between the Atlantic and the Southern Oceans. This can contribute to the “backbone” of the understanding of the dynamics in the World Ocean. The next step is to challenge these results, in order to assess their robustness, and to proceed in the understanding of the dynamics of the AMOC in the real ocean.

A

EQUIVALENT FRESHWATER BUDGET IN THE ATLANTIC OCEAN

The volume budget of the Atlantic Ocean can be written as:

$$\frac{\partial V}{\partial t} = \int_{BS} v \, dx \, dz + \int_{30S} v \, dx \, dz - EPR, \quad (\text{A.1})$$

where v is the meridional velocity, BS and $30S$ indicate integration over a zonal transect in the Bering strait and at $30^\circ S$ in the Atlantic Ocean respectively. EPR is the net evaporation over the basin and V is volume. The subscript t denotes time derivative. The volume change in the basin is the balance between inflow from zonal boundaries and net evaporation.

A.1 EQUIVALENT FRESHWATER BUDGET

Local salt conservation is expressed by:

$$\frac{\partial S}{\partial t} + \mathbf{u} \cdot \nabla S = -\nabla \mathcal{F}_S, \quad (\text{A.2})$$

where S is salinity, \mathbf{u} is the horizontal velocity vector and \mathcal{F}_S is the diffusive salt flux. Diffusive fluxes depend on model definition, so we avoid writing them explicitly. Integrating Eq. A.2 over the whole Atlantic basin, using Gauss theorem and assuming no salt flux at the surface and bottom and no diffusion across Bering strait, one obtains:

$$\frac{\partial}{\partial t} \int_{Atl} S \, dV - \int_{30S} vS \, dx \, dz - \int_{BS} vS \, dx \, dz = \int_{30S} \mathcal{F}_S \, dx \, dz. \quad (\text{A.3})$$

Using a reference salinity S_0 :

$$S_0 = \frac{\int_{30S} S \, dx \, dz}{\int_{30S} dx \, dz}, \quad (\text{A.4})$$

an equivalent freshwater transport can be defined from A.3:

$$-\frac{1}{S_0} \frac{\partial}{\partial t} \int_{Atl} S \, dV = -\frac{1}{S_0} \int_{30S} vS \, dx dz - \frac{1}{S_0} \int_{BS} vS \, dx dz - \frac{1}{S_0} \int_{30S} \mathcal{F}_S \, dx dz,$$

written in short as:

$$Q_t = M_{30S} - \frac{1}{S_0} \int_{BS} vS \, dx dz + M_d + Res, \tag{A.5}$$

where *Res* is a residual.

A.1.1 Virtual freshwater transport at 30°S

The term M_{30S} in Eq. A.5 is split in two parts:

$$\begin{aligned} M_{30S} &= -\frac{1}{S_0} \int_{30S} vS \, dx dz \\ &= -\frac{1}{S_0} \int_{30S} (\langle v \rangle + v')(\langle S \rangle + S') \, dx dz \\ &= -\frac{1}{S_0} \left(\int_{30S} \langle v \rangle \langle S \rangle \, dx dz + \int_{30S} v' S' \, dx dz \right), \end{aligned} \tag{A.6}$$

where, for a generic field f , the zonal operator is $\langle f \rangle = \int_{60^\circ W}^{20^\circ E} f \, dx / \int dx$ and the azonal operator is $f' = f - \langle f \rangle$.

Using the two definitions:

$$\begin{aligned} M_{ov} &= -\frac{1}{S_0} \int_{30S} \tilde{v}(\langle S \rangle - S_0) \, dx dz \\ M_{az} &= -\frac{1}{S_0} \int_{30S} v' S' \, dx dz, \end{aligned}$$

where for a generic field f the barotropic operator is $\bar{f} = \int f \, dz / \int dz$ and the baroclinic operator is $\tilde{f} = f - \bar{f}$, Eq. A.6 becomes:

$$M_{30S} = M_{ov} + M_{az} - \int_{30S} v \, dx dz. \tag{A.7}$$

Using Eq. A.7, the volume *outflow* of water at 30S can be represented by a virtual freshwater *inflow*.

Putting together Eqs. A.1 and A.7 into the virtual freshwater budget of Eq. A.5 we obtain Eq. 3.3:

$$EPR + Q_t + V_t = M_{ov} + M_{az} + M_d + M_{BS} + Res,$$

with $V_t = \partial V / \partial t$ the volume drift in the basin, and defining:

$$M_{BS} = \int_{BS} v dx dz - \frac{1}{S_0} \int_{BS} v S dx dz.$$

The inflow of freshwater in the basin must balance net evaporation and the drift in volume and salinity.

In the calculations, baroclinic velocity can be used instead of actual one, as long as Eq. A.4 is used as the definition of S_0 . This stems from the definition of baroclinic velocity.

A.2 FRESHWATER BUDGET IN CLIO

The terms in Eq. 3.3 for the control state of the Earth Model of Intermediate Complexity (EMIC) SPEEDO are reported in table 3.2. Very similar numbers are obtained for the HCM. In the model, the freshwater anomalies are implemented as a virtual salt flux, which can easily be accounted for by a surface salt flux in Eq. A.2. Here we include this term into EPR for simplicity.

The largest terms in the budget are EPR , M_{ov} and M_{az} by at least one order of magnitude. Moreover, the other terms are also less sensitive to the freshwater anomalies applied so that they are approximately constant, with the exception of Q_t . As discussed in section 3.4 this depends on the details of the model used. As an example, in THCM, the term M_d plays instead a primary role, and behaves in a way similar to M_{az} in SPEEDO.

B

DERIVATION OF $E_a|_{M_{ov}}^0$ AND Δ_E

To compute the E_a value needed to bring M_{ov} to zero with $q_S > 0$, the system (4.10) has to be solved.

In the non diffusive limit $\kappa \rightarrow 0$ Eq. (4.10e) reduces to $q_S - q_N = 0$, a second order equation in D , which can be solved giving as positive solution:

$$\lim_{\kappa \rightarrow 0} D|_{M_{ov}}^0 = -\frac{1}{2} \frac{1}{(T_{ts} - T_n) \alpha \eta} \frac{A_{GM} L_{xA}}{L_y} \times \left[1 - \sqrt{1 + 4 q_{Ek} \left(\frac{L_y}{A_{GM} L_{xA}} \right)^2 (T_{ts} - T_n) \alpha \eta} \right].$$

This result can be substituted into Eqs. (4.10a)–(4.10d), and salinity can be eliminated giving:

$$\begin{aligned} E_s \left[r_N - r_S + (T_{ts} - T_n) \left(D|_{M_{ov}}^0 \right)^2 \alpha \eta \right] = \\ E_a \left[r_N + r_S + (T_{ts} - T_n) \left(D|_{M_{ov}}^0 \right)^2 \alpha \eta \right]. \end{aligned} \quad (\text{B.1})$$

The latter is solved for E_a giving $E_a|_{M_{ov}}^0$ in the case of $\kappa \rightarrow 0$:

$$\begin{aligned} \lim_{\kappa \rightarrow 0} E_a|_{M_{ov}}^0 &= E_s \frac{r_N - r_S + (T_{ts} - T_n) \left(D|_{M_{ov}}^0 \right)^2 \alpha \eta}{r_N + r_S + (T_{ts} - T_n) \left(D|_{M_{ov}}^0 \right)^2 \alpha \eta} \\ &= E_s \frac{r_N - r_S + q_N|_{M_{ov}}^0}{r_N + r_S + q_N|_{M_{ov}}^0}. \end{aligned} \quad (\text{B.2})$$

(B.2) can be combined with Eq. (4.9) to give Δ_E in the non diffusive limit, Eq. (4.11).

The method outlined for the non diffusive limit can be used for the model including vertical diffusion as well. Also in this case, the mathematics involved

is very simple on conceptual grounds, but the large expressions obtained render the problem tedious with pencil and paper. The final result is obtained with Mathematica software. Eq. (4.10d), in this case a third order algebraic equation, can be solved for pycnocline depth, and the positive solution reads:

$$D|_{M_{ov}}^0 = \frac{A_{GM} L_{xA}}{3 L_y (T_n - T_{ts}) \alpha \eta} \frac{(1 + i\sqrt{3}) \left(A_{GM}^2 L_{xA}^2 + 3 L_y^2 q_{Ek} (T_{ts} - T_n) \alpha \eta \right)}{\left(3 \sqrt[3]{4} L_y (T_n - T_{ts}) \alpha \eta \left[2 A_{GM}^3 L_{xA}^3 + 9 A_{GM} L_{xA} L_y^2 q_{Ek} (T_{ts} - T_n) \alpha \eta \right] - 3 L_y^{3/2} (T_n - T_{ts}) \alpha \eta \left[9 A L_y^{3/2} (T_n - T_{ts})^2 \alpha \eta \kappa - \sqrt{3} (T_n - T_{ts}) \left(A_{GM}^2 L_{xA}^2 L_y q_{Ek}^2 + 4 A A_{GM}^3 L_{xA}^3 \kappa - 18 A A_{GM} L_{xA} L_y^2 q_{Ek} (T_n - T_{ts}) \alpha \eta \kappa - L_y^3 (T_n - T_{ts}) \alpha \eta \left(4 q_{Ek}^3 + 27 A^2 (T_n - T_{ts}) \alpha \eta \kappa^2 \right) \right)^{1/2} \right] \right)^{1/3}} + \frac{1}{6 \sqrt[3]{2} L_y (T_n - T_{ts}) \alpha \eta} (i\sqrt{3} - 1) \times \left(2 A_{GM}^3 L_{xA}^3 + 9 A_{GM} L_{xA} L_y^2 q_{Ek} (T_{ts} - T_n) \alpha \eta - 3 L_y^{3/2} (T_n - T_{ts}) \alpha \eta \left[9 A L_y^{3/2} (T_n - T_{ts}) \alpha \eta \kappa + \sqrt{3} \left(-A_{GM}^2 L_{xA}^2 L_y q_{Ek}^2 - 4 A A_{GM}^3 L_{xA}^3 \kappa + 18 A A_{GM} L_{xA} L_y^2 q_{Ek} (T_n - T_{ts}) \alpha \eta \kappa + L_y^3 (T_n - T_{ts}) \alpha \eta \left(4 q_{Ek}^3 + 27 A^2 (T_n - T_{ts}) \alpha \eta \kappa^2 \right) \right)^{1/2} \right] \right)^{1/3}$$

After eliminating salinity, Eqs. (4.10a)–(4.10d) reduce again to (B.1), and $E_a|_{M_{ov}}^0$ is still given by Eq. (B.2), but with $D|_{M_{ov}}^0$ and $q_N|_{M_{ov}}^0$ for the finite vertical diffusion case.

The difference between $E_a|_{q_N}^0$ and $E_a|_{M_{ov}}^0$ then gives Δ_E , which can be written as:

$$\begin{aligned} \Delta_E &= \frac{2E_s r_S}{r_N + r_S + (T_{ts} - T_n) \left(D|_{M_{ov}}^0 \right)^2 \alpha \eta} \\ &\quad \left\{ A_{GM} D|_{q_N}^0 L_{xA} \left[A_{GM} D|_{q_N}^0 L_{xA} + L_y (r_S - q_{Ek}) \right] \right\} \\ &\quad \left\{ \times [r_N (T_n - T_{ts}) \alpha + 2E_s S_0 \beta] \right\} \\ &= \frac{2E_s r_S}{r_N + r_S + q_N|_{M_{ov}}^0} \\ &\quad - \frac{q_e|_{q_N}^0 \left(q_e|_{q_N}^0 + r_S - q_{Ek} \right) [r_N (T_n - T_{ts}) \alpha + 2E_s S_0 \beta]}{\left[\left(A_{GM} D|_{q_N}^0 L_{xA} \right)^2 + L_y^2 q_{Ek} r_N + A_{GM} D|_{q_N}^0 L_{xA} L_y (r_S - q_{Ek}) \right] S_0 \beta} \\ &\quad - \frac{\left[\left(q_e|_{q_N}^0 \right)^2 + q_{Ek} r_N + q_e|_{q_N}^0 (r_S - q_{Ek}) \right] S_0 \beta}{\left[\left(q_e|_{q_N}^0 \right)^2 + q_{Ek} r_N + q_e|_{q_N}^0 (r_S - q_{Ek}) \right] S_0 \beta}. \end{aligned}$$

In the limit of no vertical diffusion, $q_e|_{q_N}^0 = q_{Ek}$ if $q_N = 0$, and thus Δ_E reduces to:

$$\lim_{\kappa \rightarrow 0} \Delta_E = r_S \left[\frac{2E_s}{r_N + r_S + q_N|_{M_{ov}}^0} - \frac{2E_s}{r_N + r_S} + \frac{r_N (T_{ts} - T_n) \alpha}{(r_N + r_S) S_0 \beta} \right],$$

which can be written in the form of Eq. (4.11) when $q_N|_{M_{ov}}^0$ is written explicitly.

BIBLIOGRAPHY

- [1] R. B. Alley, J. Marotzke, W. D. Nordhaus, J. T. Overpeck, D. M. Peteet, R. a. Pielke, R. T. Pierrehumbert, P. B. Rhines, T. F. Stocker, L. D. Talley, and J. M. Wallace. Abrupt climate change. *Science*, 299:2005–2010, 2003.
- [2] L. C. Allison, H. L. Johnson, D. P. Marshall, and D. R. Munday. Where do winds drive the Antarctic Circumpolar Current? *Geophysical Research Letters*, 37:L12605, 2010.
- [3] O. Arzel, M. H. England, and O. A. Saenko. The impact of wind stress feedback on the stability of the Atlantic Meridional Overturning Circulation. *Journal of Climate*, 24:1965–1984, 2011.
- [4] T. P. Barnett, M. Latif, N. Graham, M. Flugel, S. Pazan, and W. White. ENSO and enso-related predictability. Part I: prediction of equatorial Pacific sea surface temperature with a hybrid coupled ocean-atmosphere model. *Journal of Climate*, 6:1545–1566, 1993.
- [5] L. M. Beal, W. P. M. De Ruijter, A. Biastoch, and R. Zahn. On the role of the Agulhas system in ocean circulation and climate. *Nature*, 472:429–436, 2011.
- [6] A. S. Bower, M. S. Lozier, S. F. Gary, and C. W. Böning. Interior pathways of the North Atlantic meridional overturning circulation. *Nature*, 459:243–247, 2009.
- [7] A. Bracco, F. Kucharski, R. Kallummal, and F. Molteni. Internal variability, external forcing and climate trends in multi-decadal AGCM ensembles. *Climate Dynamics*, 23:659–678, 2004.
- [8] W.-P. Breugem, W. Hazeleger, and R. J. Haarsma. Mechanisms of northern tropical Atlantic variability and response to CO₂ doubling. *Journal of Climate*, 20:2691–2705, 2007.
- [9] W. S. Broecker. Thermohaline Circulation, the Achilles heel of our climate system: will man-made CO₂ upset the current balance? *Science*, 278:1582–1588, 1997.
- [10] G. Burgers and G. Jan van Oldenborgh. On the impact of local feedbacks in the central Pacific on the ENSO cycle. *Journal of Climate*, 16:2396–2407, 2003.

- [11] J. Callies and J. Marotzke. A simple and self-consistent geostrophic-force-balance model of the Thermohaline Circulation with boundary mixing. *Ocean Science*, 8:49–63, 2012.
- [12] M. A. Cane. El Niño. *Annual Review of Earth and Planetary Sciences*, 14: 43–70, 1986.
- [13] P. Cessi and M. Fantini. The eddy-driven thermocline. *Journal of Physical Oceanography*, 34:2642–2658, 2004.
- [14] P. Cessi and C. L. Wolfe. Eddy-driven buoyancy gradients on eastern boundaries and their role in the thermocline. *Journal of Physical Oceanography*, 39:1595–1614, 2009.
- [15] A. Cimadoribus, S. Drijfhout, M. den Toom, and H. Dijkstra. Sensitivity of the Atlantic meridional overturning circulation to South Atlantic freshwater anomalies. *Climate Dynamics*, 39:2291–2306, 2012.
- [16] A. Cimadoribus, S. Drijfhout, and H. Dijkstra. A global hybrid coupled model based on atmosphere-SST feedbacks. *Climate Dynamics*, 38:745–760, 2012.
- [17] P. U. Clark, N. G. Pias, T. F. Stocker, and A. J. Weaver. The role of the Thermohaline Circulation in abrupt climate change. *Nature*, 415: 863–869, 2002.
- [18] S. A. Cunningham, T. Kanzow, D. Rayner, M. O. Baringer, W. E. Johns, J. Marotzke, H. R. Longworth, E. M. Grant, J. J.-M. Hirschi, L. M. Beal, C. S. Meinen, and H. L. Bryden. Temporal variability of the Atlantic Meridional Overturning Circulation at 26.5°N. *Science*, 317:935–938, 2007.
- [19] V. Daru and C. Tenaud. High order one-step monotonicity-preserving schemes for unsteady compressible flow calculations. *Journal of Computational Physics*, 193:563–594, 2004.
- [20] A. M. De Boer, A. Gnanadesikan, N. R. Edwards, and A. J. Watson. Meridional density gradients do not control the Atlantic Overturning Circulation. *Journal of Physical Oceanography*, 40:368–380, 2010.
- [21] P. de Vries and S. L. Weber. The Atlantic freshwater budget as a diagnostic for the existence of a stable shut down of the meridional overturning circulation. *Geophysical Research Letters*, 32:L09606, 2005.
- [22] M. den Toom, H. A. Dijkstra, W. Weijer, M. W. Hecht, M. E. Maltrud, and E. van Sebille. Sensitivity of a strongly eddying global ocean to

- North Atlantic freshwater perturbations. *Journal of Physical Oceanography*, submitted, 2012.
- [23] M. den Toom, H. A. Dijkstra, A. A. Cimadoribus, and S. S. Drijfhout. Effect of atmospheric feedbacks on the stability of the Atlantic Meridional Overturning Circulation. *Journal of Climate*, 25:4081–4096, 2012.
- [24] C. Deser and J. M. Wallace. Large-scale atmospheric Circulation features of warm and cold episodes in the tropical Pacific. *Journal of Climate*, 3:1254–1281, 1990.
- [25] R. R. Dickson and J. Brown. The production of North Atlantic deep water: Sources, rates, and pathways. *Journal of Geophysical Research*, 99:12319–12341, 1994.
- [26] H. A. Dijkstra. Scaling of the atlantic meridional overturning circulation in a global ocean model. *Tellus A*, 60:749–760, 2008.
- [27] H. A. Dijkstra. *Dynamical Oceanography*. Springer, Berlin, Germany, 2008.
- [28] H. A. Dijkstra and W. Weijer. Stability of the global ocean circulation: basic bifurcation diagrams. *Journal of Physical Oceanography*, 35:933–948, 2005.
- [29] E. J. Doedel and B. E. Oldeman. AUTO-07P: continuation and bifurcation software for ordinary differential equations. Concordia University, Montreal, Canada, 2009.
- [30] S. Drijfhout, S. Weber, and E. van der Swaluw. The stability of the MOC as diagnosed from model projections for pre-industrial, present and future climates. *Climate Dynamics*, 37:1575–1586, 2011.
- [31] S. S. Drijfhout. The atmospheric response to a Thermohaline Circulation collapse: Scaling relations for the Hadley Circulation and the response in a coupled climate model. *Journal of Climate*, 23:757–774, 2010.
- [32] R. Farneti, T. L. Delworth, A. J. Rosati, S. M. Griffies, and F. Zeng. The role of mesoscale eddies in the rectification of the Southern Ocean response to climate change. *Journal of Physical Oceanography*, 40:1539–1557, 2010.
- [33] R. Ferrari and C. Wunsch. Ocean circulation kinetic energy: reservoirs, sources, and sinks. *Annual Review of Fluid Mechanics*, 41:253–282, 2009.

- [34] C. Frankignoul. Sea surface temperature anomalies, planetary waves, and air–sea feedback in the middle latitudes. *Reviews of Geophysics*, 23: 357–390, 1985.
- [35] Y. Friocourt, S. Drijfhout, B. Blanke, and S. Speich. Water mass export from Drake Passage to the Atlantic, Indian, and Pacific oceans: A Lagrangian model analysis. *Journal of Physical Oceanography*, 35:1206–1222, 2005.
- [36] A. Ganachaud and C. Wunsch. Large-scale ocean heat and freshwater transports during the world ocean Circulation experiment. *Journal of Climate*, 16:696–705, 2003.
- [37] A. Ganopolski and S. Rahmstorf. Rapid changes of glacial climate simulated in a coupled climate model. *Nature*, 409:153–158, 2001.
- [38] S. L. Garzoli and R. Matano. The South Atlantic and the Atlantic Meridional Overturning Circulation. *Deep Sea Research Part II: Topical Studies in Oceanography*, 58:1837–1847, 2011.
- [39] P. R. Gent and J. C. McWilliams. Isopycnal mixing in ocean circulation models. *Journal of Physical Oceanography*, 20:150–155, 1990.
- [40] M. Ghil, M. R. Allen, M. D. Dettinger, K. Ide, D. Kondrashov, M. E. Mann, A. W. Robertson, A. Saunders, Y. Tian, F. Varadi, and P. Yiou. Advanced spectral methods for climatic time series. *Reviews of Geophysics*, 40: 1003, 2002.
- [41] A. E. Gill. *Atmosphere–Ocean Dynamics*. Academic Press, San Diego, USA and London, UK, 1982.
- [42] A. Gnanadesikan. A simple predictive model for the structure of the oceanic pycnocline. *Science*, 283:2077–2079, 1999.
- [43] H. Goosse and T. Fichefet. Importance of ice–ocean interactions for the global ocean circulation: A model study. *Journal of Geophysical Research*, 104:23337–23356, 1999.
- [44] V. V. Gouretski and K. P. Koltermann. WOCE global hydrographic climatology. Bundesamt für Seeschifffahrt und Hydrographie, Hamburg and Rostock, Germany, 2004.
- [45] N. E. Graham and T. P. Barnett. Sea surface temperature, surface wind divergence, and convection over tropical oceans. *Science*, 238:657–659, 1987.

- [46] A. Griesel and M. A. M. Maqueda. The relation of meridional pressure gradients to North Atlantic deep water volume transport in an ocean general circulation model. *Climate Dynamics*, 26:781–799, 2006.
- [47] Y. P. Guan and R. X. Huang. Stommel’s box model of Thermohaline Circulation revisited—the role of mechanical energy supporting mixing and the wind-driven gyration. *Journal of Physical Oceanography*, 38: 909–917, 2008.
- [48] S. K. Gulev, B. Barnier, H. Knochel, J. M. Molines, and M. Cottet. Water mass transformation in the North Atlantic and its impact on the meridional circulation: insights from an ocean model forced by NCEP-NCAR reanalysis surface fluxes. *Journal of Climate*, 16:3085–3110, 2003.
- [49] S. L. Hautala, D. H. Roemmich, and W. J. Schmitz. Is the north pacific in sverdrup balance along 24°N? *Journal of Geophysical Research: Oceans*, 99:16041–16052, 1994.
- [50] E. Hawkins, R. S. Smith, L. C. Allison, J. M. Gregory, T. J. Woollings, H. Pohlmann, and B. de Cuevas. Bistability of the Atlantic overturning circulation in a global climate model and links to ocean freshwater transport. *Geophysical Research Letters*, 38:L10605, 2011.
- [51] P. H. Haynes, D. A. Poet, and E. F. Shuckburgh. Transport and mixing in kinematic and dynamically consistent flows. *Journal of the Atmospheric Sciences*, 64:3640–3651, 2007.
- [52] W. Hazeleger and R. J. Haarsma. Sensitivity of tropical Atlantic climate to mixing in a coupled ocean–atmosphere model. *Climate Dynamics*, 25: 387–399, 2005.
- [53] G. O. Hughes and R. W. Griffiths. Horizontal convection. *Annual Review of Fluid Mechanics*, 40:185–208, 2008.
- [54] S. E. Huisman, M. den Toom, H. A. Dijkstra, and S. Drijfhout. An indicator of the multiple equilibria regime of the Atlantic Meridional Overturning Circulation. *Journal of Physical Oceanography*, 40:551–567, 2010.
- [55] W. E. Johns, M. O. Baringer, L. M. Beal, S. A. Cunningham, T. Kanzow, H. L. Bryden, J. J.-M. Hirschi, J. Marotzke, C. S. Meinen, B. Shaw, and R. Curry. Continuous, array-based estimates of Atlantic Ocean heat transport at 26.5°N. *Journal of Climate*, 24:2429–2449, 2011.
- [56] H. L. Johnson and D. P. Marshall. A theory for the surface Atlantic response to thermohaline variability. *Journal of Physical Oceanography*, 32:1121–1132, 2002.

- [57] H. L. Johnson, D. P. Marshall, and D. A. J. Sproson. Reconciling theories of a mechanically driven meridional overturning circulation with thermohaline forcing and multiple equilibria. *Climate Dynamics*, 29: 821–836, 2007.
- [58] J. Karlsson, G. Svensson, and H. Rodhe. Cloud radiative forcing of subtropical low level clouds in global models. *Climate Dynamics*, 30:779–788, 2008.
- [59] U. Krebs and A. Timmermann. Tropical Air–Sea interactions accelerate the recovery of the Atlantic Meridional Overturning Circulation after a major shutdown. *Journal of Climate*, 20:4940–4956, 2007.
- [60] F. Kucharski and F. Molteni. On non-linearities in a forced North Atlantic oscillation. *Climate Dynamics*, 21:677–687, 2003.
- [61] C. Kuehn. A mathematical framework for critical transitions: Bifurcations, fast-slow systems and stochastic dynamics. *Physica D: Nonlinear Phenomena*, 240:1020–1035, 2011.
- [62] T. Kuhlbrodt, A. Griesel, M. Montoya, A. Levermann, M. Hofmann, and S. Rahmstorf. On the driving processes of the Atlantic Meridional Overturning Circulation. *Reviews of Geophysics*, 45:RG2001, 2007.
- [63] M. Latif, D. Anderson, T. Barnett, M. Cane, R. Kleeman, A. Leetmaa, J. O’Brien, A. Rosati, and E. Schneider. A review of the predictability and prediction of ENSO. *Journal of Geophysical Research*, 103:14375–14393, 1998.
- [64] M. Latif, E. Roeckner, U. Mikolajewicz, and R. Voss. Tropical stabilization of the Thermohaline Circulation in a greenhouse warming simulation. *Journal of Climate*, 13:1809–1813, 2000.
- [65] A. Laurian, S. S. Drijfhout, W. Hazeleger, and R. van Dorland. Global surface cooling: the atmospheric fast feedback response to a collapse of the Thermohaline Circulation. *Geophysical Research Letters*, 36:L20708, 2009.
- [66] T. M. Lenton, H. Held, E. Kriegler, J. W. Hall, W. Lucht, S. Rahmstorf, and H. J. Schellnhuber. Tipping elements in the Earth’s climate system. *Proceedings of the National Academy of Sciences of the United States of America*, 105:1786–1793, 2008.
- [67] A. Levermann and J. J. Fürst. Atlantic pycnocline theory scrutinized using a coupled climate model. *Geophysical Research Letters*, 37:L14602, 2010.

- [68] S. Levitus and T. P. Boyer. *World Ocean Atlas: 1994*, volume 2. U.S. Department of Commerce, Washington, USA, 1994.
- [69] H. Longworth, J. Marotzke, and T. F. Stocker. Ocean gyres and abrupt change in the Thermohaline Circulation: a conceptual analysis. *Journal of Climate*, 18:2403–2416, 2005.
- [70] R. Lumpkin and K. Speer. Global Ocean meridional overturning. *Journal of Physical Oceanography*, 37:2550–2562, 2007.
- [71] J. Marotzke. Boundary mixing and the dynamics of three-dimensional thermohaline circulations. *Journal of Physical Oceanography*, 27:1713–1728, 1997.
- [72] J. Marotzke and B. A. Klinger. The dynamics of equatorially asymmetric thermohaline circulations. *Journal of Physical Oceanography*, 30:955–970, 2000.
- [73] J. Marotzke and J. Willebrand. Multiple equilibria of the Global Thermohaline Circulation. *Journal of Physical Oceanography*, 21:1372–1385, 1991.
- [74] R. Marsh, W. Hazeleger, A. Yool, and E. J. Rohling. Stability of the Thermohaline Circulation under millennial CO₂ forcing and two alternative controls on Atlantic salinity. *Geophysical Research Letters*, 34:L03605, 2007.
- [75] D. P. Marshall and H. R. Pillar. Momentum balance of the wind-driven and Meridional Overturning Circulation. *Journal of Physical Oceanography*, 41:960–978, 2011.
- [76] J. Marshall, A. Adcroft, C. Hill, L. Perelman, and C. Heisey. A finite-volume, incompressible navier stokes model for studies of the ocean on parallel computers. *Journal of Geophysical Research*, 102:5753–5766, 1997.
- [77] C. Meunier and A. D. Verga. Noise and bifurcations. *Journal of statistical physics*, 50:345–375, 1988.
- [78] F. Molteni. Atmospheric simulations using a GCM with simplified physical parametrizations. I: model climatology and variability in multi-decadal experiments. *Climate Dynamics*, 20:175–191, 2003.
- [79] M. Nakamura, P. H. Stone, and J. Marotzke. Destabilization of the Thermohaline Circulation by atmospheric eddy transports. *Journal of Climate*, 7:1870–1882, 1994.

- [80] J. D. Neelin, I. M. Held, and K. H. Cook. Evaporation–wind feedback and low-frequency variability in the tropical atmosphere. *Journal of the Atmospheric Sciences*, 44:2341–2348, 1987.
- [81] M. Nikurashin and G. Vallis. A theory of the interhemispheric Meridional Overturning Circulation and associated stratification. *Journal of Physical Oceanography*, 42:1652–1667, 2012.
- [82] M. Nonaka and S.-P. Xie. Covariations of sea surface temperature and wind over the Kuroshio and its extension: Evidence for ocean–to–atmosphere feedback. *Journal of Climate*, 16:1404–1413, 2003.
- [83] K. I. C. Oliver, A. J. Watson, and D. P. Stevens. Can limited ocean mixing buffer rapid climate change? *Tellus A*, 57:676–690, 2005.
- [84] Y.-G. Park. The stability of Thermohaline Circulation in a two–box model. *Journal of Physical Oceanography*, 29:3101–3110, 1999.
- [85] Y.-G. Park and K. Bryan. Comparison of thermally driven Circulations from a depth-coordinate model and an isopycnal-layer model. part i: Scaling-law sensitivity to vertical diffusivity. *Journal of Physical Oceanography*, 30:590–605, 2000.
- [86] S. Rahmstorf. On the freshwater forcing and transport of the Atlantic Thermohaline Circulation. *Climate Dynamics*, 12:799–811, 1996.
- [87] S. Rahmstorf. Bifurcations of the Atlantic Thermohaline Circulation in response to changes in the hydrological cycle. *Nature*, 378:145–149, 1995.
- [88] S. Rahmstorf, M. Crucifix, A. Ganopolski, H. Goosse, I. Kamenkovich, R. Knutti, G. Lohmann, R. Marsh, L. A. Mysak, Z. Wang, and A. J. Weaver. Thermohaline Circulation hysteresis: a model intercomparison. *Geophysical Research Letters*, 32:L23605, 2005.
- [89] C. Rooth. Hydrology and ocean circulation. *Progress In Oceanography*, 11:131–149, 1982.
- [90] R. M. Samelson. Simple mechanistic models of middepth meridional overturning. *Journal of Physical Oceanography*, 34:2096–2103, 2004.
- [91] A. Schmittner, M. Latif, and B. Schneider. Model projections of the North Atlantic Thermohaline Circulation for the 21st century assessed by observations. *Geophysical Research Letters*, 32:L23710, 2005.

- [92] J. R. Scott, J. Marotzke, and P. H. Stone. Interhemispheric Thermohaline Circulation in a coupled box model. *Journal of Physical Oceanography*, 29:351–365, 1999.
- [93] C. A. Severijns and W. Hazeleger. The efficient global primitive equation climate model SPEEDO. *Geoscientific Model Development Discussions*, 2: 1115–1155, 2009.
- [94] W. P. Sijp and M. H. England. Sensitivity of the Atlantic Thermohaline Circulation and its stability to basin-scale variations in vertical mixing. *Journal of Climate*, 19:5467–5478, 2006.
- [95] W. P. Sijp, J. M. Gregory, R. Tailleux, and P. Spence. The key role of the western boundary in linking the AMOC strength to the north–south pressure gradient. *Journal of Physical Oceanography*, 42:628–643, 2012.
- [96] M. A. Spall. Dynamics of the Gulf Stream/deep western boundary current crossover. Part II: low-frequency internal oscillations. *Journal of Physical Oceanography*, 26:2169–2182, 1996.
- [97] M. A. Spall. Boundary currents and watermass transformation in marginal seas. *Journal of Physical Oceanography*, 34:1197–1213, 2004.
- [98] M. A. Spall and R. S. Pickart. Where does dense water sink? a subpolar gyre example. *Journal of Physical Oceanography*, 31:810–826, 2001.
- [99] H. Stommel. Thermohaline convection with two stable regimes of flow. *Tellus*, 13:224–230, 1961.
- [100] H. Stommel and A. Arons. On the abyssal circulation of the world ocean—I. Stationary planetary flow patterns on a sphere. *Deep Sea Research (1953)*, 6:140–154, 1959.
- [101] R. J. Stouffer, J. Yin, J. M. Gregory, K. W. Dixon, M. J. Spelman, W. Hurlin, A. J. Weaver, M. Eby, G. M. Flato, H. Hasumi, A. Hu, J. H. Jungclaus, I. V. Kamenkovich, A. Levermann, M. Montoya, S. Murakami, S. Nawrath, A. Oka, W. R. Peltier, D. Y. Robitaille, A. Sokolov, G. Vettoretti, and S. L. Weber. Investigating the causes of the response of the Thermohaline Circulation to past and future climate changes. *Journal of Climate*, 19:1365–1387, 2006.
- [102] F. Straneo. On the connection between dense water formation, overturning, and poleward heat transport in a convective basin. *Journal of Physical Oceanography*, 36:1822–1840, 2006.

- [103] H.-H. Syu, J. D. Neelin, and D. Gutzler. Seasonal and interannual variability in a hybrid coupled GCM. *Journal of Climate*, 8:2121–2143, 1995.
- [104] R. Tailleux. Available potential energy and exergy in stratified fluids. *Annual Review of Fluid Mechanics*, 45:35–58, 2013.
- [105] L. Talley. Freshwater transport estimates and the Global Overturning Circulation: shallow, deep and throughflow components. *Progress In Oceanography*, 78:257–303, 2008.
- [106] The R Development Core Team. *R: A Language and Environment for Statistical Computing*. R Foundation For Statistical Computing, Vienna, Austria, 2009.
- [107] A. Timmermann, H. Gildor, M. Schulz, and E. Tziperman. Coherent resonant millennial-scale climate oscillations triggered by massive meltwater pulses. *Journal of Climate*, 16:2569–2585, 2003.
- [108] A. Timmermann, U. Krebs, F. Justino, H. Goosse, and T. Ivanochko. Mechanisms for millennial-scale global synchronization during the last glacial period. *Paleoceanography*, 20:PA4008, 2005.
- [109] K. Trenberth, J. Olson, and W. Large. A global ocean wind stress climatology based on ECMWF analyses. National Center for Atmospheric Research, Boulder, USA, 1989.
- [110] E. Tziperman. On the role of interior mixing and air-sea fluxes in determining the stratification and circulation of the oceans. *Journal of Physical Oceanography*, 16:680–693, 1986.
- [111] G. K. Vallis. Large-scale circulation and production of stratification: effects of wind, geometry, and diffusion. *Journal of Physical Oceanography*, 30:933–954, 2000.
- [112] M. van den Broeke, J. Bamber, J. Ettema, E. Rignot, E. Schrama, W. J. van de Berg, E. van Meijgaard, I. Velicogna, and B. Wouters. Partitioning recent Greenland mass loss. *Science*, 326:984–986, 2009.
- [113] E. van Sebille, M. O. Baringer, W. E. Johns, C. S. Meinen, L. M. Beal, M. F. d. Jong, and H. M. v. Aken. Propagation pathways of classical Labrador Sea water from its source region to 26°N. *Journal of Geophysical Research*, 116:C12027, 2011.
- [114] M. Vellinga and R. A. Wood. Global climatic impacts of a collapse of the Atlantic Thermohaline Circulation. *Climatic Change*, 54:251–267, 2002.

- [115] M. Vellinga, R. A. Wood, and J. M. Gregory. Processes governing the recovery of a perturbed Thermohaline Circulation in HadCM3. *Journal of Climate*, 15:764–780, 2002.
- [116] J.-S. von Storch, J. P. Montavez, and B. S. Beena. EMAD: an empirical model of air-sea fluxes. *Meteorologische Zeitschrift*, 14:755–762, 2005.
- [117] J. M. Wallace, C. Smith, and Q. Jiang. Spatial patterns of atmosphere–ocean interaction in the northern winter. *Journal of Climate*, 3:990, 1990.
- [118] W. Weijer, W. P. De Ruijter, A. Sterl, and S. S. Drijfhout. Response of the Atlantic overturning circulation to South Atlantic sources of buoyancy. *Global and Planetary Change*, 34:293–311, 2002.
- [119] W. Weijer, H. A. Dijkstra, H. Öksüzoğlu, F. W. Wubs, and A. C. de Niet. A fully-implicit model of the global ocean circulation. *Journal of Computational Physics*, 192:452–470, 2003.
- [120] C. L. Wolfe and P. Cessi. What sets the strength of the middepth stratification and overturning circulation in eddy ocean models? *Journal of Physical Oceanography*, 40:1520–1538, 2010.
- [121] C. L. Wolfe and P. Cessi. The adiabatic pole-to-pole overturning circulation. *Journal of Physical Oceanography*, 41:1795–1810, 2011.
- [122] Wolfram Research, Inc. *Mathematica*. Wolfram Research, Inc., Champaign, USA, 8.0 edition, 2010.
- [123] C. Wunsch. The decadal mean ocean circulation and sverdrup balance. *Journal of Marine Research*, 69:417–434, 2011.
- [124] J. Yin, M. E. Schlesinger, N. G. Andronova, S. Malyshev, and B. Li. Is a shutdown of the Thermohaline Circulation irreversible? *Journal of Geophysical Research*, 111:D12104, 2006.
- [125] G. J. Zhang, V. Ramanathan, and M. J. McPhaden. Convection–evaporation feedback in the equatorial Pacific. *Journal of Climate*, 8:3040–3051, 1995.

LIST OF PUBLICATIONS

1. S. Drijfhout, G. J. van Oldenborgh, and A. Cimatoribus. Is a decline of AMOC causing the warming hole above the North Atlantic in observed and modeled warming patterns? *Journal of Climate*, 25:8373–8379, 2012.
2. M. Eby *et al.* Historical and idealized climate model experiments: an EMIC intercomparison. *Climate of the Past Discussions*, 8:4121–4181, 2012.
3. A. A. Cimatoribus, S. S. Drijfhout, and H. A. Dijkstra. Meridional overturning circulation: stability and driving mechanisms in a box model. *Climate Dynamics*, In press, 2012.
4. A. A. Cimatoribus, S. S. Drijfhout, V. Livina, and G. van der Sclier. Dansgaard–Oeschger events: tipping points in the climate system. *Climate of the Past*, 9:323–333, 2013.
5. M. den Toom, H. A. Dijkstra, A. A. Cimatoribus, and S. S. Drijfhout. Effect of atmospheric feedbacks on the stability of the Atlantic meridional overturning circulation. *Journal of Climate*, 25:4081–4096, 2012.
6. A. A. Cimatoribus, M. den Toom, S. S. Drijfhout, and H. A. Dijkstra. Sensitivity of the Atlantic meridional overturning circulation to South Atlantic freshwater anomalies. *Climate Dynamics*, 39:2291–2306, 2012.
7. A. A. Cimatoribus, S. S. Drijfhout, and H. A. Dijkstra. A global hybrid coupled model based on atmosphere–SST feedbacks. *Climate Dynamics*, 38:745–760, 2011.
8. A. A. Cimatoribus, S. Sacconi, F. Bencivenga, A. Gessini, M. G. Izzo, and C. Masciovecchio. The mixed longitudinal–transverse nature of collective modes in water. *New Journal of Physics*, 12:053008, 2010.
9. F. Bencivenga, A. Cimatoribus, A. Gessini, M. G. Izzo, and C. Masciovecchio. Temperature and density dependence of the structural relaxation time in water by inelastic ultraviolet scattering. *Journal of Chemical Physics*, 131:144502, 2009.
10. F. Bencivenga, A. Cimatoribus, A. Gessini, and M. G. Izzo. Anomalous density dependence of structural relaxation time in water. *Philosophical Magazine*, 88:4137–4142, 2008.

For an up-to-date list of publications, visit: <http://www.andreacimatoribus.it>

ACKNOWLEDGMENTS

First, I want to thank Sybren Drijfhout: not only has he been a supportive and helpful supervisor, but he has also given me the freedom to try and to make mistakes on my own. I cannot imagine a better way to learn. I would like to thank Henk Dijkstra: he is one of the busiest persons I have ever met, still he has always found the time for discussing my work, for replying to my questions and for supporting my ideas. His endless curiosity has been a continuous source of motivation. I would like to thank Matthijs den Toom, working with such a smart person has given me countless chances to learn. I would like to thank him also for kindly providing the translation of the abstract.

I would like to thank all the people, at KNMI, IMAU and elsewhere, who gave a great contribution to this work by discussing with me, answering my questions, suggesting new lines of research or just by keeping me interested in the world of Oceanography, Climate and GFD. Among others, I should mention Will de Ruijter, Anna von der Heydt, Leo Maas, David Marshall, Andreas Sterl, Dewi Le Bars, Jan Viebahn, Anna Rabitti, Jelle van den Berk, Sjoerd Groeskamp. Some ideas born during these discussions have grown and can be found in these pages, others did not reach maturity, at least not yet, but have been as important as those which did.

Had I only been working during the last four years, this thesis would not exist. I thus want to thank those who helped making my last four years a time worth living. A list of all of them would be too long and would not add much; let me just write the names of Anna, my new house mate, and Carlo and Sara, my old ones. In very different ways, they have been a constant presence, and one that has made my days better.

Last but not least, a great thanks to my family, who has been helping and supporting despite the distance.

This document was typeset using `classicthesis` developed by André Miede.

Final Version as of 16th April 2013 (`classicthesis`).

“grazie”